Cosmic Magnetism: The Plasma Physics of the Recombining Universe

Submitted in fulfilment of the requirements for the Degree of Doctor of Philosophy

Euan David Bennet, M. Sci.

School of Physics and Astronomy
College of Science and Engineering
University of Glasgow

Submitted May 2012

Contents

List of Figures

Abstract

This thesis presents an analytical and computational approach to modelling partially ionised, spatially-inhomogeneous and recombining plasmas. The specific context for this study is astrophysical plasmas, the early Universe in particular. Two models are investigated in detail: a magnetohydrodynamic (MHD) plasma model to simulate partially ionised plasmas; and a fully electromagnetic/kinetic model, used to study recombining plasmas.

The first section further develops an existing computational model of a partially ionised plasma as a mixture of two cospatial fluids: an MHD plasma and a neutral gas. In order to model the interaction *between* the plasma and neutral gas populations *ab initio*, a collisional momentum exchange term was added to the momentum equation of each fluid. The model was used to investigate the combined response to different wave modes driven in the plasma or the neutral gas. The momentum coupling between the plasma and the neutral gas leads to complex interactions between the two populations. In particular, the propagation of plasma waves induces waves in the neutral gas by virtue of the collisional momentum exchange between the velocity fields of each fluid. This means that the normal wave modes of each independent fluid are modified to produce a combined, hybrid response, with the intriguing possibility that neutral gas can not only respond indirectly to magnetic fluctuations but also generate them via sound waves.

This model is used to examine an existing observational method known as the 'Chandrasekhar-Fermi method' (CF53) for the diagnosis of magnetic fields in astrophysical plasmas. CF53 is commonly applied to objects such as nebulae and molecular clouds which are partially-ionised plasmas. It assumes that the gas motion can be used to infer the magnetic field strength, given coupling between Alfvén waves in the plasma and the thermal motion of the neutral gas. Computational results show that this method may need to be refined, and that certain assumptions made should

be re-evaluated. This is consistent with reports in the literature of CF53 under- *or* over-estimating the magnetic fields in objects such as molecular clouds.

The second part of this thesis concentrates on the non-equilibrium evolution of magnetic field structures at the onset of the large-scale recombination of an inhomogeneously-ionised plasma, such as the Universe was during the epoch of recombination. The conduction currents sustaining the magnetic structure will be removed as the charges comprising them combine into neutrals. The effect that a decaying magnetic flux has on the acceleration of remaining charged particles via the transient induced electric field is considered. Since the residual charged-particle number density is small as a result of decoupling, the magnetic and electric fields can be considered essentially to be imposed, neglecting for now the feedback from any minority accelerated population.

The electromagnetic treatment of this phase transition can produce energetic electrons scattered throughout the Universe. Such particles could have a significant effect on cosmic evolution in several ways: (i) their presence could influence the overall physics of the recombination era; and (ii) a population of energetic particles might lend a Coulomb contribution to localized gravitational collapse.

This is confirmed by a numerical simulation in which a magnetic domain is modelled as a uniform field region produced by a thin surrounding current sheet. The imposed decay of the current sheet simulates the formation of neutrals characteristic of the decoupling era, and the induced electric field accompanying the magnetic collapse is able to accelerate ambient stationary electrons (that is, electrons not participating in the current sheet) to energies of up to order 10keV. This is consistent with theoretical predictions.

Acknowledgements

This thesis would not have been possible without the support and encouragement of several excellent individuals. First and foremost I would like to thank my supervisor Declan Diver, whose knowledge, advice, and infectious enthusiasm have been invaluable throughout. I was fortunate indeed to have the opportunity to work with such a talented supervisor who always praised achievements, encouraged recovery from setbacks and nurtured my enthusiasm both for my own work and for physics in general.

I have been very lucky to work with many talented people: Martin Hendry gave me my first work experience in a research environment, and he has always been a friendly and reliable source of advice; Hugh Potts, who was always happy to share his extensive knowledge, as well as being a specialist at finding entertaining things on the internet! Last but not least, I wish to thank Luis Teodoro, who has always challenged me to bring out the best of my abilities. I look forward and hope to have the chance to work with all four of these excellent people in the future.

To thank the people in my life away from work, I must begin with my parents, who have had the best and most positive influence any son could ask for. They encouraged my love of reading and nurtured my enthusiasm for science from an early age, and have always challenged me to improve whilst keeping my feet on the ground with each new achievement and milestone. In all aspects of my life, I am certain I would not be who or where I am today without them. My sister Lorna has always inspired and supported me too. My aunt Elspeth has had a positive impact throughout my life. My girlfriend Natasha has been the perfect partner over the last eight months, and I hope for many more to come.

Finally I want to thank my friends, in particular: Greg, Stephen, Barry, Fraser, Isla, David, Derek, Christine, and Karen. To avoid writing a huge list of names, I'll mention all together the football crowd (especially Eric and Gail) and the Kelvin SNP crowd (especially Mark, Patrick and Kenny).

Declaration

I declare that this thesis is my own composition except where indicated in the text and that no portion of the work referred to in the thesis has been submitted in support of an application for another degree or qualification from this or any other institution.

Copyright Statement

"If knowledge can create problems, it is not through ignorance that we can solve them."

Isaac Asimov

"Very simple was my explanation, and plausible enough - as most wrong theories are!"

H. G. Wells, 'The Time Machine'

1

Introduction

1.1 Plasmas

Plasma is usually described as the fourth phase of matter, after solid, liquid and gas. The name was first coined by Irving Langmuir in 1928, who had noticed unusual electron oscillations during his experiments with ionised gas. The definition came about as follows (Langmuir 1928):

> "It seemed that these oscillations must be regarded as compressional electric waves somewhat analogous to sound waves. Except near the electrodes, where there are *sheaths* containing very few electrons, the ionized gas contains ions and electrons in about equal numbers so that the resultant space charge is very small. We shall use the name *plasma* to describe this region containing balanced charges of ions and electrons."

Subsequently, the name *plasma* has become the accepted term for any quasi-neutral[1] collection of charged particles with sufficiently high number density such that electromagnetism is the dominant force, and collective effects are a significant part of the

[1] *charge quasi-neutral*: although the individual particles that make up the plasma are electrically charged, over length scales longer than a characteristic length (see section 1.5.1) the system as a whole is neutral.

dynamics.

The most intuitive example of a plasma is that of a gas that has been ionised either by heating or by electric discharge: electrons have been removed from the neutral atoms, leaving a mixture of positive ions and electrons. Plasmas are all around us today, whether produced by man-made devices such as lightbulbs and television screens, or found naturally in the upper reaches of Earth's atmosphere and out into the Solar system and beyond. The most obvious and important plasma to everyday life is found in the Sun. Most of the matter in the Universe exists as plasma, meaning that plasmas are truly ubiquitous.

Plasmas are fascinating because their behaviour can be very complex, often surprising and sometimes very counterintuitive: the dynamics tend to be dominated by long-range collective effects rather than individual particle-particle interactions such as those common in gas dynamics or gravitation.

1.1.1 Types of Plasma

The most common kinds of plasma are electron-ion plasmas consisting of electrons and positive ions. This includes any kind of positive ion, for example Hydrogen plasmas which are made up of protons as the positive species, and electrons. Practically, electron-ion plasmas would usually have a number of different positive species, either by mass or ionisation level. For example, in the plasma of the early Universe it is believed that the positive ions were almost all Hydrogen ions, but that a small percentage ions were Helium nuclei (twice-ionised) and that an even tinier percentage were Lithium or Beryllium nuclei. Similarly, a Chlorine plasma would have ions with a variety of positive charges - some Chlorine atoms would lose just one electron (to become once-ionised, an ion with a charge of +1) but some of the atoms would become more ionised, losing between two and all of their electrons.

More exotic kinds of plasmas also exist in nature and in the lab. An extremely common example is dusty plasma. This variant electron-ion plasma has an extra kind

of particle present - dust. Dust is a generic term for a group or clump of atoms or ions. Dusty plasmas provide an important opportunity to improve our understanding of many situations, including stellar and planetary formation. Another example of the importance of dusty plasmas is in fusion research, where it is essential to understand the interaction between the plasma in the tokamak and potential contaminants that could be introduced from the device itself (Tsytovich et al. 2008).

It is also possible for a plasma to have positive and negative ion species, with applications such as negative ion beams or even the formation of neutral beams used in tokamak heating (Freidberg 2007).

A much rarer kind is electron-positron pair plasma. It has been postulated (da Costa et al. 2011; Diver et al. 2010) that such plasmas may exist around pulsars, which are rapidly rotating neutron stars resulting from a star that has exploded in a supernova. Pair plasmas are very unusual because the mass of the positive charge species is equal to the mass of the negative charge species, leading to quite different theoretical results from those for conventional plasmas. Unique dynamics and instabilities are introduced, not least because of the possibility that an electron-positron collision could result in annihilation as opposed to the more conventional recombination reaction usually encountered in, say, an electron-proton collision.

Plasmas in Nature

As a rule of thumb, most material observed in space that emits light or other electromagnetic radiation of its own accord is a plasma. This includes stars, nebulae, accretion disks, pulsars and interstellar dust, to name just a few examples. These examples cover a wide range of temperature and density regimes even within a single object: for instance, the Sun's photosphere (the visible surface, i.e. where the plasma becomes optically opaque) is observed to have a blackbody temperature of around $5,800\,\mathrm{K}$ and a particle number density of order $10^{23}\,\mathrm{m}^{-3}$, but the corona (the optically-thin outer atmosphere) is a much sparser, hotter plasma with around $1,000,000\,\mathrm{K}$ temperature and a number density of order $10^{15} - 10^{16}\,\mathrm{m}^{-3}$ (Aschwanden 2005). Pulsars are home to

Table 1.1: Typical physical properties of natural plasmas.

Type of Plasma	Temperature/K	Number Density/m^{-3}	Magnetic Field/T
Solar photosphere	6×10^3	10^{23}	10^{-4}
Solar corona	$\gtrsim 10^6$	10^{15}	10^{-2}
Earth's ionosphere	10^2	10^9	$10^{-5} - 10^{-4}$
Lightning	10^5	10^{21}	10^{-5}
Interstellar medium	$10^3 - 10^4$	$10^2 - 10^5$	$10^{-10} - 10^{-8}$
Pulsar atmosphere	$< 10^6$	$10^{11} - 10^{14}$	10^8
Neutral Hydrogen cloud	$10 - 10^2$	$10^8 - 10^9$	10^{-7}

some of the most extreme environments, and physics, in the Universe. Magnetic flux densities of order 10^8 T have been inferred from observations, far stronger than the magnetic fields found in any other natural plasma. Table 1.1 shows the typical orders of magnitude of temperature, ion number density and magnetic field strength observed in various naturally-occurring plasmas[2].

A great deal of the Universe is made up of relatively low-temperature, low-density plasma. Section 1.2 below will discuss in detail these specific plasmas, with which this thesis is primarily concerned.

The terrestrial environment also hosts naturally-occurring plasmas, the closest and clearest example of which is the ionosphere layer of the Earth's atmosphere. The ionosphere is present because the radiation from the Sun ionises the gas in the Earth's atmosphere, and it is practically important because radio signals can be reflected by the plasma in the ionosphere in order to communicate around the world. The ionosphere also interacts with the Earth's magnetic field, and changes depending on Solar activity. Other terrestrial objects including the planets Venus, Jupiter and Uranus, and Saturn's moon Titan also have observed ionospheres. Lightning is another extremely

[2]Pulsar atmosphere number density was estimated using the Goldreich-Julian formula (Goldreich and Julian 1969), although it has been shown that this may drastically underestimate the density (Lyutikov 2007).

common natural plasma, on Earth and elsewhere. It is caused by the discharge of static electricity that builds up in the atmosphere due to collisional ionisation between atoms and molecules.

Lab Plasmas and Applications

Plasmas are now extremely common in everyday life, with the most obvious examples being modern lightbulbs (including fluorescent and energy-saving bulbs) and television screens. When it comes to industrial applications, it is now difficult to name an industry where plasmas *aren't* used in some shape or form. Particularly important uses of plasmas are in the surface modification of materials, such as the etching of silicon pathways in microchips for computers, and for sterilisation of food and water. Many new applications are currently in development.

In pure research terms, there is a very wide field of study of plasmas, incorporating not just physics but also chemical and electrical engineering, chemistry, and biology. Research into fields as diverse as laser fusion and magnetic drug delivery, and everything in between, is exciting, innovative and ultimately will make a positive impact in everyday life.

1.2 Astrophysical Plasmas

The most abundant plasmas in the Universe occur naturally. In fact, the vast majority of the matter in the Universe is low-temperature, low-pressure plasma. Much of this can be seen in infrared images of nebulae, molecular clouds and galactic spiral arms, to name a few examples. In terms of elemental abundance, the most common plasmas are largely populated by ions of atomic or molecular Hydrogen, with a small proportion of heavier elements. Localised regions may contain larger concentrations of particular elements, for example in nebulae which are the result of a supernova. In most cases, the density and temperature regimes are quite different from those of the plasmas generated in the lab on Earth.

1.2.1 Low-temperature Plasmas

Away from hot, dense regions such as stars, the majority of plasmas are only partially ionised; i.e. along with positive ions and electrons, a significant population of the plasma is neutral gas in the form of atoms or molecules. Nebulae and molecular clouds are good examples of dense partially-ionised plasmas. The interstellar medium (ISM) is a very low-density (lower range around $10^5 - 10^6\,\mathrm{m}^{-3}$), low-temperature (low range of order $10^2 - 10^4\,\mathrm{K}$) plasma. Assumptions can be and are made so that, for example, molecular clouds are modelled as entirely plasma, or the ISM is considered to follow neutral gas dynamics, but subtlety is lost. At some stage, arguably one that has already been reached, the precision of astrophysical observations will surpass the precision of such assumptions. When that happens, the modelling techniques must be refined in order to gain new understanding.

As an example, consider the ongoing problem of understanding how large-scale structure in the Universe first formed. There is a disparity between the predictions made by popular models of galaxy formation and the true observations. For example, in the most popular "cold dark matter" model, it is predicted that galaxies and larger structures grew over time from small overdense perturbations. However, the interpretation of observations suggest a *top-down* hierarchical process could have taken place, with the largest structures forming first and then gradually smaller structures (galaxy superclusters, clusters, then individual galaxies) forming from fragments as perturbed regions collapse under self-gravity (Carroll and Ostlie 2006; Benson 2010). Unfortunately theories of top-down structure formation have their own problems and are not fully supported by observations either: under these theories it is predicted that the Universe reionised much later than has been observed because the first stars would not have formed until later. Therefore there is scope to improve both kinds of structure formation model by considering plasma and electromagnetic effects which have until now been largely neglected.

A key assumption of all current popular models is generally that the dynamics

are entirely dominated by gravity, and electromagnetic or plasma effects are generally considered to be unable to challenge this dominance. However, modern observations show that coherent magnetic structures exist not just on a galactic scale, but on scales as large as galactic clusters. It is therefore crucial to develop understanding of the plasmas on galactic scales which *must* be responsible for sustaining these large-scale magnetic fields.

The partially-ionised nature of most astrophysical plasmas naturally makes modelling slightly more complex, as there are interactions in each of the ionised and neutral populations that are mutually exclusive, but there are also interactions *between* the populations.

1.2.2 The Early Universe

The currently accepted paradigm of the early Universe, big bang theory, states that after an initial singularity at the beginning of the Universe, an initial "soup" of fundamental particles, probably electrons, quarks and gluons[3], came into existence. According to the most popular description of the early Universe, although for as yet unexplained physical reasons, an extremely short period of exponential expansion known as inflation is believed to have preceded this epoch within the first 10^{-32} seconds of all existence. After the inflation period, the standard model says that the Universe continued to expand adiabatically, and as it cooled atomic nuclei formed during the process known as primordial nucleosynthesis. From the elemental abundances observed today, this is predicted to have happened within the first 20 minutes. At this stage it is thought that the Universe was a fully-ionised plasma, with the ion population consisting of around 75% Hydrogen ions (protons, with traces of Deuterium and Tritium ions), 25% Helium ions (α-particles), and trace amounts of Lithium and Beryllium (Carroll and Ostlie 2006). For a nucleosynthesis model to conform to current observations, no other

[3]This soup would have been a very unusual plasma, containing multiple ion species with non-integer charge.

heavier elements should have been created at this time.

The predictions of the current big bang model, along with the popular cosmological ΛCDM[4] model can be compared with observations to infer these details about the early Universe. No direct observations can be made currently, since the earliest possible epoch of the Universe that can be observed is of order some $500,000$ years after the end of the predicted inflation period. This is the cosmic microwave background (CMB), isotropic radiation observed today that has travelled uninterrupted over billions of years across the Universe.

The Epoch of Recombination

The microwave background is the most compelling piece of evidence supporting the big bang/ΛCDM model of the Universe. As it covers the entire sky isotropically and is very homogeneous, the CMB is thought to be a direct observation of an epoch in the early Universe known as *recombination*, or *decoupling*. Prior to this epoch all of the plasma in the Universe was strongly coupled to the dense photon population[5] by Compton scattering. The plasma was fully-ionised, in the sense that the rate of ionisation was very much greater than the rate of neutralisation. The accepted picture of the recombination epoch is that as the Universe expanded and cooled, eventually a tipping point was reached where neutralisations in the plasma significantly outnumbered ionisations. Recombination is thought to have begun around $380,000$ years after the end of inflation, and within about $100,000$ years of the beginning of the process the ionisation fraction of the Universe dropped from 1 to 10^{-5}, which is similar to the ionisation fraction of many technological plasmas. This significant change meant that not only did the photons and baryons become decoupled (with the photons travelling on across the Universe to be observed today as the microwave background), but that gravity became the dominant force over all others in the Universe. A plasma with ionisation fraction 10^{-5} would still behave like a plasma however, and electromagnetic

[4]Dark energy, cold dark matter.

[5]Theory suggests that photons outnumbered baryonic particles by a factor of 10^9.

effects would continue to influence the dynamics.

In the literature, it is generally assumed (i) that global recombination of the entire Universe "happened quickly" in the sense that the timescales involved are extremely rapid compared to normal cosmological processes; and (ii) that the electron-proton-photon fluid is a magnetised plasma with "infinite conductivity". Hence in the literature, a simple ideal magnetohydrodynamic (MHD) description is normally used to simulate the epoch of recombination (Subramanian and Barrow 1998a,b; Durrer et al. 1998; Jedamzik et al. 2000). It has been argued recently, for example by Teodoro et al. (2008) and Diver and Teodoro (2008), that while MHD is a successful theory in certain situations, it compromises too much of the electromagnetism to provide a full description of the plasma during this transitional epoch. As these articles point out, there are several issues with timescales, MHD's neglect of the displacement current, and electrical conductivity of the plasma. For example: as recombination began the plasma would have had very high (tending towards infinity) conductivity, but since the ionisation fraction fell by 5 orders of magnitude *during* recombination, it certainly would not retain this convenient characteristic by the end of the transition. It is also impossible (without cleverly adapting MHD theory) to reconcile the slow, fluid timescale that limits the resolution of MHD theories with the relatively rapid dynamics of plasma recombination which happens on atomic timescales - the basic theory simply cannot model any effects that act on timescales shorter than the fluid timescale.

1.3 Magnetic Fields in Astrophysics

It is perhaps self-evident that since most of the Universe is plasma, magnetic fields must also be very common. Indeed, recent developments in astrophysical theory and data are beginning to show how important magnetism is in all kinds of areas. For example, within the Solar system the Earth's magnetic field protects all terrestrial inhabitants from harmful energetic charged particles coming from the Sun and further afield. The Sun's magnetic evolution appears to be related to its 11- and 22-year ac-

tivity cycles. Localised magnetic "reconnection" events are currently one postulated explanation for the coronal heating problem, i.e. the fact that the Sun's surface has a temperature of less than 6000 K but its atmosphere is at over 1 million K. Finally, the Sun's magnetic influence reaches the outer limits of the Solar system, where the *magnetopause* acts in a similar way to the Earth's magnetic field.

Magnetism is also very important in pulsars, which observations have inferred to have extremely strong magnetic fields of up to 10^8 T, even up to 10^{10} T in some extreme cases known as magnetars. The pulsar radiation mechanism, i.e. beamed synchrotron related to the electron-positron pair plasma in the pulsar atmosphere, depends on the strong magnetic fields. Other astrophysical objects including moons, nebulae, and molecular clouds have also been observed to have magnetic properties of some kind.

1.3.1 Magnetic Fields and Large-Scale Structure

It was reported in the late 1940s that the light from distant stars was observed to become up to 5% linearly polarised as it propagates in the interstellar medium (Hall 1949; Hiltner 1949). Spitzer and Tukey (1949) suggested that the alignment of "needle-like" dust grains with large-scale magnetic fields could be responsible. The Hall and Hiltner data was used by Davis and Greenstein (1951) to further develop this theory, suggesting that if dust grains have the shape of an elongated ellipse, and if the grains are composed of a few percent Iron, then the major axis of each grain will experience a torque due to paramagnetic relaxation. This torque would eventually, over timescales of millions of years, align the grain with a weak coherent background magnetic field. The idea of large-scale magnetic fields in the interstellar medium was first developed by Fermi (1949) as part of his explanation for the origin of cosmic rays.

Since these early theories were formulated, it has indeed been discovered that magnetic fields coherent over very long scale lengths are present in our galaxy. Studies have shown that magnetic fields of magnitude $10^{-11} - 10^{-9}$ T exist over very long coherence lengths of order 10^6 pc, i.e. on galactic cluster scales (see Vallee (1997) for a review).

These steady-state fields must be sustained by conduction currents in the material that the galaxies are composed from, but at present there is not a clear explanation as to how the magnetic fields were first induced (see Widrow (2002) and detailed references therein). This poses several potential challenges to theoretical models of large-scale structure formation. Currently it is a great challenge to formulate a theoretical model describing how magnetic fields are first induced (see below), and it is even more challenging to explain how this happened over galactic coherence scales *after* the first galaxies formed.

An alternative is to suggest that coherent large-scale magnetic fields existed before the physical structures formed around them. It is certainly reasonable to assume that the early galactic plasma would follow magnetic influence while present-day structures were formed. Transport of charged particles in magnetic fields is anisotropic, with equilibration parallel to the field direction generally faster than that perpendicular to the field. Therefore even extremely weak magnetic flux densities could have a significant effect, given the timescales involved: structure formation would have taken hundreds of millions, if not billions, of years, and even a small anisotropy could bias the eventual outcome. There is a slight incompatibility between this notion and the currently accepted cosmological paradigm which states that it is non-luminous dark matter which clumped into large scale structure before the ordinary luminous matter followed it. Since the dark matter is assumed to interact only with gravity the magnetic fields would have no influence on structure formation under this paradigm.

For now, the disparity between theory and observation exists. Large-scale structure formation models currently neglect electromagnetism, but magnetic fields observed in close relation to observed large-scale structure probably originally predate the matter structure. Either way, the general assumption for how the magnetic field came to exist is that it was amplified by "magnetic dynamo" from an initial, tiny, "seed field". Currently no physical process has been identified that can achieve such an effect, and generally the initial seed field is thought of as a mathematical initial condition, rather than as a physical electromagnetic phenomenon (Widrow 2002).

1.3.2 Electromagnetism in the Early Universe

Many theories now predict that large-scale magnetic fields were present in the very early Universe, including during decoupling (Battaner and Florido 2009; Giovannini 2004, 2006, 2010; Kosowsky et al. 2005; Kahniashvili et al. 2001; Mack et al. 2002). Some have even suggested that gravitational wave observations (or lack of) could provide limits on any stochastic magnetic fields which could have existed during decoupling (Caprini and Durrer 2002, 2005; Maartens et al. 2001). Various theories have been proposed that attempt to explain the initial induction of these fields (Grasso and Rubinstein 2001; Ichiki et al. 2007; Cho et al. 2009). Takahashi et al. (2008) provide detailed calculations showing that since photons scatter preferentially with electrons rather than protons, this will result in non-zero charge separation and relative motion between the electrons and protons. Ultimately it is this deviation of motion, hence conduction current, that induces magnetic fields in the plasma. The resultant magnetic fields tie electrons and protons to the conduction current, circulating in opposite directions to each other.

In this thesis it shall be assumed that the Universe was initially magnetised pseudo-stochastically into "magnetic domains" which could potentially be related to density perturbations in the early Universe, as shown by Ichiki et al. (2006, 2007). Each domain could be up to kilo- or even mega-parsecs in diameter and would have sustained within it a coherent, roughly uniform magnetic field in a particular direction, with the total field over the Universe summing to zero in order to satisfy the cosmological principle of isotropy. No assumptions are made about *how* the magnetic domains formed, only that they do exist.

In this "steady-state" scenario, the boundaries between magnetic domains would necessarily be formed by regions of conduction current, sustained by the circulation of charges in the plasma. In electromagnetism there is another kind of current that can contribute to inducing magnetic field, that is the displacement current. This is a particular aspect of electromagnetism which will be investigated in chapter 5 in the

context of these magnetic domains during decoupling.

1.3.3 Cosmic Microwave Background Experiments

The cosmic microwave background (CMB) was first discovered accidentally by radio astronomers Arno Penzias and Robert Wilson in 1964. A background bolometric temperature of the Universe had been theorised as early as 1941, and the concept of background radiation with temperature of around 5K was first hinted at by Alpher et al. (1948), but Penzias and Wilson (1965) were the first to discover it observationally. Famously, they originally suspected that their 3.5 ± 1.0 K signal was caused by interference from "white dielectric material" that had been left in their detector by a flock of pigeons. After cleaning their telescope, the signal persisted, and was found to be isotropic across the entire sky. Theorists Dicke, Peebles, Wilkinson and Roll identified the signal as the CMB (Dicke et al. 1965), and in 1978 Penzias and Wilson were awarded the Nobel Prize in Physics. Further implications of the microwave background were first described by Peebles (1965).

The CMB is often described as "the afterglow of the big bang". The cosmological epoch of recombination decoupled the abundant photon population from the baryonic matter, and those photons are what is observed today as the CMB (Peebles 1968). The frequency of the photons observed today is much less than their frequency when decoupled - the photons have been redshifted by the expansion of the Universe. This is completely analogous to the Doppler effect.

COBE

During the 1980s, a number of ground- and balloon-based experiments were carried out to study the CMB. One of the major difficulties for these experiments was thermal interference, so in 1983 the Soviet satellite RELIKT-1 was launched. Among the many advantages of a space telescope, the major benefit for CMB experiments is that less cooling is required than for a detector inside the Earth's atmosphere. The next big

breakthrough came when the NASA satellite COBE (COsmic Background Explorer) was launched in 1989. The FIRAS instrument (Far InfraRed Absolute Spectrophotometer)on COBE measured, for the first time, the blackbody radiation curve that had been theoretically predicted, with a corresponding temperature of 2.7 K (Mather et al. 1990). COBE also discovered that the CMB is isotropic to 1 part in 10^5, i.e. the smallest fluctuations in blackbody temperature are of order $100,000$ times smaller than the overall temperature.

WMAP

NASA's follow-up experiment WMAP (Wilkinson Microwave Anisotropy Probe, Bennett et al. (2003)) launched in 2001 and produced even more spectacular results including narrowing the theoretical limits on the age, composition and expansion of the Universe to unprecedented precision (Larson et al. 2011). The precision of the anisotropy measurements in WMAP improved by an order of magnitude on COBE's measurements, but the instruments on WMAP measured the fluctuations in a different way. Rather than bolometrically measuring the full blackbody spectrum as FIRAS on COBE did, WMAP has five differential radiometers with central frequencies ranging from 23 GHz to 94 GHz. The radiometers measure tiny differences in the power received by two telescope beams pointing in opposite directions. The blackbody temperature is measured in this fashion by comparing a blackbody radiation curve fitted to the measurements from the five frequency channels to a theoretically perfect blackbody. WMAP's detectors are also sensitive to polarisation which has provided other important results (Komatsu et al. 2011).

PLANCK

The European Space Agency (ESA) PLANCK satellite, a next-generation microwave background explorer, was launched in 2009. With nine frequency bands increasing the spectral range covered to 30 - 857 GHz, higher resolution, and an order of magni-

tude better sensitivity, PLANCK will allow significant advances to be made PLANCK Science Team (2005). In particular, the unprecedented precision in polarisation measurements is expected to bring insight into magnetic fields both nearby and in the early Universe. Early results were published in late 2011 in a catalogue including Planck Collaboration et al. (2011a) and 25 other articles.

1.3.4 Observational Techniques

In astrophysics, gathering data is very difficult, since the only source of information is a very limited number of photons. Interpretation is even more difficult: unlike laboratory experiments, the observer has no control over the initial conditions of their "experiment". Fortunately in the modern day, there are many sophisticated observational methods that can yield a surprisingly large amount of information.

Doppler Velocity Measurements

The Doppler effect occurs when an observer measures a wave (light or sound) emanating from a source that is moving in the observer's rest frame. The observed frequency and wavelength of light shifts depending on the relative velocity of the source and observer. If the source is moving towards the observer, the light is *blue-shifted*, i.e. the observed frequency is higher than the emitted frequency, and vice versa for light that is *red-shifted* (Carroll and Ostlie 2006).

This effect is a powerful diagnostic tool for astrophysics, whereby the light observed from distant plasma emission can be interpreted to give insight into the conditions under which it was emitted. For example, consider a single spectral line such as the Hydrogen Balmer α line (H_α) - produced when the electron in a Hydrogen atom makes the transition from the third to the second energy level, and is an excellent indicator of the presence of ionised Hydrogen[6]. The wavelength of the H_α spectral line is

[6]The cascade of transitions of a newly captured electron down to the ground energy state of a recombined atom includes the H_α emission approximately half of the time.

very specific:

$$\lambda_\alpha = 656.281\text{nm} \tag{1.1}$$

Therefore if a cloud of plasma is observed to be emitting spectral lines with wavelengths spread around λ_α with a particular profile, this wavelength dispersion can be used to find the root mean square velocity of particles in the plasma, i.e. the average thermal velocity.

Linear Polarisation Measurements

In a transverse electromagnetic wave such as light, the direction of the electric field vector of the wave is always perpendicular to the direction of travel. The direction of the magnetic field vector is perpendicular to both the electric field vector and the direction of propagation. Consider a wave travelling in the z-direction - the electric field vector will point either in the x- or y-direction, or some superposition of the two. The nature of the transverse wave means that the electric field in the direction of travel must be zero (in vacuum). Ordinary, unpolarised, light contains a superposition of waves with electric field vectors aligned in all directions perpendicular to the propagation direction. Light that has been *polarised* generally means that all of the electric field vectors of the waves point in the same direction (figure 1.1).

Linear polarisation in astronomy is generally thought to happen in the presence of magnetic fields, hence observing the polarisation of detected light can be a powerful diagnostic tool. There are two types of light polarisation in vacuum to be considered; E modes and B modes. In astronomy, E mode polarisation is thought to occur due to scattering and is common to most of the Universe. The general assumption is that dust grains will align along even weak coherent magnetic fields (see section 1.3.1 earlier). Then when unpolarised background starlight passes through the dust, the polarisation corresponding to the direction of the magnetic field (i.e. the direction that the dust grains align along) will be preferentially absorbed, leaving a net polarised signal in the direction perpendicular to the background magnetic field.

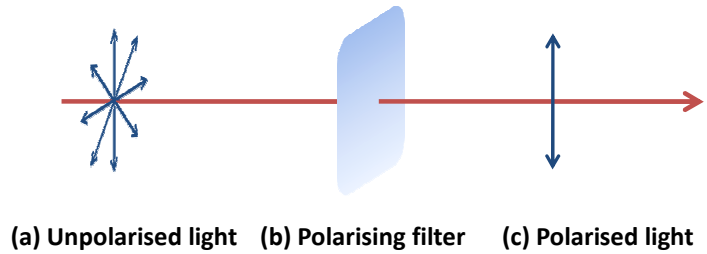

Figure 1.1: (a) Ordinary light is unpolarised, composed of a superposition of electromagnetic waves with electric field vectors aligned in any direction perpendicular to the propagation direction. (b) A polarising filter only allows a single polarisation of light to pass through, resulting in (c) polarised light, where the electric field vectors of all waves in the superposition are aligned along the same direction.

One very useful effect that is commonly used in astronomy is *Faraday rotation* - this occurs when polarised light propagates through a magnetic field *parallel* to the direction of propagation. The polarisation vector actually rotates by an angle (known as the rotation measure) related to the magnitude of the magnetic field and the frequency of the light. Faraday rotation is particularly useful as a diagnostic for measuring the line-of-sight magnetic field in objects that have sources of coherent light behind them, e.g. Andersson and Potter (2005) used three pulsars located behind a molecular cloud to obtain precise measurements of the magnetic field in the cloud.

B mode polarisation is much less common and has currently never been observed: Physically, B-mode polarisation is related to shearing such as the effect of gravitational waves on matter, and would be observable as a curl in a vector field depiction of linear polarisation. It is believed that B mode signals in the microwave background could indicate the effects of primordial gravitational waves in the very early Universe, caused by cosmic inflation. Indeed, some theories have been formulated that put an upper limit on the strength of such gravitational waves, due to the non-detection of B mode polarisation so far (Caprini and Durrer 2002, 2005; Maartens et al. 2001).

1.4 Plasma Modelling Techniques

There are several approaches that can be used to model the physics of plasmas. The most complete method is full kinetic theory, which has the unfortunate drawback of being horrendously complicated. Kinetic theory essentially considers in turn the interaction between each particle and every other particle in the system, with the related electric and magnetic fields calculated self-consistently as the calculations progress. Other modelling techniques include cold plasma theory, which models the plasma to be a pressureless fluid, i.e. fully electromagnetic but not thermodynamic. Another commonly-used model is magnetohydrodynamics (MHD); MHD compromises on the electromagnetism but provides a framework for modelling in the fluid limit with full thermodynamics.

1.4.1 Kinetic Model

The true description of a plasma can only be made when the motion of each of the particles is known (Dendy 1990). However, since any realistic plasma would require billions of particles to be tracked to allow a full solution, such a solution is currently computationally impossible. The best approximation to the true behaviour of a plasma comes from kinetic modelling, in which the plasma is assigned a distribution function f_s. For a three-dimensional system, a 7-dimensional distribution function

$$f_s = f_s(t, x, y, z, w_x, w_y, w_z) = f_s(t, \mathbf{r}, \mathbf{w}) \tag{1.2}$$

is required. A full solution allows the position co-ordinates in configuration space $\mathbf{r} = (x, y, z)$ and the velocity co-ordinates in phase space $\mathbf{w} = (w_x, w_y, w_z)$ of each particle to be tracked (for each species s, at each time t). The distribution function itself represents the number density of particles in phase space. The distribution function is normalised by total number of particles in the plasma N, which can be found by integrating over all phase space:

$$\int \int f_s(t, \mathbf{x}, \mathbf{w}) d^3\mathbf{r} d^3\mathbf{w} = N \tag{1.3}$$

The evolution of the distribution function can be found by solving Boltzmann's equation:

$$\frac{\partial f_s}{\partial t} + \mathbf{w} \cdot \frac{\partial f_s}{\partial \mathbf{r}} + \mathbf{a}_s \cdot \frac{\partial f_s}{\partial \mathbf{w}} = \left(\frac{\partial f_s}{\partial t} \right)_c \tag{1.4}$$

where $\mathbf{r}$, $\mathbf{w}$ and $\mathbf{a}_s$ respectively are the position, velocity and acceleration co-ordinate vectors. The term on the right hand side is the Boltzmann collision term and describes how collisions between particles alter the distribution function. The three terms on the left hand side respectively describe the changes to the distribution function with time, in position space and in velocity space. To account for the effects of external electric and magnetic fields, the Lorentz equation

$$\mathbf{a}_s = \frac{q_s}{m_s} (\mathbf{E} + \mathbf{w}_s \times \mathbf{B}) \tag{1.5}$$

can be substituted for the acceleration term. Solution of these equations represents an enormous computational challenge.

Equilibrium Solution

For the case where the plasma is in thermal equilibrium and there are no external fields present, equation 1.4 reduces to

$$\left(\frac{\partial f_s}{\partial t}\right)_c = 0 \tag{1.6}$$

This represents the equilibrium case, where the plasma is in thermal equilibrium as well as ionisation equilibrium i.e. the ionisation interaction rate from collisions between species is exactly equal to the recombination rate, therefore the proportion of all species in the plasma remains constant.

Considering collisions between a single species, the simplest solution to equation 1.4 consistent with a net zero collision term (equation 1.6) is a Maxwell-Boltzmann distribution (or 'Maxwellian') as follows:

$$f_{MB}(\mathbf{w}) = n\left(\frac{m}{2\pi k_B T}\right)^{\frac{3}{2}} \exp\left(-\frac{m(\mathbf{w}-\bar{\mathbf{w}})^2}{2k_B T}\right) \tag{1.7}$$

where n is the number density, m is the mass and $\mathbf{w}$ is the velocity of the particles in the distribution. The mean, or root mean square (rms) velocity is $\bar{\mathbf{w}}$. The distribution temperature is T and k_B is Boltzmann's constant.

General Solution

For a distribution containing two species which are not in thermal equilibrium, most appropriate form for the collision term in this case[7] for the right hand side of equation 1.4 is the Boltzmann collision term:

$$\left(\frac{\partial f_i}{\partial t}\right)_i = \int (f_i^{(1)'} f_i' - f_i^{(1)} f_i)\sigma_{ii}|\mathbf{v}_i^{(1)'} - \mathbf{v}_i| d\mathbf{v}_i^{(1)} \tag{1.8}$$

for binary collisions between the same species i, where $f_i = f_i(t, \mathbf{r}, \mathbf{v})$ is the distribution function of particles, $f_i^{(1)}$ is the distribution function of the same type of particle but with different velocity (the superscript (1) is included for clarity), and primed quantities

[7] i.e. for binary collisions in this context. Other forms of the collision term such as the Fokker-Planck form exist and are used, for example, in cases where there are multiple collisions simultaneously.

represent the distribution function of the particles immediately after the collision. For example, particles in a distribution have function $f_i = f_i(t, \mathbf{r}, \mathbf{v})$ before a collision and distribution function $f_i' = f_i(t, \mathbf{r}, \mathbf{v}')$ after the collision. σ_{ii} is the cross-section of the same-species collision.

Generalising the Boltzmann term (equation 1.8), the collision term for collisions between particles of species i and a different species j are given as follows:

$$\left(\frac{\partial f_i}{\partial t}\right)_j = \int\int (f_i' f_j' - f_i f_j)\sigma_{ij}|\mathbf{v}_i - \mathbf{v}_j| d\mathbf{v}_j \tag{1.9}$$

where σ_{ij} is the cross-section term for collisions between particles of species i and species j, and $i \neq j$. For example, in a partially-ionised Hydrogen plasma, electrons can collide with other electrons (use equation 1.8), or with protons *or* neutral atoms (use equation 1.9). In thermal and ionisation equilibrium, all collisions transferring energy one way are matched by collisions in the opposite direction, so the net change to the distribution function is zero. In this case, both equation 1.8 and equation 1.9 reduce to zero, returning equation 1.6 for the overall collision term.

1.4.2 Magnetohydrodynamic Fluid Model

Given the computational scale of the full kinetic description of plasma, it is perhaps not surprising that several alternative descriptions have been developed. These descriptions contain simplifying approximations that are usually valid within a particular range of physical conditions. For example, ideal magnetohydrodynamics (MHD) is a fluid approximation which is successful and valid as long as the plasma satisfies the following conditions (Dendy 1990):

1. The plasma remains in thermal equilibrium, i.e. the particle distribution is approximately Maxwellian. This means the timescale between collisions must be shorter than any other timescale in the plasma.

2. The plasma must have high conductivity, and the magnetic diffusion timescale must be longer than any other timescale. There are resistive approximations of

MHD which relax this condition.

3. The system must evolve over timescales no shorter than the fluid timescale. It is only valid to consider low-frequency, long-wavelength perturbations. For example, the fluid model is meaningless over timescales as short as, say, the ion cyclotron frequency. This is the most commonly violated restriction on MHD.

Single-fluid ideal MHD

The fluid model is found by deriving the moments of the kinetic equations. Fluid models can be at most 4-dimensional, i.e. over position space and time. To find the moments, the Boltzmann equation (1.4) must be integrated over the full velocity space. The zeroth moment gives the continuity equation, or mass conservation law:

$$\begin{aligned} \int \left(\frac{\partial f_s}{\partial t} + \mathbf{w} \cdot \frac{\partial f_s}{\partial \mathbf{r}} + \mathbf{a}_s \cdot \frac{\partial f_s}{\partial \mathbf{w}} \right) d^3\mathbf{w} &= \int \left(\frac{\partial f_s}{\partial t} \right)_c d^3\mathbf{w} \\ \Rightarrow \frac{\partial n_s}{\partial t} + \nabla \cdot (n_s \bar{\mathbf{w}}_s) &= 0 \end{aligned} \tag{1.10}$$

This is the standard fluid continuity equation. The first moment of equation 1.4 can be found as follows:

$$\begin{aligned} \int \left(\frac{\partial f_s}{\partial t} + \mathbf{w} \cdot \frac{\partial f_s}{\partial \mathbf{r}} + \mathbf{a}_s \cdot \frac{\partial f_s}{\partial \mathbf{w}} \right) \mathbf{w} d^3\mathbf{w} &= \int \left(\frac{\partial f_s}{\partial t} \right)_c \mathbf{w} d^3\mathbf{w} \\ \Rightarrow n_s m_s \left(\frac{\partial}{\partial t} + \bar{\mathbf{w}}_s \cdot \nabla \right) \bar{\mathbf{w}}_s + \nabla p_s - n_s q_s (\mathbf{E} + \bar{\mathbf{w}}_s \times \mathbf{B}) &= 0 \end{aligned} \tag{1.11}$$

Equation 1.11 is the equation of motion, or the momentum equation of the fluid.

To close the system of equations, an energy relation must be assumed. The adiabatic gas law is one possible relation:

$$\left(\frac{\partial}{\partial t} + \bar{\mathbf{v}}_s \cdot \nabla \right) (p_s [n_s m_s]^{-\gamma}) = 0 \tag{1.12}$$

with the constant $\gamma = 5/3$.

After further derivation, the complete set of single-fluid ideal MHD equations is as follows:

$$\dot{\rho} = -\nabla \cdot (\rho \mathbf{w}) \tag{1.13}$$

$$\rho\dot{\mathbf{w}} + \rho(\mathbf{w}\cdot\nabla)\mathbf{w} = -\nabla p + \mathbf{J}\times\mathbf{B} \tag{1.14}$$

$$\dot{\mathbf{B}} = \nabla\times(\mathbf{w}\times\mathbf{B}) \tag{1.15}$$

$$p \propto \rho^{\gamma_a} \tag{1.16}$$

where ρ, $\mathbf{w}$ and p are the plasma density, velocity field and pressure respectively, $\mathbf{J}$ is the current density and $\mathbf{B}$ is the magnetic flux density. The adiabatic constant $\gamma_a = 5/3$ governs the equation of state, and the usual dot notation indicates a time derivative. These equations describe the equilibrium case (i.e. ionisation and recombination reactions in the plasma are balanced), therefore there are no source or sink terms in the continuity equation 1.13, and no net ionisation/neutralisation terms in the momentum equation 1.14. The collisional aspects of the plasma are represented by the scalar pressure, and the fluid is inviscid.

1.4.3 Multi-fluid Models

Single-fluid ideal MHD is a simplified model in which fluid elements are plasma, and since there is no charge separation in the reduced electromagnetism that is included in the model, the concept of populations of ions and electrons is not compatible with MHD. However, it *is* possible to model multiple populations in the fluid limit. As a general example, consider a partially-ionised plasma containing three populations: this ternary mixture includes electrons, ions and neutral atoms. Assigning the subscripts e, i, and a respectively to denote each population, it can be shown by finding the moment equations (exactly as for equations 1.10 and 1.11) that the multi-fluid equations are as follows:

- Continuity equations

$$\begin{aligned} \dot{\rho}_e + \nabla\cdot(\rho\mathbf{w}_e) &= S_e \\ \dot{\rho}_i + \nabla\cdot(\rho\mathbf{w}_i) &= S_i \\ \dot{\rho}_a + \nabla\cdot(\rho\mathbf{w}_a) &= S_a \end{aligned} \tag{1.17}$$

- Momentum equations

$$\begin{aligned}
\rho\dot{\mathbf{w}}_e + \rho(\mathbf{w}_e \cdot \nabla)\mathbf{w}_e &= -\nabla p + n_e q_e \left[\mathbf{E} + (\mathbf{w}_e \times \mathbf{B})\right] + \Gamma_e \\
\rho\dot{\mathbf{w}}_i + \rho(\mathbf{w}_i \cdot \nabla)\mathbf{w}_i &= -\nabla p + n_i q_i \left[\mathbf{E} + (\mathbf{w}_i \times \mathbf{B})\right] + \Gamma_i \\
\rho\dot{\mathbf{w}}_a + \rho(\mathbf{w}_a \cdot \nabla)\mathbf{w}_a &= -\nabla p + \Gamma_a
\end{aligned} \tag{1.18}$$

where n_s and q_s are the number density and charge of each species. The S terms in equations 1.17 are sources or sinks of each species. These are only non-zero in a non-equilibrium system where ionisations and neutralisations are unbalanced. The Γ terms in equations 1.18 represent momentum transfer between populations e.g. when ions and neutral atoms collide this can transfer momentum from one fluid to the other. The Γ terms may also include the effect of ionisations and neutralisations, in non-equilibrium models where these are taken into account.

Assuming ionisation equilibrium[8], then $S_s = 0$ and the Γ terms include only the momentum transfer due to collisions between the fluid species. The Γ terms depend only on the fluid densities and the differential velocity between the species. For example, the momentum exchange between the ions and neutral atoms (and vice versa) is given by:

$$\Gamma_{ia} = \Gamma_{ai} = \pm\frac{\rho_i}{\tau}|\mathbf{w}_i - \mathbf{w}_a| \tag{1.19}$$

where τ is analogous to a coefficient of friction. The form of equation 1.19 is the result of using the Boltzmann term (equation 1.9) as the collision term in equation 1.4 while integrating to find the fluid equations.

1.4.4 Two-Fluid Partially-Ionised MHD Model

By following through the derivation of a ternary mixture in section 1.4.3 (see also Jancel and Kahan (1966)), the equations describing a binary mixture of MHD and

[8] i.e. ionisation and recombination reactions in the plasma are balanced, and the difference in chemical potential means that collisions between the plasma and neutral gas do not change the relative densities of either fluid.

neutral gas can be derived[9]:

- Continuity Equations:

$$\dot{\rho} = -\nabla \cdot (\rho \mathbf{w}) \tag{1.20}$$

$$\dot{\hat{\rho}} = -\nabla \cdot (\hat{\rho} \mathbf{v}) \tag{1.21}$$

  where respectively ρ and $\mathbf{w}$ are the plasma density and velocity field, and $\hat{\rho}$ and $\mathbf{v}$ are the neutral gas density and velocity field.

- Momentum Equations:

$$\rho \dot{\mathbf{w}} + \rho(\mathbf{w} \cdot \nabla)\mathbf{w} = -\nabla p + \mathbf{J} \times \mathbf{B} + \Gamma \tag{1.22}$$

$$\hat{\rho} \dot{\mathbf{v}} + \hat{\rho}(\mathbf{v} \cdot \nabla)\mathbf{v} = -\nabla \hat{p} - \Gamma \tag{1.23}$$

  where $\mathbf{J}$ is the current density and $\mathbf{B}$ is the magnetic flux density. The plasma pressure is p and the neutral gas pressure denoted by $\hat{p}$

- Other equations: To complete the initial set of equations, the magnetic field equation is required, and each fluid has an adiabatic equation of state:

$$\dot{\mathbf{B}} = \nabla \times (\mathbf{w} \times \mathbf{B}) \tag{1.24}$$

$$p \propto \rho^{\gamma_a} \tag{1.25}$$

$$\hat{p} \propto \hat{\rho}^{\gamma_a} \tag{1.26}$$

  The adiabatic constant $\gamma_a = 5/3$ governs the equations of state. The usual dot notation denotes a time derivative.

Now the Γ in the momentum equations is of the form shown in equation 1.19, specifically $\Gamma = \rho/\tau|\mathbf{w} - \mathbf{v}|$ and accounts for momentum transfer between the plasma and neutral gas, facilitated by collisions between particles of each species. The terms are

[9] In MHD theory there is no charge separation, therefore no electron population can be considered: the ion equations lead to the MHD equations.

equal and opposite in each equation so that any momentum lost to one fluid is transferred to the other, and vice versa. In this fluid limit, it is the differential motion of the velocity fields which provides the transfer of momentum, effectively via friction.

Notice that this model was derived assuming ionisation equilibrium (as shown in section 1.4.3) which is required in order to satisfy the basic assumption that in MHD there is no charge separation. Therefore the source and sink terms are all equal to zero. This partially-ionised plasma model will be used in chapters 2 and 3.

1.4.5 Cold Model

Cold plasma is another approximate model that covers a fairly wide parameter range. Formally it is valid for all length scales, as long as random, thermal motion is negligible and the plasma can be considered to be pressureless. The full set of linearised cold plasma equations is (Dendy 1990):

$$\frac{\partial n_s}{\partial t} + n_s \nabla \cdot \mathbf{w}_s = 0 \tag{1.27}$$

$$m_s \dot{\mathbf{w}}_s - q_s \left(\mathbf{E} + \mathbf{w}_s \times \mathbf{B}\right) = 0 \tag{1.28}$$

$$\mathbf{J} = \Sigma_s n_s q_s \mathbf{w}_s \tag{1.29}$$

where q_s is the charge of particle species s and $\mathbf{J}$ is the current density. These equations are supplemented by the full set of Maxwell's equations, i.e. unlike in MHD, a cold plasma is fully electromagnetic:

$$\nabla \times \mathbf{E} = -\frac{\partial \mathbf{B}}{\partial t} \tag{1.30}$$

$$\nabla \times \mathbf{B} = \mu_0 \mathbf{J} + \frac{1}{c^2}\frac{\partial \mathbf{E}}{\partial t} \tag{1.31}$$

$$\nabla \cdot \mathbf{E} = \frac{\rho_c}{\epsilon_0} \tag{1.32}$$

$$\nabla \cdot \mathbf{B} = 0 \tag{1.33}$$

where $\mathbf{E}$ is the electric field, $\mathbf{B}$ is the total magnetic field, $\mathbf{J}$ is the current density, and ρ_c is the density of free charge. ϵ_0 is the permittivity of free space, μ_0 is the permeability of free space and c is the speed of light in vacuum.

The cold plasma interpretation allows the detailed study of important plasma properties such as the various characteristic oscillations discussed in section 1.5.2, and the dielectric and refractive properties of plasma. Cold plasma theory is mentioned here for the sake of completeness, but will not be used in this thesis.

1.5 Characteristic Plasma Dynamics

Every plasma has a set of characteristic scale lengths and frequencies. These are important in whichever regime one is working. Even in MHD, which formally has no individual charges, the ion cyclotron frequency places an important lower limit on timescales that the theory is valid for.

1.5.1 The Debye Sphere

The Debye length is the characteristic length related to plasma behaviour - over length scales shorter than the Debye length the quasi-neutrality condition does not hold, and effects such as plasma oscillations and electromagnetic inter-particle forces dominate. Over scales longer than the Debye length, collective effects dominate.

To illustrate the derivation, consider a uniform electron-positive ion plasma in thermal equilibrium, with temperature T. Random thermal fluctuations will affect the electrons more than the ions, because the electrons are far more mobile. Considering a 1-D slice, this means a zone of electron depletion of some length d will be created by fluctuations. Solving Gauss' equation (1.32) leads to the expression for the electric potential ϕ of this region:

$$\phi(x) = \frac{n_p q_p (d^2 - x^2)}{2\epsilon_0} \tag{1.34}$$

where x is the distance co-ordinate, d is the maximum extent of the electron-depleted region, n_i is the ion number density, e is the electron charge, and ϵ_0 is the permittivity of free space.

The maximum size d of the region can be found by equating the maximum potential

energy with the thermal energy $\frac{1}{2}k_BT$ (recall this is for one dimension):

$$\begin{aligned} \frac{1}{2}k_BT &= e\phi(0) \\ &= \frac{ne^2d^2}{2\epsilon_0} \end{aligned} \tag{1.35}$$

which can be rearranged to find λ_D, the Debye length:

$$\lambda_D = d = \left(\frac{\epsilon_0 k_B T}{n_i e^2}\right)^{\frac{1}{2}} \tag{1.36}$$

This is shown in figure 1.2. Any charge imbalance occurring due to fluctuations in the plasma will be shielded over length scales greater than λ_D, meaning that the plasma is quasi-neutral on scales $> \lambda_D$. Extending this to three dimensions, the Debye sphere is the volume within which charge imbalances dominate electrostatically.

1.5.2 Plasma Frequency

Since the plasma shields electric fields over length scales greater than the Debye length, this means there must be some kind of restoring force that prevents charge separation over these large scales. Considering a plasma averaged over such scales, the continuity equation can be used to investigate perturbations to the number density n.

$$\frac{\partial n}{\partial t} + \nabla \cdot (n\mathbf{v}) = 0 \tag{1.37}$$

where $\mathbf{v}$ is the fluid velocity, i.e. the averaged velocity over the bulk plasma. Since the electrons are far more mobile than the ions, any perturbation will lead to a charge separation and hence an electric field $\mathbf{E}$, according to Gauss' equation (1.32). The charges in the plasma will be accelerated by this

$$m_e \frac{d\mathbf{v}}{dt} = -e\mathbf{E} \tag{1.38}$$

where m_e and e are the electron mass and charge respectively. Then assuming the perturbation n_1 to initial number density n_0 is small, the system to be solved consists

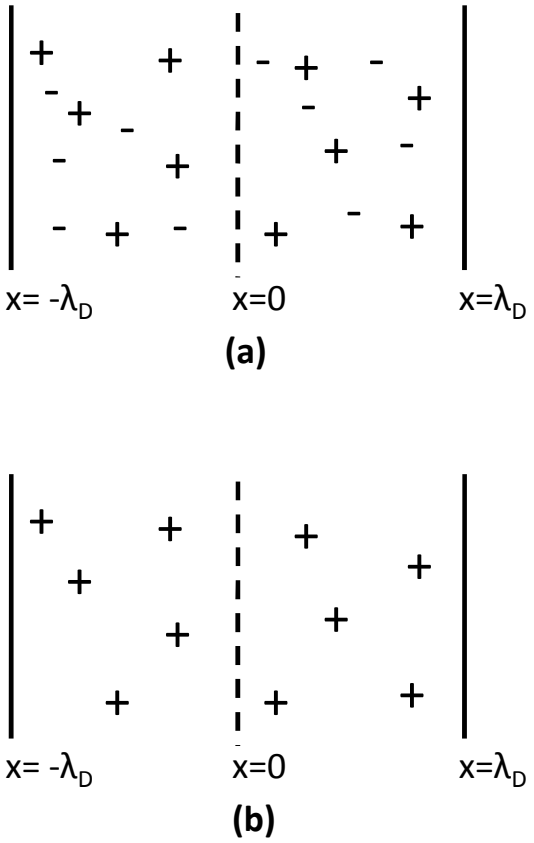

Figure 1.2: Consider a small region of length $2\lambda_D$ in a plasma as shown in the figure above. λ_D is the Debye length, which is the maximum length scale over which random thermal fluctuations in the plasma can be cancelled out by the restoring Coulomb force in the plasma. The figure shows: (a) A 1-D slice of a quasi-neutral plasma. The + represent protons and the − represent electrons. The charge is balanced, i.e. the plasma is locally quasi-neutral. (b) A random thermal fluctuation affects the more mobile electrons more than the protons, creating a temporary zone of electron depletion. This charge separation means a restoring Coulomb force is induced, which then returns the electrons to the depleted zone. Energy considerations show that the characteristic length of the temporary depletion zone is λ_D, the Debye length. Over length scales greater than λ_D, any charge imbalance in the plasma is shielded and the plasma is quasi-neutral.

of three linear equations:

$$\frac{\partial n_1}{\partial t} + n_0 \nabla \cdot \mathbf{v}_1 = 0 \tag{1.39}$$

$$m_e \frac{d\mathbf{v}_1}{dt} = -e\mathbf{E}_1 \tag{1.40}$$

$$\nabla \cdot \mathbf{E}_1 = -\frac{n_1 e}{\epsilon} \tag{1.41}$$

which combine to one equation,

$$\frac{\partial^2 n_1}{\partial t^2} + \frac{n_0 e^2}{\epsilon_0 m_e} n_1 = 0 \tag{1.42}$$

Equation 1.42 is an expression for simple harmonic motion with frequency

$$\omega = \omega_{p,e} = \left(\frac{n_0 e^2}{\epsilon_0 m_e} \right)^{\frac{1}{2}} \tag{1.43}$$

where $\omega_{p,e}$ is the electron plasma frequency. Fluctuations that cause separation will induce an oscillation at frequency $\omega_{p,e}$ in the plasma until quasi-neutrality has been restored. This means that fluctuations made to the plasma with frequency less than or equal to the plasma frequency will be absorbed by the electron motion. This has implications for electromagnetic radiation - for light of frequency $\omega \leq \omega_{p,e}$ the electron motion produces a conduction current that cancels out the displacement current of the wave, fully absorbing it. This is why plasmas are opaque to radiation below the plasma frequency. For frequency $\omega > \omega_{p,e}$, the electrons cannot accelerate quickly enough to cancel the electromagnetic radiation, therefore the wave can propagate through the plasma.

1.5.3 Electron and Ion Cyclotron Frequency

Consider the motion of particles in a magnetised plasma with a uniform, constant magnetic field **B** and zero electric field. The motion of a single particle with charge q and mass m will evolve according to the Lorentz equation

$$m\frac{d\mathbf{v}}{dt} = q\mathbf{v} \times \mathbf{B} \tag{1.44}$$

Assuming the magnetic field is non-zero in the z-direction only, i.e. $\mathbf{B} = B\hat{\mathbf{z}}$, the components of this are as follows:

$$\frac{dv_x}{dt} = \frac{q}{m}Bv_y \tag{1.45}$$

$$\frac{dv_y}{dt} = -\frac{q}{m}Bv_x \tag{1.46}$$

$$\frac{dv_z}{dt} = 0 \tag{1.47}$$

where the components of the velocity vector are $\mathbf{v} = (v_x, v_y, v_z)$. Equation 1.47 says the particle moves with a constant velocity in the z-direction. The time derivatives of equations 1.45 and 1.46 are

$$\frac{d^2v_x}{dt^2} = -\left(\frac{qB}{m}\right)^2 v_x \tag{1.48}$$

$$\frac{d^2v_y}{dt^2} = -\left(\frac{qB}{m}\right)^2 v_y \tag{1.49}$$

Equations 1.48 and 1.49 describe simple harmonic motion at frequency

$$\omega_c = \frac{|q|B}{m} \tag{1.50}$$

This is the cyclotron frequency. In an electron-ion plasma there will be two cyclotron frequencies - $\omega_{c,e}$ for the electrons and $\omega_{c,i}$ for the ions. The solutions to equations 1.48 and 1.49 are the expressions for circular motion, known as 'gyro' motion, at the cyclotron frequency:

$$v_x = v_\perp \cos(\omega_c t) \tag{1.51}$$

$$v_y = \pm v_\perp \sin(\omega_c t) \tag{1.52}$$

where the $\pm$ sign depends on the sign of the charge. Note that $v_\perp$ is the component of velocity that is perpendicular to the magnetic field. The cyclotron frequencies describe the gyro motion of electrons and ions in a magnetised plasma, and also define important timescales.

Larmor Radius

The gyro motion of charged particles in a magnetic field is also known as a Larmor orbit. The radius of this orbit about the guiding centre is given by

$$r_L = \frac{v_\perp}{\omega_c} = \frac{mv_\perp}{|q|B} \tag{1.53}$$

This is a characteristic minimum scale length for several plasma effects.

1.5.4 Plasma Drifts

The idea of gyro motion is an important concept as part of understanding the behaviour of single particles in plasmas. Particles move in orbits around a 'guiding centre' - a point that is not necessarily stationary. Guiding centres have various mechanisms which make them move, usually when external electric fields are introduced into the plasma.

E x B Drift

Consider a magnetised plasma with uniform, constant magnetic field $\mathbf{B} = B\hat{\mathbf{z}}$ and uniform, constant electric field $\mathbf{E} = -E_x\hat{\mathbf{x}} + E_z\hat{\mathbf{z}}$, i.e. with components of electric field parallel and perpendicular to the magnetic field. Then the particle equations of motion are

$$\frac{dv_x}{dt} = \frac{q}{m}(-E_x + Bv_y) \tag{1.54}$$

$$\frac{dv_y}{dt} = -\frac{q}{m}Bv_x \tag{1.55}$$

$$\frac{dv_z}{dt} = \frac{q}{m}E_z \tag{1.56}$$

The time derivatives of equations 1.54 and 1.55 are

$$\frac{d^2v_x}{dt^2} = \omega_c\frac{dv_y}{dt} = -\omega_c^2 v_x \tag{1.57}$$

$$\frac{d^2v_y}{dt^2} = -\omega_c\frac{dv_x}{dt} = -\omega_c^2\left(\frac{-E_x}{B} + v_y\right) \tag{1.58}$$

which are second-order differential equations similar to, but not exactly, simple harmonic motion. Solutions to equations 1.57 and 1.58 are, using the usual complex exponential for periodic functions;

$$v_x = v_0 \exp(i\omega_c t) \tag{1.59}$$

$$v_y = v_0 \exp(i\omega_c t) + \frac{E_x}{B} \tag{1.60}$$

In fact, this is the gyro motion derived in section 1.5.3 with an additional drift in the positive y-direction. The gyro motion no longer describes closed circles - the guiding centre of the particle motion moves in the direction of the drift (see figure 1.3). This is known as the $\mathbf{E} \times \mathbf{B}$ drift because the direction in which the guiding centre moves is the direction perpendicular to both the electric field and magnetic field. The guiding centre velocity $\mathbf{v}_{gc}$ is given by the expression

$$\mathbf{v}_{gc} = \frac{\mathbf{E} \times \mathbf{B}}{|B|^2} \tag{1.61}$$

This depends only on the magnitude and direction of the electric and magnetic fields, and *not* on the charge or mass of the particle. Therefore electrons and ions are affected equally by the $\mathbf{E} \times \mathbf{B}$ drift, and the guiding centres of both move in the same direction at the same speed.

Other Particle Drifts

Other kinds of particle drifts exist in plasmas which have non-uniform background magnetic fields. The *grad-B* drift happens in a spatially-varying background field; positive and negative particles drift in opposite directions perpendicular to the direction of the field and the field gradient. An effect related to the grad-B drift is *curvature drift*, which in practice always accompanies the grad-B drift in curved magnetic field and acts in the same direction. Understanding these effects is particularly important, for example, for maintaining magnetic confinement in tokamaks. The tokamak field configuration means that both the grad-B drift and the curvature drift act to make ions drift towards the walls of the tokamak, risking the loss of confinement.

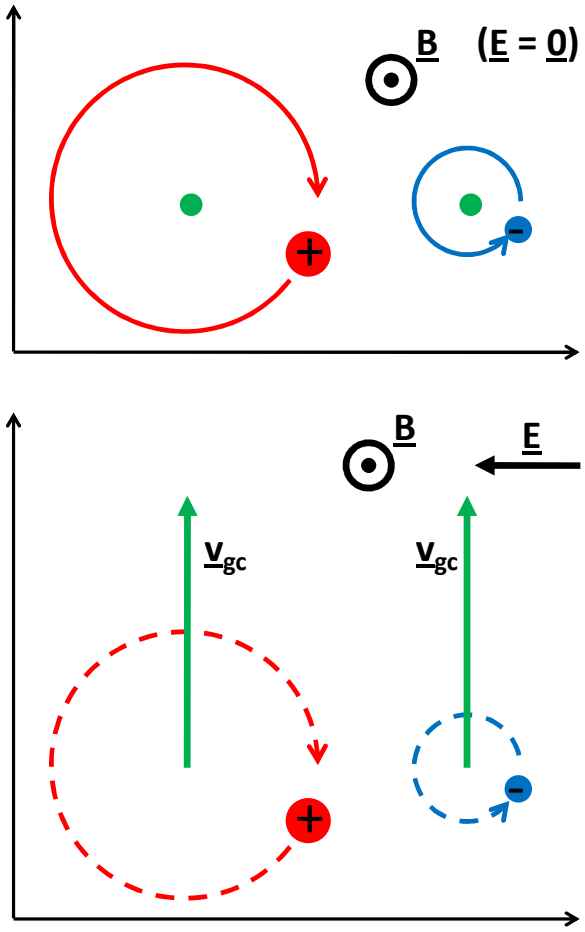

Figure 1.3: The top figure shows the gyro motion of a moving proton and electron in a constant, uniform background magnetic field pointing out of the page. The particles each orbit a guiding centre (shown in green), with the proton executing an orbit with a larger radius and in the opposite direction to the electron. The radii are not to scale.

The bottom figure shows the drift motion acquired by the particles if a constant, uniform electric field is present in the direction shown. The guiding centres of both the proton and electron drift upwards, in the direction perpendicular to both the electric and magnetic fields (i.e. in the direction of $(\mathbf{E} \times \mathbf{B})$) at *the same velocity* $\mathbf{v}_{gc}$. The gyro motion is still happening, but the particles no longer move in closed circles. The full motion of each is more complex.

1.6 MHD Wave Modes

Plasmas support many different wave modes. The various descriptions of plasma allow these wave modes to be studied theoretically in different limits - for example, cold plasma theory can be used to derive various high-frequency electrostatic wave modes such as the plasma oscillation and cyclotron waves. In the fluid limit under MHD, a dispersion relation can be derived, the interpretation of which reveals three unique wave modes are supported in the MHD regime. These are transverse Alfvén waves, and the fast and slow magnetosonic modes.

The derivation of the dispersion relation begins with the full set of MHD equations (Dendy 1990). The fluid equations are

$$\frac{\partial \rho}{\partial t} + \nabla \cdot (\rho \mathbf{u}) = 0 \tag{1.62}$$

$$\rho \frac{D\mathbf{u}}{Dt} + \nabla p - \mathbf{J} \times \mathbf{B} = 0 \tag{1.63}$$

$$\frac{D}{Dt} (p\rho^{-\gamma_a}) = 0 \tag{1.64}$$

$$\tag{1.65}$$

where ρ is the total plasma density, $\mathbf{u}$ is the bulk fluid velocity, and $D/Dt = \partial/\partial t + \mathbf{u} \cdot \nabla$ is the advective derivative. The fluid pressure is p, $\mathbf{J}$ is the current density and $\mathbf{B}$ is the background magnetic field. For an adiabatic equation of state, $\gamma_a = 5/3$ is a constant. The fluid equations are supplemented by the reduced electromagnetic equations:

$$\mathbf{E} = -\mathbf{u} \times \mathbf{B} \tag{1.66}$$

$$\nabla \times \mathbf{E} = -\frac{\partial \mathbf{B}}{\partial t} \tag{1.67}$$

$$\nabla \times \mathbf{B} = \mu_0 \mathbf{J} \tag{1.68}$$

$$\nabla \cdot \mathbf{E} = 0 \tag{1.69}$$

$$\nabla \cdot \mathbf{B} = 0 \tag{1.70}$$

Equation 1.66 is the ideal MHD perfect conductivity equation, the rest are Maxwell's equations, two of which have been reduced from their full form.

The dispersion relation is derived by considering the response of the plasma to perturbations of the form

$$\exp(i[\mathbf{k}\cdot\mathbf{r}-\omega t) \tag{1.71}$$

where $\mathbf{k} = k_{\parallel}\hat{\mathbf{z}} + k_{\perp}\hat{\mathbf{y}}$ is the wavenumber vector with components parallel and perpendicular to the magnetic field $\mathbf{B} = B\hat{\mathbf{z}}$.

Eventually, the dispersion relation can be written in matrix form as

$$\begin{bmatrix} \omega^2 - v_A^2 k_{\parallel}^2 & 0 & 0 \\ 0 & \omega^2 - v_A^2 k_{\parallel}^2 - (v_S^2 + v_A^2)k_{\perp}^2 & -v_S^2 k_{\parallel} k_{\perp} \\ 0 & -v_S^2 k_{\parallel} k_{\perp} & \omega^2 - v_S^2 k_{\parallel}^2 \end{bmatrix} \begin{bmatrix} u_x \\ u_y \\ u_z \end{bmatrix} = \begin{bmatrix} 0 \\ 0 \\ 0 \end{bmatrix} \tag{1.72}$$

The characteristic speeds v_A and v_S are the Alfvén speed and sound speed in the plasma respectively.

1.6.1 Transverse Alfvén Waves

Focusing on the u_x line of the dispersion relation, the equation

$$\omega^2 = v_A^2 k_{\parallel}^2 \tag{1.73}$$

emerges. This is the dispersion relation of the normal mode known as the *transverse Alfvén mode*, which is an electromagnetic wave completely parallel to the magnetic field and is dispersionless, i.e. the wave speed does not depend on wave frequency. The wave mode is transverse because although it propagates in the z-direction along the direction of the background magnetic field, the perturbations to the plasma velocity field occur only in the x-direction. In MHD, transverse Alfvén waves are completely analogous to waves on a string.

1.6.2 Magnetosonic Modes

Similarly, the dispersion relation in the other directions returns the expressions for other wave modes. There are two solutions, these are

$$\omega^2 = \frac{k^2}{2}\left[(v_S^2 + v_A^2) \pm \left((v_S^2 - v_A^2)^2 + 4v_S^2 v_A^2 \frac{k_{\perp}^2}{k^2}\right)^{\frac{1}{2}}\right] \tag{1.74}$$

The positive option of the ± gives the *fast magnetosonic mode*, the negative option gives the *slow magnetosonic mode*. Both modes are pressure waves that propagate in any direction except parallel to the magnetic field, according to the dispersion relation. The wavenumber term $k = \sqrt{k_\perp^2 + k_\parallel^2}$ includes components from both the parallel and perpendicular directions to the magnetic field.

The magnetosonic modes are like any other pressure wave modes, except as they propagate the magnetic pressure related to the background magnetic field can either support or oppose the hydrostatic pressure disturbance. If the magnetic pressure is perturbed in phase with the hydrostatic pressure, the fast mode is the response. If the magnetic pressure opposes the hydrostatic pressure, the slow mode is implicated.

1.6.3 Firehose Instability

Like any fluid, MHD plasmas are susceptible to non-linear behaviour such as instabilities. One that affects transverse Alfvén waves in particular is the *firehose instability*. Assume that the plasma has a pressure tensor as follows:

$$\underline{\underline{p}} = \begin{bmatrix} p_\perp & 0 & 0 \\ 0 & p_\perp & 0 \\ 0 & 0 & p_\parallel \end{bmatrix} \tag{1.75}$$

That is, the pressure $p_\perp$ is consistent in both directions perpendicular to the magnetic field, but different ($p_\parallel$) in the parallel direction. This allows for anisotropic transport such as that seen in magnetised plasma, while setting the non-diagonal terms to zero maintains the inviscid nature of the fluid.

The tensor structure also means that there are two sound speeds in the plasma, $v_{S,\perp}$ and $v_{S,\parallel}$. There are two possible wave modes supported by the plasma in the parallel direction to the magnetic field. The first is a transverse Alfvén wave with the dispersion relation

$$\omega^2 = k^2(v_A^2 + v_{S,\perp}^2 - v_{S,\parallel}^2) \tag{1.76}$$

$$= \frac{k^2}{\rho_0}\left(\frac{B_0^2}{\mu_0} + p_{\perp,0} - p_{\parallel,0}\right) \tag{1.77}$$

where the subscript 0 denotes the initial, unperturbed quantity. The other potential wave mode in the parallel direction corresponds to an ion sound wave, and has a dispersion relation

$$\omega^2 = 3k^2 \frac{p_{\parallel,0}}{\rho_0} \tag{1.78}$$

Consider the transverse Alfvén mode, given in equation 1.77. Assuming that perturbations to the velocity field have the form

$$\mathbf{v}_1 \propto \exp(i[\mathbf{k} \cdot \mathbf{r} - \omega t]) \tag{1.79}$$

it is clear that if $\omega^2 < 0$ then $\omega \in \mathbb{C}$, meaning $\mathbf{v}_1$ acquires an exponentially growing or decaying term. Therefore the condition for stability of a transverse Alfvén wave is $\omega^2 \geq 0$. This means that according to equation 1.77, a transverse Alfvén wave will become unstable if

$$p_{\parallel,0} > \frac{B_0^2}{\mu_0} + p_{\perp,0} \tag{1.80}$$

The physical interpretation of this is that if the parallel pressure exceeds the sum of the perpendicular hydrostatic pressure and the magnetic pressure of the wave, the restoring force of the wave is unable to slow some of the plasma motion. Therefore each half wave cycle some of the plasma will continue moving in the direction perpendicular to the direction of travel of the wave. The result is an Alfvén wave that will rapidly disperse its energy into sonic/magnetosonic modes and be absorbed into the plasma. Picture a real-life firehose which has the water switched on with no-one holding it: the hose will flail around sending water everywhere. This analogy is where the name of the instability comes from, as the plasma is perturbed in a very similar manner.

1.7 Thesis Outline

The following chapters can be grouped into two distinct parts. The first part will deal with partially-ionised, inhomogeneous and recombining plasmas in the fluid limit - specifically these three chapters will address the propagation of plasma wave modes

in such plasmas. In chapter 2 a fluid model of partially-ionised plasmas will be developed, and the computational model will be derived. This model is put into use in chapter 3, in which results of the simulations will be presented. The results will show that given the high-precision polarisation data now available, the Chandrasekhar-Fermi observational method could, with some refinement, be used to interpret the data giving unprecedented diagnosis of astrophysical magnetic fields.

In the second part of this thesis, chapters 4 and 5 will address the specific issue of charge acceleration due to magnetic collapse during the neutralisation of a self-magnetised plasma. The theoretical and computational model developed in chapter 4 will be put into practice in chapter 5, with the results showing that a natural consequence of the epoch of recombination in the early Universe is a persistent small population of energetic charges. Chapter 6 will conclude, and examine the plentiful potential for future work.

"Reality is that which, when you stop believing in it, doesn't go away."

Philip K. Dick

2

Fluid Model of a Partially-Ionised Plasma

In this chapter a fluid model describing partially-ionised plasma will be developed. This chapter builds on work originally carried out by Diver et al. (2006) where the importance of partially-ionised plasma interspecies interaction by momentum coupling was demonstrated. The motivation for this is to analyse the plasma-neutral interaction *ab initio* without making any assumptions about the nature of the interaction. A specific example of an assumption to be avoided is the relation of "turbulence" to the plasma and neutral gas behaviour[1]. In considering the behaviour of the plasma-neutral mixture from first principles, the model accounts for the fact that the plasma-neutral interaction is complex and must be given a more careful treatment than it has been afforded up until now in the literature.

The specific context for immediate application of this work, which will be developed in the next chapter, is to a diagnostic known as the Chandrasekhar-Fermi method, used to infer magnetic flux density in astrophysical objects such as nebulae, molecular clouds or galactic spiral arms. However, the description "partially-ionised" can refer to any low-temperature plasma such as, for example, the start-up phase or the

[1]The notion of turbulence in this context is flawed since in the fluid limit, all random, incoherent motion is by definition averaged out over the larger scale bulk motion.

cooler edge regions during operation of tokamaks. Analogous situations where this work could also have relevance include dusty plasmas and plasmas with multiple ion populations. A general point that requires emphasis is that when dealing with a fluid composed of a mixture of two different populations, the interaction *between* the two populations cannot be neglected. The model developed in this chapter will address this, and will be extendable to any such mixture given the correct choice of parameters for computation.

2.1 Wave Modes

The fundamental principle of this model holds that as long as the conditions for magnetohydrodynamics (MHD) are satisfied, any partially-ionised or inhomogeneous plasma can be modelled as a cospatial mixture of two populations: one an MHD plasma and the other an ordinary neutral gas[2]. Indeed it is necessary to consider such a mixture when modelling low-frequency perturbations such as Alfvén wave modes since, as will be shown, the interaction between the two populations can be quite complex.

In the 2-D linear limit, the coupling between the two populations can be modelled by a momentum exchange operator motivated by the Boltzmann collision term (see section 1.4.3). In a mixture of this kind the character of a propagating wave in one population is altered by additional wave modes which it induces in the other population. For example, sound waves in the neutral gas can indirectly induce magnetic perturbations in the plasma, and conversely purely magnetic disturbances can cause density perturbations in the neutral gas. Even infinite plane Alfvén waves, which do not cause density perturbations in the plasma[3], can indirectly perturb the neutral gas density as momentum transfers to perturb the velocity field of the neutral population.

[2]The same also applies to any multi-species plasma, which can be modelled as a mixture of two populations of MHD plasma with different mass density.

[3]In this case the Alfvén wave contributes only an oscillating velocity structure along with the characteristic magnetic perturbations.

This is significant because transverse Alfvén waves cannot affect a population of neutral gas directly, because neutral atoms are not perturbed by the variation in magnetic field, and do not contribute to the magnetic pressure.

It is the *momentum exchange* between the plasma and the neutral population that allows this mode conversion: so when the plasma moves, it collides with the neutral gas and drags it along, and vice versa. This is proportional to density (equation 1.19) and differential velocity between the fluids. For the example of a transverse Alfvén wave, the perturbations to the plasma velocity field are accompanied by associated perturbations to the neutral gas velocity field. This causes density perturbations to develop in the neutral gas, which then propagate as ordinary sonic waves at the neutral sound speed. These sonic modes can then cause new perturbations in the plasma, in the form of more sonic or magnetosonic waves. This means the plasma can acquire further density perturbations from the Alfvén wave indirectly, via the neutral gas population.

In fact neither gas medium responds in a normal mode, so the neutral gas doesn't have perfect sound waves, and the plasma doesn't have perfect magnetosonic modes either. Potentially, any perturbation to either population will produce a superposition of many different wave modes. This is a consequence only of the linear process of collisional momentum exchange, rather than any nonlinear effect.

2.2 Theory

The model equations are derived as follows. The computational model was first derived by Diver et al. (2006). Begin with the two-fluid partially-ionised plasma model developed in chapter 1. Recall equations 1.20 - 1.26 to describe the plasma-neutral gas mixture:

- Continuity Equations:

$$\dot{\rho} = -\nabla \cdot (\rho \mathbf{w}) \tag{2.1}$$

$$\dot{\hat{\rho}} = -\nabla \cdot (\hat{\rho} \mathbf{v}) \tag{2.2}$$

where respectively ρ and $\mathbf{w}$ are the plasma density and velocity field, and $\hat{\rho}$ and $\mathbf{v}$ are the neutral gas density and velocity field.

- Momentum Equations:

$$\rho\dot{\mathbf{w}} + \rho(\mathbf{w}\cdot\nabla)\mathbf{w} = -\nabla p + \mathbf{J}\times\mathbf{B} + \mathbf{\Gamma}_c \tag{2.3}$$

$$\hat{\rho}\dot{\mathbf{v}} + \hat{\rho}(\mathbf{v}\cdot\nabla)\mathbf{v} = -\nabla\hat{p} - \mathbf{\Gamma}_c \tag{2.4}$$

where $\mathbf{J}$ is the current density and $\mathbf{B}$ is the magnetic flux density. The plasma pressure is p and the neutral gas pressure denoted by $\hat{p}$. The coupling term is

$$\mathbf{\Gamma}_c = \frac{\rho}{\tau}|\mathbf{w}-\mathbf{v}| \tag{2.5}$$

see sections 1.4.3 and 1.4.4 for the background for this.

- Other equations: To complete the initial set of equations, the magnetic field equation is required, and each fluid has an adiabatic equation of state:

$$\dot{\mathbf{B}} = \nabla\times(\mathbf{w}\times\mathbf{B}) \tag{2.6}$$

$$p \propto \rho^{\gamma_a} \tag{2.7}$$

$$\hat{p} \propto \hat{\rho}^{\gamma_a} \tag{2.8}$$

The adiabatic constant $\gamma_a = 5/3$ governs the equations of state. The usual dot notation denotes a time derivative.

The following assumptions will be made: first, the perturbed wave modes will have small amplitude and low frequency, so that it is reasonable to work in the linear regime[4]. Furthermore, in this two-dimensional case the waves are confined to the x-z regime. Finally, assume that the equilibrium is homogeneous, and that an equilibrium, or "background", magnetic flux density $\mathbf{B}_0$ is uniform and aligned along the positive z-direction.

[4]Note that this is a computational decision; the Alfvén wave equations are inherently non-linear but can be solved using the linear equations.

2.2.1 Step 1: Linearise the Equations

To linearise the equations the following substitutions are made: using the terminology of Diver et al. (2006), each term is replaced by two components: a zeroth order (or equilibrium) term with the subscript 0, and a first order (or perturbation) term with subscript 1.

$$\rho \mapsto \rho_0 + \rho_1$$

$$\mathbf{w} \mapsto \mathbf{w}_0 + \mathbf{w}_1$$

$$p \mapsto p_0 + p_1$$

$$\hat{\rho} \mapsto \hat{\rho}_0 + \hat{\rho}_1$$

$$\mathbf{v} \mapsto \mathbf{v}_0 + \mathbf{v}_1$$

$$\hat{p} \mapsto \hat{p}_0 + \hat{p}_1$$

$$\mathbf{J} \mapsto \mathbf{J}_0 + \mathbf{J}_1$$

$$\mathbf{B} \mapsto \mathbf{B}_0 + \mathbf{B}_1$$

Equations 2.1-2.8 can be linearised by making these substitutions and then dropping terms that are greater than first order. First, however, it is instructive to examine the assumptions made about the equilibrium conditions.

2.2.2 Step 2: Substitute Equilibrium Conditions

The equilibrium assumptions made can be substituted into the set of equations as shown below.

1. The assumption of a spatially-homogeneous equilibrium density means that $\dot{\rho}_0 = \dot{\hat{\rho}}_0 = 0$ and $\nabla\rho_0 = \nabla\hat{\rho}_0 = 0$.

2. It is reasonable to assume that there are initially no flows in the velocity fields, i.e. $\mathbf{w}_0 = \mathbf{v}_0 = 0$.

3. The homogeneous equilibrium magnetic flux density is uniform in the z-direction and zero elsewhere, i.e. $\mathbf{B}_0 = B_0\hat{\mathbf{z}}$.

4. The adiabatic equations of state mean that the pressure terms can be written in terms of density and sound speed by combining the model equations. For the plasma this is $\nabla p = \sigma^2 \nabla \rho$ and the neutral gas relation is $\nabla \hat{p} = c^2 \nabla \hat{\rho}$.

5. Ideal MHD relates the current density and the magnetic flux density as follows: $\mu_0 \mathbf{J} = \nabla \times \mathbf{B}$ where μ_0 is the permeability of free space.

Now the linearised equations with the equilibrium assumptions applied look like this:

$$\dot{\rho}_1 = -\rho_0 \nabla \cdot \mathbf{w}_1 \tag{2.9}$$

$$\rho_0 \mathbf{w}_1 = -\sigma^2 \nabla \rho_1 + (\nabla \times \mathbf{B}_1) \times \mathbf{B}_0 + \frac{\rho_0}{\tau} |\mathbf{w}_1 - \mathbf{v}_1| \tag{2.10}$$

$$\dot{\mathbf{B}}_1 = \nabla \times (\mathbf{w}_1 \times \mathbf{B}_0) \tag{2.11}$$

$$\dot{\hat{\rho}}_1 = -\hat{\rho}_0 \nabla \cdot \mathbf{v}_1 \tag{2.12}$$

$$\hat{\rho}_0 \mathbf{v}_1 = -c^2 \nabla \hat{\rho}_1 - \frac{\rho_0}{\tau} |\mathbf{w}_1 - \mathbf{v}_1| \tag{2.13}$$

2.2.3 The 2D Linearised Equations

Finally, substituting the velocity and magnetic flux density vectors e.g. $\mathbf{w}_1 = w_x \hat{\mathbf{x}} + w_z \hat{\mathbf{z}}$ simplifies the cross product and curl terms. The coupling term $\mathbf{\Gamma}_c$ has been replaced by the vector $\mathbf{K} = (K_x, K_z)$ described below. The result is a set of five linear equations for the plasma:

$$\dot{\rho}_1 = -\rho_0 (\partial_x w_x + \partial_z w_z) \tag{2.14}$$

$$\rho_0 \dot{w}_x = -\sigma^2 \partial_x \rho + \frac{B_0}{\mu_0} (\partial_z B_x - \partial_x B_z) + K_x \tag{2.15}$$

$$\rho_0 \dot{w}_z = -\sigma^2 \partial_z \rho + K_z \tag{2.16}$$

$$\dot{B}_x = B_0 \partial_z w_x \tag{2.17}$$

$$\dot{B}_z = -B_0 \partial_x w_x \tag{2.18}$$

and three equations for the neutral gas complete the system:

$$\dot{\hat{\rho}} = -\hat{\rho}_0 (\partial_x v_x + \partial_z v_z) \tag{2.19}$$

$$\hat{\rho}_0 \dot{v}_x = -c^2 \partial_x \hat{\rho} - K_x \tag{2.20}$$

$$\hat{\rho}_0 \dot{v}_z = -c^2 \partial_z \hat{\rho} - K_z \tag{2.21}$$

The notation ∂_x denotes the partial derivative $\partial/\partial x$, and so on. The momentum coupling terms K_x and K_z are part of the plasma and neutral gas momentum equations in such a way that the total fluid (that is, plasma plus neutral gas) momentum is conserved. The form of the vector momentum coupling term $\mathbf{K} = (K_x, K_z)$ is

$$K_{x,z} = \pm \frac{\rho_0}{\tau} |w_{x,z} - v_{x,z}| \tag{2.22}$$

Notice that in the linearised equations, the coefficient ρ_0/τ includes the equilibrium density ρ_0. This means that ρ_0/τ can be taken as a constant of proportionality; that is, the momentum coupling is similar to a drag or friction term that operates when the two fluids have a relative velocity. Since both fluids are adiabatic gases, kinetic energy transferred via this momentum coupling is the only available method of energy transfer between them[5].

2.2.4 Non-dimensionalising the Equations

In order to computationally solve the system, the equations must be non-dimensionalised. In other words, each term was substituted with a dimensionless scale factor, normalised by some characteristic physical quantity. For example, the plasma density was written as $e = \rho_1/\rho_0$ where, as above, ρ_1 is the density perturbation term and ρ_0 is the equilibrium density. The non-dimensionalisation for all terms was as follows:

$$d = \frac{\hat{\rho}_1}{\hat{\rho}_0} \tag{2.23}$$

$$e = \frac{\rho_1}{\rho_0} \tag{2.24}$$

$$p = \frac{w_x}{\alpha} \tag{2.25}$$

[5]This is true because although the first moment equation of the distribution function is modified by the momentum coupling term, the second moment is not adjusted, meaning that an adiabatic equation of state still holds for each fluid.

$$q = \frac{w_z}{\alpha} \tag{2.26}$$

$$g = \frac{v_x}{\alpha} \tag{2.27}$$

$$h = \frac{v_z}{\alpha} \tag{2.28}$$

$$m = \frac{B_x}{B_0} \tag{2.29}$$

$$n = \frac{B_z}{B_0} \tag{2.30}$$

The density terms are normalised to the equilibrium densities ρ and $\hat{\rho}$, the velocity terms are normalised to the Alfvén speed of the plasma α, and the magnetic flux density terms are normalised to the equilibrium background magnetic field B_0.

The basic units of distance and time also need to be written in dimensionless form, using the characteristic length (L) and time (T) of the physical system. The dimensionless factors substituted were:

$$\tau = \frac{t}{T} \tag{2.31}$$

$$\xi = \frac{x}{L} \tag{2.32}$$

$$\zeta = \frac{z}{L} \tag{2.33}$$

$$\alpha = \frac{L}{T} = \frac{B_0}{\sqrt{\rho_0 \mu_0}} \tag{2.34}$$

where t, x and z are the basic units of time and distance in the dimensional equations, and to tie it all together α is chosen to be the characteristic velocity of the physical system (recall that it was already used to non-dimensionalise the other velocity terms). When these co-ordinate changes are substituted the derivative terms are also altered as follows:

$$\partial_x \mapsto \frac{1}{L}\partial_\xi$$
$$\partial_z \mapsto \frac{1}{L}\partial_\zeta$$
$$\partial_t \mapsto \frac{1}{T}\partial_\tau$$

After making all of these substitutions and simplifying, the dimensionless code

equations are:

$$d_\tau = -(g_\xi + h_\zeta) \tag{2.35}$$

$$e_\tau = -(p_\xi + q_\zeta) \tag{2.36}$$

$$p_\tau = -r^2 e_\xi + (m_\zeta - n_\xi) - \Gamma|p - g| \tag{2.37}$$

$$q_\tau = -r^2 e_\zeta - \Gamma|q - h| \tag{2.38}$$

$$g_\tau = -s^2 d_\xi + \frac{\Gamma}{\kappa}|p - g| \tag{2.39}$$

$$h_\tau = -s^2 d_\zeta + \frac{\Gamma}{\kappa}|q - h| \tag{2.40}$$

$$m_\tau = p_\zeta \tag{2.41}$$

$$n_\tau = -q_\xi \tag{2.42}$$

where the subscripts indicate a derivative in that direction, and the momentum coupling coefficient defined in equation 2.22 have been replaced with the normalised dimensionless coupling term $\Gamma = T/\tau$. Notice that the density ρ_0 no longer appears in the coupling term, meaning that it can be treated as a constant parameter. A value of $\Gamma = 0.1$ was chosen initially. The constant $\kappa = \hat{\rho}_0/\rho_0$ is the ratio of background neutral gas density to background plasma density.

This system of eight equations has eight variables and two control parameters. The parameters are the normalised sound speeds: $r = \sigma/\alpha$ for the plasma and $s = c/\alpha$ for the neutral gas, where α is the Alfvén speed in the plasma. By altering r and s, the relative populations of plasma and neutral gas in the simulation can be controlled; for example, in a simulation where $r = s = 1$, equal densities of plasma and neutral gas are present, and the sound speeds are both equal to the Alfvén speed. Numerically solving the system of equations 2.35- 2.42 in this way for a 2-dimensional grid yields full results for each of the eight variables; the density and the 2-D velocity space for both the plasma and the neutral gas components of the mixture, as well as the 2-D magnetic flux density.

2.3 Lax-Wendroff Method and the Computational Solutions

Lax-Wendroff (Mitchell and Griffiths 1980) is a numerical method based on finite differences, accurate to second order, which can find approximate numerical solutions to hyperbolic partial differential equations. Given the initial conditions for a system of equations at time $t = 0$, the method solves the model equations numerically for the next timestep. These solutions become the new starting conditions, and the method is repeated, and so on, until the equations have been solved at every timestep in the desired range. Lax-Wendroff is an explicit method, meaning that there are characteristic length and time steps (which can also be thought of as a maximum signal propagation speed) that control the numerical stability of the solutions.

2.3.1 Deriving the Lax-Wendroff Method

The derivation of the Lax-Wendroff method begins with the linear advection equation, e.g. in one dimension:

$$\frac{\partial}{\partial t}u(x,t) + A\frac{\partial}{\partial x}u(x,t) = 0 \tag{2.43}$$

where A a constant speed (the 'advection speed'). u is some well-behaved scalar function of space and time. The variables x and t and function u can be discretised into steps like so:

$$u_i^n = u(x_i, t^n) \tag{2.44}$$

Taylor expand equation 2.44 to second order in the usual fashion to find

$$u_i^{n+1} = u_i^n + \Delta t\frac{\partial}{\partial t}u_i^n + \frac{A^2\Delta t^2}{2}\frac{\partial^2}{\partial t^2}u_i^n \tag{2.45}$$

where higher order terms are neglected. Now substitute the time derivatives for spatial derivatives according to equation 2.43

$$u_i^{n+1} = u_i^n - A\Delta t\frac{\partial}{\partial x}u_i^n + \frac{A^2\Delta t^2}{2}\frac{\partial^2}{\partial x^2}u_i^n \tag{2.46}$$

Next, replace the spatial derivatives using the central finite difference formula

$$\frac{\partial}{\partial x}u_i^n = \frac{u_{i+1/2}^n - u_{i-1/2}^n}{\Delta x} \tag{2.47}$$

$$\approx \frac{u_{i+1}^n - u_{i-1}^n}{2\Delta x} \tag{2.48}$$

$$\frac{\partial^2}{\partial x^2}u_i^n = \frac{u_{i+1}^n - 2u_i^n + u_{i-1}^n}{\Delta x} \tag{2.49}$$

which results in

$$u_i^{n+1} = u_i^n - \frac{A\Delta t}{2\Delta x}(u_{i+1}^n - u_{i-1}^n) + \frac{A^2\Delta t^2}{2\Delta x^2}(u_{i+1}^n - 2u_i^n + u_{i-1}^n) \tag{2.50}$$

$$= (1-\mu^2A^2)u_i^n - \frac{1}{2}\mu A(1-\mu A)u_{i+1}^n + \frac{1}{2}\mu A(1+\mu A)u_{i-1}^n \tag{2.51}$$

where $\mu = \Delta t/\Delta x$ is the mesh ratio. Stability limits on μ will be discussed in section 2.3.2. Given the starting conditions u_i^0 for all i, the method finds the next step u_i^1 (for all i). Then repeat to find the following step, and so on, until all timesteps are calculated. The method is accurate to second order.

2.3.2 Extension to Two Dimensions

Extending the solution by starting with a two-dimensional advection equation, the derivation starts with a hyperbolic equation with two spatial derivatives:

$$\frac{\partial}{\partial t}\mathbf{u}(x,z,t) + A\frac{\partial}{\partial x}\mathbf{u}(x,z,t) + B\frac{\partial}{\partial z}\mathbf{u}(x,z,t) = 0 \tag{2.52}$$

where now $\mathbf{u}$ is a vector of functions that are to be solved. In this way the Lax-Wendroff method can be applied to solve systems of equations. Then A and B are constant matrices of coefficients which link the different equations in the system[6]. The system studied here has eight equations (equations 2.35 - 2.42) so $\mathbf{u}$ is a vector with eight

[6]In general, A and B could be functions of position. This would change the derivation slightly.

entries;

$$\mathbf{u} = \begin{bmatrix} d \\ e \\ g \\ h \\ m \\ n \\ p \\ q \end{bmatrix} \tag{2.53}$$

while A and B are a pair of 8×8 matrices:

$$A = \begin{bmatrix} 0 & 0 & 1 & 0 & 0 & 0 & 0 & 0 \\ 0 & 0 & 0 & 0 & 0 & 0 & 1 & 0 \\ s^2 & 0 & 0 & 0 & 0 & 0 & 0 & 0 \\ 0 & 0 & 0 & 0 & 0 & 0 & 0 & 0 \\ 0 & 0 & 0 & 0 & 0 & 0 & 0 & 0 \\ 0 & 0 & 0 & 0 & 0 & 0 & 1 & 0 \\ 0 & r^2 & 0 & 0 & 0 & 1 & 0 & 0 \\ 0 & 0 & 0 & 0 & 0 & 0 & 0 & 0 \end{bmatrix} \tag{2.54}$$

and

$$B = \begin{bmatrix} 0 & 0 & 0 & 1 & 0 & 0 & 0 & 0 \\ 0 & 0 & 0 & 0 & 0 & 0 & 0 & 1 \\ 0 & 0 & 0 & 0 & 0 & 0 & 0 & 0 \\ s^2 & 0 & 0 & 0 & 0 & 0 & 0 & 0 \\ 0 & 0 & 0 & 0 & 0 & 0 & -1 & 0 \\ 0 & 0 & 0 & 0 & 0 & 0 & 0 & 0 \\ 0 & 0 & 0 & 0 & -1 & 0 & 0 & 0 \\ 0 & r^2 & 0 & 0 & 0 & 0 & 0 & 0 \end{bmatrix} \tag{2.55}$$

As in the 1-D case, the first step in the derivation is to write out the Taylor expansion

in time of the vector **u**:

$$\mathbf{u}_{i,j}^{n+1} = \mathbf{u}_{i,j}^{n} + \Delta t \frac{\partial}{\partial t}\mathbf{u}_{i,j}^{n} + \frac{A^2\Delta t^2}{2}\frac{\partial^2}{\partial t^2}\mathbf{u}_{i,j}^{n} \tag{2.56}$$

where the only difference between equation 2.56 and equation 2.45 is that eq. 2.56 is in two spatial dimensions x and z, hence the two spatial subscripts i and j. Now substitute the time derivatives by rearranging equation 2.52 to find the operators

$$\frac{\partial}{\partial t} = -A\frac{\partial}{\partial x} - B\frac{\partial}{\partial z} \tag{2.57}$$

$$\frac{\partial^2}{\partial t^2} = A^2\frac{\partial^2}{\partial x^2} + B^2\frac{\partial^2}{\partial z^2} + (AB + BA)\frac{\partial}{\partial x}\frac{\partial}{\partial z} \tag{2.58}$$

Next, as before, substitute the spatial derivative operators for the central difference approximation.

$$\frac{\partial}{\partial x}\mathbf{u}_{i,j}^{n} \approx \frac{1}{h}\left(\mathbf{u}_{i+1/2,j}^{n} - \mathbf{u}_{i-1/2,j}^{n}\right) \tag{2.59}$$

$$\approx \frac{1}{2h}\left(\mathbf{u}_{i+1,j}^{n} - \mathbf{u}_{i-1,j}^{n}\right) \tag{2.60}$$

$$\frac{\partial^2}{\partial x^2}\mathbf{u}_{i,j}^{n} = \frac{1}{h^2}\left(\mathbf{u}_{i+1,j}^{n} - 2\mathbf{u}_{i,j}^{n} + \mathbf{u}_{i-1,j}^{n}\right) \tag{2.61}$$

$$\frac{\partial}{\partial z}\mathbf{u}_{i,j}^{n} \approx \frac{1}{h}\left(\mathbf{u}_{i,j+1/2}^{n} - \mathbf{u}_{i,j-1/2}^{n}\right) \tag{2.62}$$

$$\approx \frac{1}{2h}\left(\mathbf{u}_{i,j+1}^{n} - \mathbf{u}_{i,j-1}^{n}\right) \tag{2.63}$$

$$\frac{\partial^2}{\partial z^2}\mathbf{u}_{i,j}^{n} = \frac{1}{h^2}\left(\mathbf{u}_{i,j+1}^{n} - 2\mathbf{u}_{i,j}^{n} + \mathbf{u}_{i,j-1}^{n}\right) \tag{2.64}$$

where in this case h is the step size in both directions x and z. Now the expression for the $(n+1)$th timestep for each function in the vector **u**, given the nth step is:

$$\mathbf{u}_{i,j}^{n+1} = \left[I - \frac{1}{2}\mu A H_x - \frac{1}{2}\mu B H_z + \frac{1}{2}\mu^2 A^2\delta_x^2 + \frac{1}{2}\mu^2 B^2\delta_z^2 + \frac{1}{8}\mu^2(AB + BA)H_x H_z\right]\mathbf{u}_{i,j}^{n} \tag{2.65}$$

with operators defined as

$$\delta_x^2\mathbf{u}_{i,j}^{n} = \mathbf{u}_{i+1,j}^{n} - 2\mathbf{u}_{i,j}^{n} + \mathbf{u}_{i-1,j}^{n} \tag{2.66}$$

$$\delta_z^2\mathbf{u}_{i,j}^{n} = \mathbf{u}_{i,j+1}^{n} - 2\mathbf{u}_{i,j}^{n} + \mathbf{u}_{i,j-1}^{n} \tag{2.67}$$

$$H_x \mathbf{u}_{i,j}^n = \mathbf{u}_{i+1,j}^n - \mathbf{u}_{i-1,j}^n \tag{2.68}$$

$$H_z \mathbf{u}_{i,j}^n = \mathbf{u}_{i,j+1}^n - \mathbf{u}_{i,j-1}^n \tag{2.69}$$

and where $\mu = \frac{\Delta t}{h}$ is the mesh ratio, and I is obviously an 8×8 identity matrix. Now the algorithm for the Lax-Wendroff method in two dimensions can be completed by calculating AB, BA, A^2 and B^2 by multiplying the matrices to obtain:

$$A^2 = \begin{bmatrix} s^2 & 0 & 0 & 0 & 0 & 0 & 0 & 0 \\ 0 & r^2 & 0 & 0 & 0 & 1 & 0 & 0 \\ 0 & 0 & s^2 & 0 & 0 & 0 & 0 & 0 \\ 0 & 0 & 0 & 0 & 0 & 0 & 0 & 0 \\ 0 & 0 & 0 & 0 & 0 & 0 & 0 & 0 \\ 0 & r^2 & 0 & 0 & 0 & 1 & 0 & 0 \\ 0 & 0 & 0 & 0 & 0 & 0 & r^2+1 & 0 \\ 0 & 0 & 0 & 0 & 0 & 0 & 0 & 0 \end{bmatrix} \tag{2.70}$$

$$B^2 = \begin{bmatrix} s^2 & 0 & 0 & 0 & 0 & 0 & 0 & 0 \\ 0 & r^2 & 0 & 0 & 0 & 0 & 0 & 0 \\ 0 & 0 & 0 & 0 & 0 & 0 & 0 & 0 \\ 0 & 0 & 0 & s^2 & 0 & 0 & 0 & 0 \\ 0 & 0 & 0 & 0 & 1 & 0 & 0 & 0 \\ 0 & 0 & 0 & 0 & 0 & 0 & 0 & 0 \\ 0 & 0 & 0 & 0 & 0 & 0 & 1 & 0 \\ 0 & 0 & 0 & 0 & 0 & 0 & 0 & r^2 \end{bmatrix} \tag{2.71}$$

$$AB + BA = \begin{bmatrix} 0 & 0 & 0 & 0 & 0 & 0 & 0 & 0 \\ 0 & 0 & 0 & 0 & -1 & 0 & 0 & 0 \\ 0 & 0 & 0 & s^2 & 0 & 0 & 0 & 0 \\ 0 & 0 & s^2 & 0 & 0 & 0 & 0 & 0 \\ 0 & -r^2 & 0 & 0 & 0 & -1 & 0 & 0 \\ 0 & 0 & 0 & 0 & -1 & 0 & 0 & 0 \\ 0 & 0 & 0 & 0 & 0 & 0 & 0 & r^2 \\ 0 & 0 & 0 & 0 & 0 & 0 & r^2 & 0 \end{bmatrix} \tag{2.72}$$

Now, for example, the equation for the neutral gas density d can be written out:

$$d_{i,j}^{n+1} = d_{i,j}^{n} - \frac{1}{2}\mu H_x g_{i,j,}^{n} - \frac{1}{2}H_y h_{i,j}^{n} + \frac{1}{2}\mu^2 s^2 \delta_x^2 d_{i,j}^{n} + \frac{1}{2}\mu^2 s^2 \delta_y^2 d_{i,j}^{n} \tag{2.73}$$

Similarly, the equations for the other eight variables are contained within the matrices. Thus the eight Lax-Wendroff algorithm equations are now in a form amenable to computation.

Stability criteria of the Lax-Wendroff method

It can be shown (Mitchell and Griffiths 1980) that the stability criteria of a Lax-Wendroff solution to a two-dimensional hyperbolic system, where A and B are constant matrices, is as follows:

$$\mu|\lambda_m| \leq \frac{1}{2\sqrt{2}} \tag{2.74}$$

λ_m is a scalar given by the formula

$$|\lambda_m| = \max_{A,B}\left[|\lambda_A|, |\lambda_B|\right] \tag{2.75}$$

where

$$|A - \lambda_A I| = 0 \tag{2.76}$$

$$|B - \lambda_B I| = 0 \tag{2.77}$$

Note that this limit is more strict than the Courant-Friedrichs-Lewy (CFL) limit, which is $\mu|\lambda_m| \leq 1$. To satisfy the stability condition, a mesh ratio of $\mu = 0.25$ was chosen for the code.

2.3.3 The Computational Domain

A computational routine using the Lax-Wendroff algorithm was written and implemented using FORTRAN-77. The spatial computational domain was $i_{\mathbf{max}}$ steps in the x direction and $j_{\mathbf{max}}$ steps in the z direction, with $j_{\mathbf{max}} > i_{\mathbf{max}}$. Along one short side of the grid, the "driving wall" was the row of grid points that was consistently perturbed to launch waves into the computational domain. With eight quantities governed by the eight coupled equations, almost any wave mode supported by the plasma or the neutral gas could be launched with the appropriate choice of driver. The code was written in such a way that the background magnetic field in the system uniformly pointed in the z-direction, i.e. along the long direction of the grid.

Boundary Conditions

On all boundaries apart from the driving wall, boundary conditions were transparent so that there were no reflections. "Dummy" points were set on the grid outside the computed points, extrapolated from the points immediately adjacent to the edge of the grid. These dummy points were updated every timestep before the numerical solver calculated the next step for each of the points in the domain. This allowed accuracy to be preserved by ensuring that the full second-order algorithm could be applied right up to the edges of the computational domain. As an additional benefit the extrapolated points outside the domain meant that any perturbation encountering the boundary of the computational domain would simply pass across it and leave the system. Therefore the dummy points ensured the desired transparency for the boundaries.

For example, along one 'long' side of the domain points (i.e. the line $i = 1$) a set of dummy points $i = 0$ was defined and calculated, and for the other long side the points

$i = i_{max} + 1$ were defined. Finally, the short side of the domain that wasn't the driving wall had its own set of dummy points $j = j_{max} + 1$ calculated. Each dummy point was extrapolated from three points along a straight line perpendicular to the domain boundary: the corresponding point on the edge of the computational domain plus the adjacent and next-adjacent points into the domain. Equations 2.78, 2.79 and 2.80 below show the quadratic extrapolation formulae used to define the dummy points for the example of plasma density[7]:

$$e^n_{0,j} = e^n_{3,j} - 3e^n_{2,j} + 3e^n_{1,j} \quad , \forall\, j \tag{2.78}$$

$$e^n_{i_{max}+1,j} = e^n_{i_{max}-2,j} - 3e^n_{i_{max}-1,j} + 3e^n_{i_{max},j} \quad , \forall\, j \tag{2.79}$$

$$e^n_{i,j_{max}} = e^n_{i,j_{max}-2} - 3e^n_{i,j_{max}-1} + 3e^n_{i,j_{max}} \quad , \forall\, i \tag{2.80}$$

The driving wall consisted of the points described by $e^n_{i,0} \quad , \forall\, i$.

Driving Perturbation

The driving wall was perturbed by a function primarily of cosine form, with additional variations and spatial structure that altered depending on which wave modes it is desired to induce. These perturbations propagate via the model equations as wave modes allowed by the plasma-neutral mixture spread into the domain. The driving perturbation was of the form

$$\textbf{driver} \propto \cos \omega t \, (1 + \cos kx) \tag{2.81}$$

This form for the driver provides uniform perturbations along the driving wall, within a spatial envelope shaped in cosine form, as shown in figure 2.2 in comparison with a plane wave driving envelope. A plane wave driver[8] is instructive in some situations, but it is a very idealised condition. In reality it is likely that some of the most interesting effects would take place "at the edges", i.e. near parts of the wave front where the

[7] Note that the mesh ratio does not appear in these equations because the system is dimensionless, therefore the dummy points are automatically scaled to the computational grid.

[8] In this context "plane wave" means the case where every point on the wave front has a wave vector with a non-zero component only in the direction of travel of the wave.

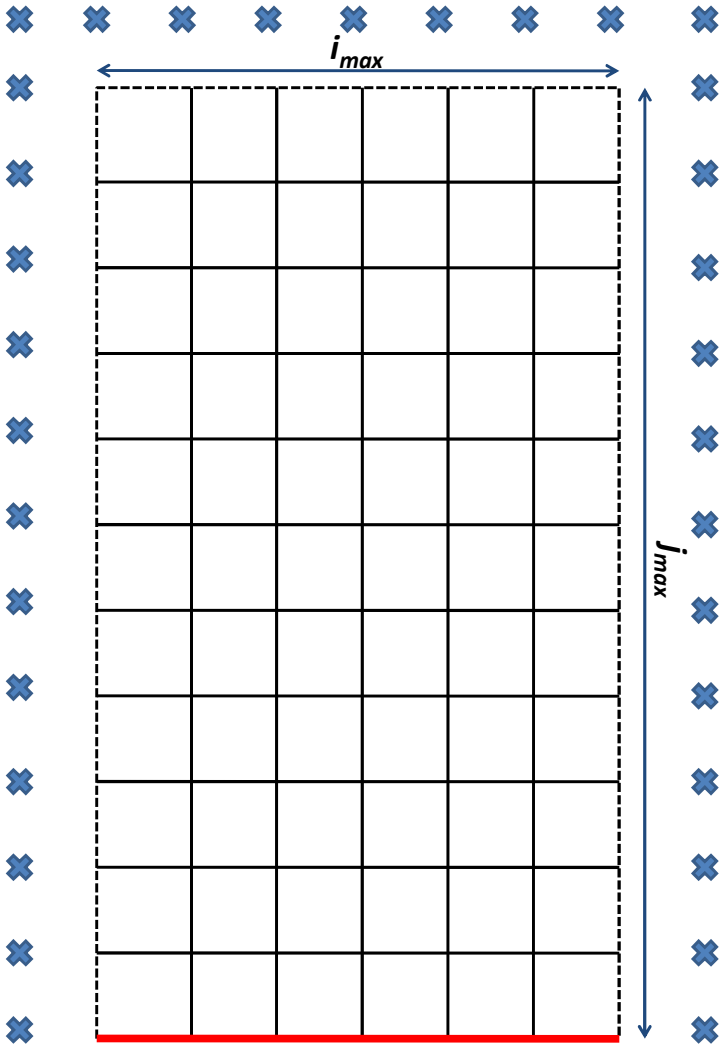

Figure 2.1: Schematic of the computational grid, with the driving wall shown in red. The dummy points outside the edges of the computational domain are marked by the blue crosses.

wave vector has non-zero components in more than one direction. The spatial part of the perturbation form can be used to study just such a situation: by spatially limiting the extent of the driven wave front, a more realistic *superposition* of wave modes is induced, and it is crucial to understand the interplay between these modes in order to gain insight into the wider problems which will be discussed later.

The transverse Alfvén mode is non-dispersive[9], therefore a full frequency spectrum

[9]The transverse Alfvén mode has dispersion relation $\omega = kc_A$ with frequency ω, wavenumber k and

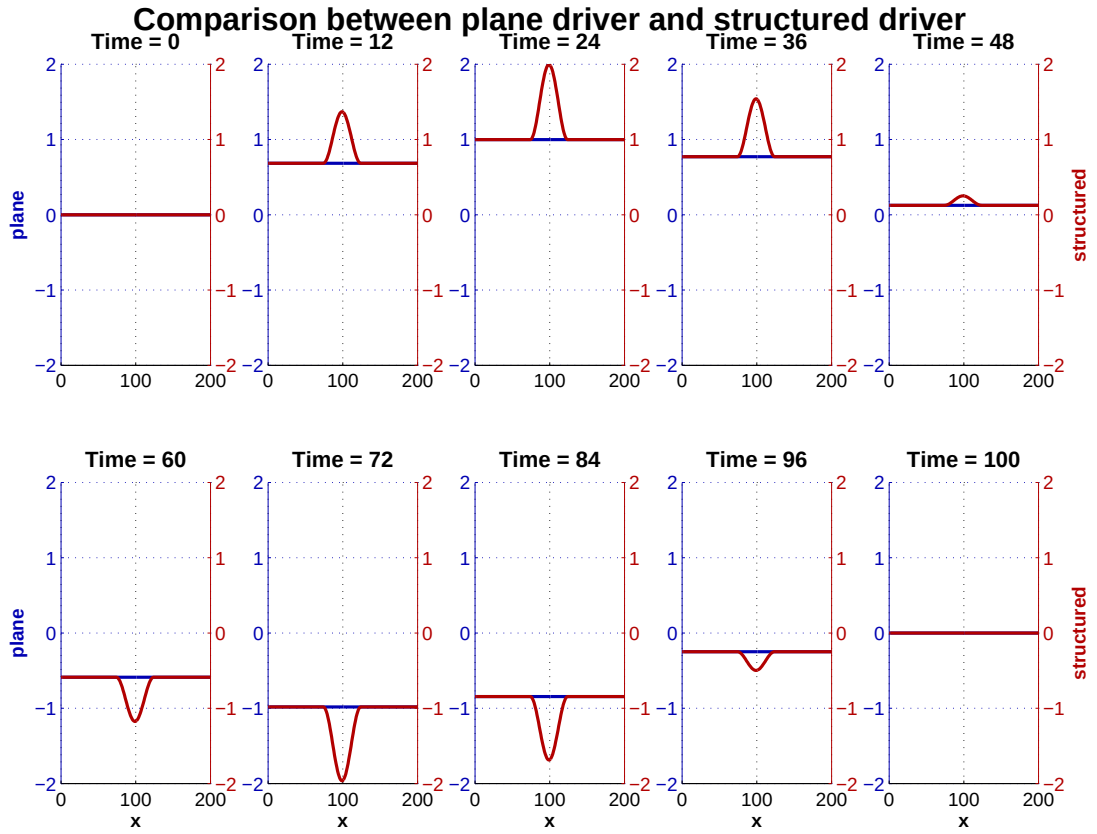

Figure 2.2: This plot shows snapshots of the driving perturbation changing with time, over one full cycle. The blue line shows, for comparison, a driver that would induce idealised plane waves. The red line shows the driver used in these simulations, which adds a spatial structure to the planar driving perturbation. The additional structure is confined to the middle of the driving wall between $x = 75$ and $x = 125$, and has the spatial form of half a cosine (a value of $\cos(2\pi x/100)$ between $x = 75$ and $x = 125$ was added to the otherwise flat spatial form of the driving perturbation).

is available for study. In other words, any choice of driving frequency within limits would excite the transverse Alfvén mode. The frequency was chosen to be more than high enough for the computational timestep to resolve the waves properly, but not so high that the total computational time became prohibitive.

speed c_A, the Alfvén speed

2.3.4 Convergence of the Code

In addition to the stability requirements and the correct boundary conditions, it is important to check that the code is physically correct. One way to verify this is to compare the results from two simulations with identical initial conditions, but with different mesh ratios. A code with double the mesh ratio, but evolved for half the number of timesteps, should produce identical results. Figures 2.3 and 2.4 show the results of two such simulations for comparison. Any differences between the figures are due to the plotting.

2.4 The Combined Response of the Plasma-Neutral Mixture

Using the methods derived above and the FORTRAN-77 code that was written to numerically solve the algorithms, simulations could be run to investigate the effects of exciting different wave modes in partially-ionised plasmas of varying composition. The code used in this thesis was originally written as part of the work reported in Diver et al. (2006), but was modified in several ways:

1. Diver et al. (2006) was concerned with sonic/magnetosonic excitation; this thesis will primarily focus on transverse Alfvén waves as the driver.

2. The driving perturbation is provided here by one wall of the computational domain; Diver et al. (2006) presented results from a 2-D Gaussian driver positioned in the centre of the domain.

3. To allow extension of the model into further parameter space, and eventually to inhomogeneous or recombining plasmas, the third characteristic speed i.e. the plasma Alfvén speed was made modifiable, in addition to the two sound speeds.

The simulation results confirm the importance of the *interaction* between what can be considered as the two co-spatial populations. The *combined response* of the plasma

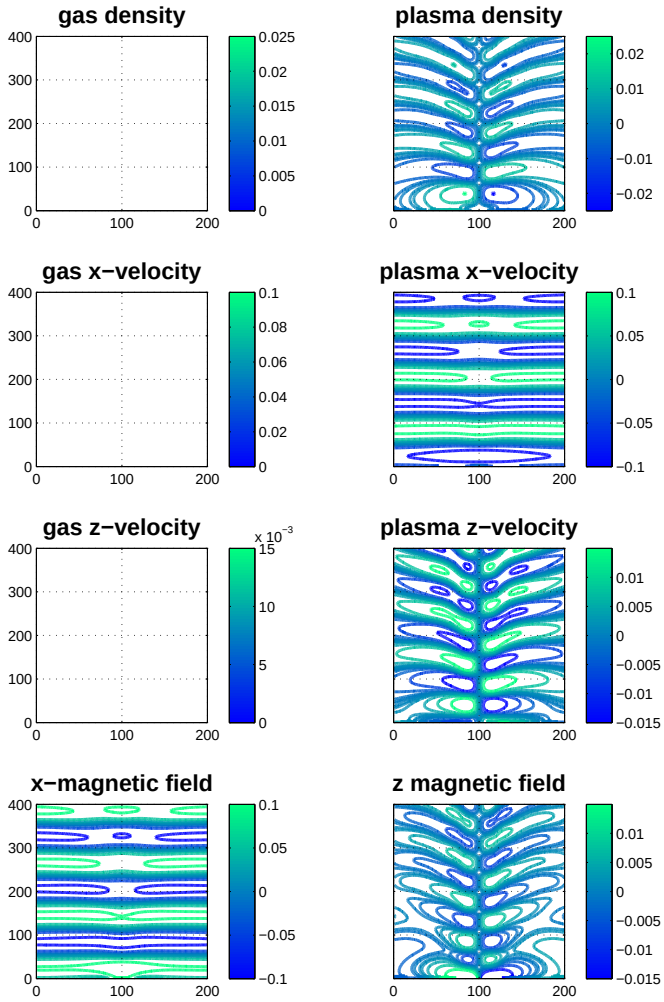

Figure 2.3: Calibration test 1: A standard example of simulation results of the form presented in figures 2.16- 2.19. Here it is shown as an example perturbations caused by a transverse Alfvén wave driven in an uncoupled plasma, where the sound speed equals the Alfvén speed ($r = u = 1$). In this simulation the mesh ratio was $\mu = 0.25$ and the number of timesteps evolved was $nt = 3000$, with the figure showing a snapshot of the final timestep for the eight quantities. Note that the neutral gas plots are empty because this example is for an uncoupled plasma, i.e. there is no neutral gas present.

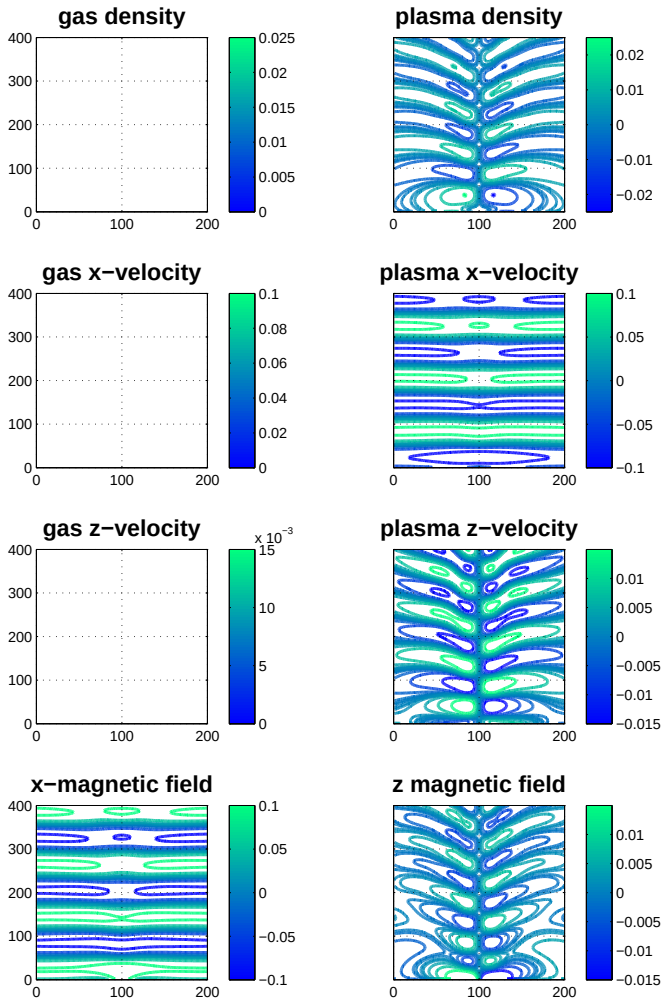

Figure 2.4: Calibration test 2: For comparison to figure 2.3, this figure shows the results of a simulation with identical initial conditions but different mesh and timestep parameters. In this simulation the mesh ratio was $\mu = 0.5$ (N.B. still within the stability limit discussed in section 2.3.2) and the number of timesteps evolved was $nt = 1500$, with the figure showing a snapshot of the final timestep for all eight quantities. Note that the neutral gas plots are empty because this example is for an uncoupled plasma, i.e. there is no neutral gas present.

population with the neutral gas population becomes dominant over any individual response. To clearly illustrate this, two examples are particularly informative:

1. An Alfvén wave excited in the plasma - showing that even purely magnetic waves can indirectly influence the neutral gas in a coherent way.

2. A sound wave excited in the neutral gas, which demonstrates that, conversely, purely neutral hydrodynamic waves can indirectly cause coherent magnetic perturbations.

This unusual connection between magnetic effects and neutral fluid is crucial to understanding the propagation of waves, and is particularly important when it comes to diagnostic techniques based on said magnetic effects. This section will examine the two examples in detail, leading to a discussion of constructive improvements to the Chandrasekhar-Fermi diagnostic method in the next chapter.

Physically, the complexity of the combined response is twofold; the most apparent difficulty arises from the fact that the momentum coupling between the plasma and neutral gas populations means that any excitation to one fluid produces a response in both fluids. In this way for example, an initial transverse Alfvén wave in the plasma can indirectly induce sound waves in the gas. Such sound waves carry energy away from the central wave isotropically and even out of the system if they cross the transparent boundaries of the computational grid.

However, this mode conversion is only half of the story; as described above, in a more realistic case there would be a superposition of wave modes driven in the plasma in the first place, and the combined response to this superposition is the dominant factor. This was taken into account by adding spatial structure to the simulation driver in the transverse direction, to incorporate features associated with a spatially-limited Alfvén wave. In other words, the simulations were carried out with the assumption that the coherence scale of the perturbations was smaller than the size of the overall domain: a reasonable assumption given the physical scale lengths involved. Now the additional pressure term implicated near the edges of the pencil of Alfvén waves drives

sonic and magnetosonic wave modes as well, and these couple with the neutral gas to cause further feedback of sonic wave modes between the two populations.

2.4.1 Interpreting the Data

With multiple wave modes and eight variables to analyse, there is a lot of detail to consider in the data. Features common to all figures are listed here for reference.

1. In all figures showing the computational domain, the x-axis is horizontal and the z-axis is vertical. The background magnetic field B_0 is uniform and aligned along the z-direction.

2. "Transverse mode characteristics" are perturbations to the plasma x-velocity and x-magnetic field in the x-direction only (i.e. in the direction parallel to the background magnetic field). All transverse Alfvén waves have these features (according to the dispersion relation, equation 1.72), but not all of these features are related to transverse Alfvén waves.

3. A plane transverse Alfvén wave would propagate through the computational domain perturbing *only* the plasma x-velocity and x-magnetic field in a planar fashion i.e. the contour plots would simply show a series of horizontal lines in these two quantities, with no other quantity perturbed.

4. "Non-transverse characteristics" are any perturbations which are *not* associated with the transverse Alfvén mode, i.e. sonic and magnetosonic perturbations. This includes *all* perturbations to the neutral gas velocity field, the plasma z-velocity and z-magnetic field. Obviously all perturbations to the density field of either fluid are also non-transverse.

5. The driving perturbation excites the plasma x-velocity and x-magnetic field with equal amplitude and opposite phase in order to launch transverse Alfvén waves propagating only in the z-direction.

6. The spatial structure of the driving perturbation means that some other wave modes are also driven which have wave vector components in both the x- and z-directions. This is caused by the fact that there are gradients in the magnitude of the driven plasma x-velocity[10]. The dispersion relation (equation 1.72) along with points 2 and 4 tell us that such modes cannot be transverse Alfvén modes.

7. Transverse Alfvén modes propagate at the Alfvén speed of the plasma. Sonic modes in each fluid propagate at the sound speed in the appropriate fluid. These speeds are parameters set in each simulation.

8. Magnetosonic modes propagate at a speed dependent on frequency and direction, as determined by the dispersion relation. The fast and slow magnetosonic speeds are also functions of the Alfvén speed and plasma sound speed (see point 7).

2.5 Example Simulations: Transverse Alfvén Waves in the Plasma

Consistent perturbations were made to both the plasma velocity field in the x-direction and the magnetic field in the antiparallel direction in order to launch a pencil of transverse Alfvén waves along the direction of the background magnetic field: the positive z-direction. The spatial structure of the driving perturbation means that other wave modes in other directions are also induced, and this will be discussed below. It is worth emphasising however that although the response of a plasma-neutral mixture includes many different wave modes, the *original perturbation* was always characteristic of a transverse Alfvén wave alone.

[10]Which induces a density perturbation according to equations 2.35 - 2.42.

2.5.1 Momentum coupling off

This example shows the results of simulations which consider the plasma and neutral gas to be decoupled, i.e. the momentum coupling constant Γ in equations 2.37-2.40 was set to zero. This could represent a fully-ionised plasma, but it is also how Chandrasekhar and Fermi (1953) treated the derivation of their diagnostic method, discussed in chapter 3. They assumed that the neutral gas population of partially-ionised plasma would not respond directly or indirectly to Alfvén waves, but would instead move incoherently as normal gas does. Most, if not all, of the literature since 1953 makes this assumption as well. Therefore this example could be interpreted as what the current CF53 interpretation assumes is observed.

To illustrate the multiple wave modes that are implicated by the spatially-structured driving perturbation for comparison to later results, figures 2.5 - 2.9 show the progress of the superposition of waves induced by a pencil of Alfvén waves driven in a fully-ionised plasma. The plasma sound speed parameter r and the Alfvén speed parameter u were both set equal to unity. This generic calibration example allows comparisons to be made later in this chapter when the parameters are varied.

The figures each show eight snapshots in time of the progress of the perturbations. The axes represent the computational domain with the horizontal axis corresponding to the x-direction and the vertical axis the z-direction. The background magnetic field in the system is aligned along the positive z-direction, and for that reason that is also the direction that the driving perturbation launches Alfvén waves in.

Figure 2.5 shows the advance of perturbations to the plasma density. The fact that this plot is not empty shows already that the spatial structure of the Alfvén wave driver causes other, non-Alfvénic wave modes to be induced: for plane transverse Alfvén waves the plasma density would be completely unperturbed. However, these perturbations are caused by longitudinal pressure waves, as demonstrated by the lateral

transport of the perturbations (in the x-direction)[11]. This is particularly clear at early times, i.e. the left-hand column. At later times the fact that density perturbations spread out laterally, i.e. in the positive and negative x-direction, shows that there are non-transverse modes propagating in all directions (see point 4).

Figures 2.6 and 2.7 show the plasma velocity field in the x- and z-directions respectively. The x-velocity field is largely dominated by a transverse wave mode, i.e. the Alfvén wave mode that is characteristic of the driving perturbation. However, inspection of the plots as time advances reveals that some other structure develops, caused by the spatial structure around the driver: notice the gaps that develop in figure 2.6 as time progresses.

Furthermore, the z-velocity perturbations appear to be closely related to the density perturbations in figure 2.5. This is to be expected (point 4) and is consistent with the interpretation that these show the magnetosonic modes that are induced by the velocity gradient in the spatial structure of the driving perturbation.

The magnetic perturbations in the x- and z-directions are shown in figures 2.8 and 2.9 respectively. The perturbations in the x-magnetic field are consistent with the x-velocity perturbations, supporting the interpretation that it is the transverse Alfvén mode which is responsible for these (point 2). The additional structure (gaps in the contour plots) in the x-velocity discussed with figure 2.6 is also seen here, because the moving plasma induces magnetic perturbations.

The z-magnetic field perturbations are again consistent with both figures 2.5 and 2.7, as expected. This consistency across the three quantities density, z-velocity and z-magnetic field indicates that the perturbations are likely to have been caused by a propagating magnetosonic wave (see section 2.4.1). Isotropic transport is possible for these modes, so the perturbations propagate with components perpendicular to the magnetic field. This can be seen by observing how the perturbations spread out laterally from the more narrow origin as time progresses in figure 2.9.

[11] Recall that the driving perturbation is constrained between $x = 75$ and $x = 125$, therefore any disturbances outside that range must have an x-component of propagation.

The overall responses of the plasma to the driven perturbation are dominant transverse Alfvén waves propagating in the z-direction, and due to the spatial gradient in the magnitude of the plasma velocity at the edges of the pencil of Alfvén waves, magnetosonic modes are continually induced which are able to propagate isotropically.

2.5.2 Momentum coupling on

Instead of assuming that either 1) there is no neutral gas present; or 2) there *is* neutral gas present but the plasma doesn't interact with it, this model has been developed to treat the system *ab initio*. As an example for direct comparison to the uncoupled case, the following figures show the results of simulations with identical initial conditions but for one change: the coupling constant was set to $\Gamma = 0.1$, in code units. The neutral gas sound speed parameter was set to $s = 1$, equal to the plasma sound speed r and the Alfvén speed u. In percentage composition terms, this means the simulation studied a plasma with 50% ionisation fraction i.e. equal proportions of plasma and neutral gas in the mixture. This generic calibration example allows comparisons to be made later in this chapter when the parameters are varied.

This time the plasma-neutral interaction is important, because the momentum coupling transfers energy and momentum from the plasma to the neutral gas, and such energy is lost to the transverse Alfvén wave component of the superposition of wave modes. This will be discussed in more detail in chapter 3. Perturbations to the plasma result in the neutral gas becoming perturbed as well, and the neutral population only supports sound waves which do not directly interact with the magnetic field. However, such sound waves can feed back into the plasma later, inducing new wave modes. This cycle can continue *ad infinitum* as the momentum coupling means the two populations respond coherently to any stimulus.

The density perturbations are shown in figures 2.10 and 2.11. The momentum coupling means that the two plots are essentially identical. The density perturbations are small in magnitude but some interesting structure emerges: it is particularly apparent

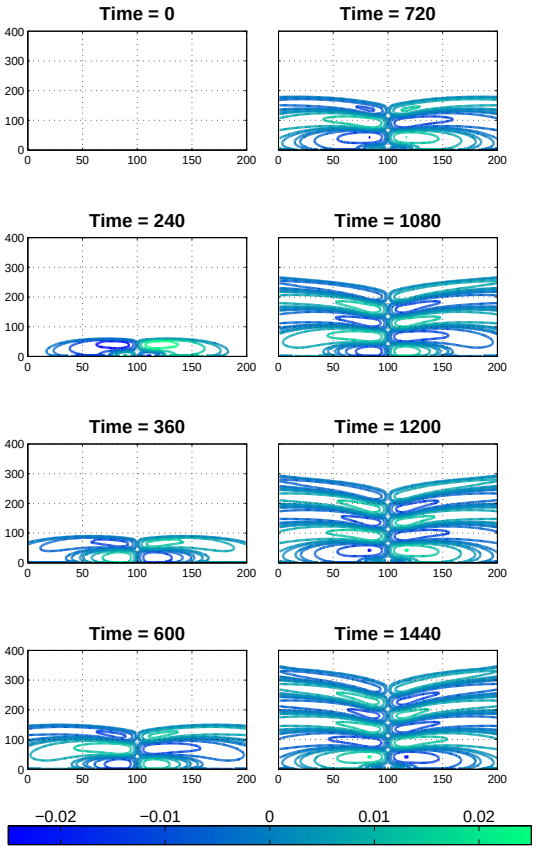

Figure 2.5: Snapshots in time of plasma density perturbations caused by a driven pencil of Alfvén waves in a pure, i.e. uncoupled plasma. The simulation parameters were $r = u = 1$, i.e. the plasma sound speed was equal to the Alfvén speed. Early times (left hand column) show compressional wave modes propagating in horizontal and near-horizontal directions from their origin near the edges of the spatial structure of the driving perturbation at $x = 75$ and $x = 125$. The only wave modes capable of causing density perturbations are compressional i.e. sonic and magnetosonic modes. The driven transverse Alfvén wave (which itself produces no density perturbations) induces these other wave modes due to the velocity gradients present at the edges of the spatial structure of the driving perturbation. The similarities between this figure and figure 2.7, along with non-transverse components present in figure 2.6 support the compressional wave mode interpretation. Similarities between this figure and figure 2.9 suggest that the wave mode primarily responsible is the magnetosonic mode.

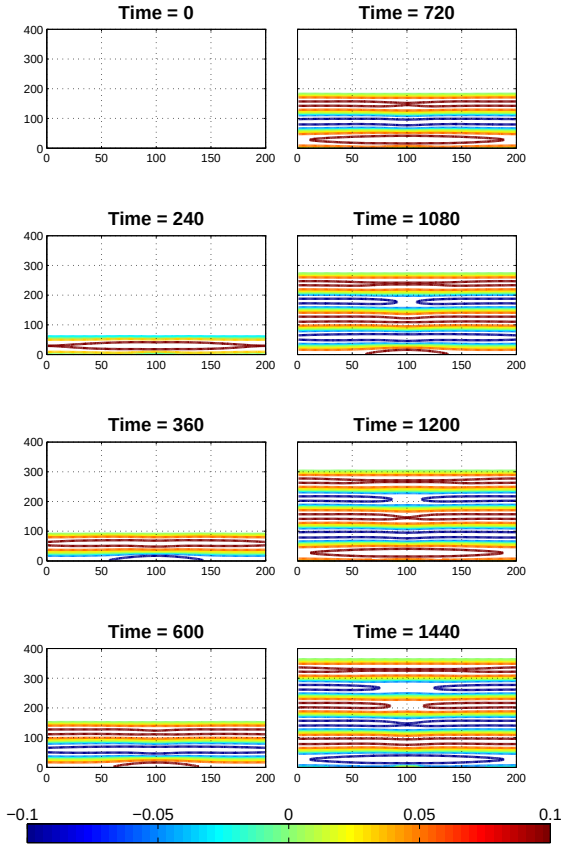

Figure 2.6: Snapshots in time of plasma x-velocity perturbations caused by a driven pencil of Alfvén waves in a pure, i.e. uncoupled plasma. The simulation parameters were $r = u = 1$, i.e. the plasma sound speed was equal to the Alfvén speed. The velocity structure is dominated by the transverse Alfvén wave mode that is characteristic of the driving perturbation (horizontal contours indicate transverse waves i.e. with the only non-zero velocity component perpendicular to the direction of propagation). This transverse motion is also seen in figure 2.8 i.e. the only other quantity characteristic of the transverse Alfvén wave mode. At later times a triangular structure develops around the centre line $x = 100$, indicating the presence of waves with non-transverse (i.e. non-Alfvén mode) components. The fact that this structure is also seen in figure 2.8 suggests that these are caused by magnetosonic modes with velocity components in both directions. The magnetsonic modes are more clearly shown in figures 2.5, 2.7 and 2.9.

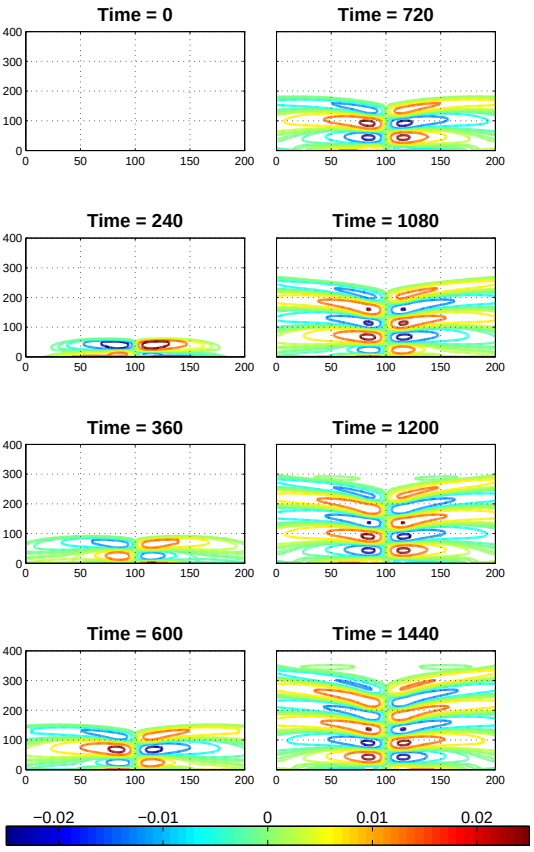

Figure 2.7: Snapshots in time of plasma z-velocity perturbations caused by a driven pencil of Alfvén waves in a pure, i.e. uncoupled plasma. The simulation parameters were $r = u = 1$, i.e. the plasma sound speed was equal to the Alfvén speed. The z-velocity perturbations are consistent with the density perturbations in figure 2.5. The fact that these have a velocity component parallel to the background magnetic field means that the wave mode responsible for them must be compressional, i.e. sonic, in nature. The correlation of these z-velocity perturbations to the z-magnetic field perturbations in figure 2.9 supports the interpretation that it is in fact magnetosonic modes that are dominant.

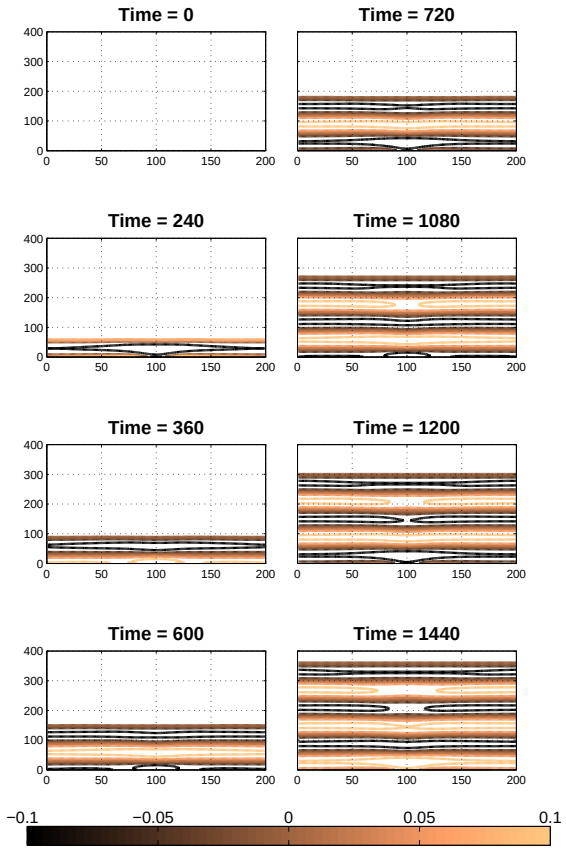

Figure 2.8: Snapshots in time of plasma x-magnetic field perturbations caused by a driven pencil of Alfvén waves in a pure, i.e. uncoupled plasma. The simulation parameters were $r = u = 1$, i.e. the plasma sound speed was equal to the Alfvén speed. The plots are dominated by the transverse Alfvén wave mode and are consistent with the x-velocity plots in figure 2.6, while the small laterally-propagating structures caused by magnetosonic feedback can also be seen in figures 2.5, 2.7 and 2.9.

at later times that there are wave modes present that were not induced in the uncoupled case. Perturbations near the edges of the domain overtake the central perturbations indicating that the wave mode responsible has a propagation speed greater than the Alfvén speed, and since all characteristic speeds are set equal in this simulation, some kind of hybrid wave must be responsible. This will be discussed later.

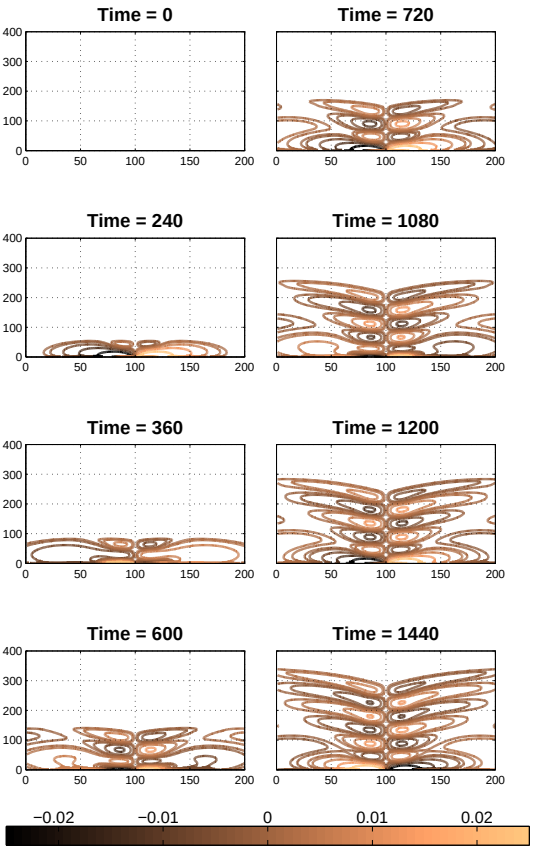

Figure 2.9: Snapshots in time of plasma z-magnetic field perturbations caused by a driven pencil of Alfvén waves in a pure, i.e. uncoupled plasma. The simulation parameters were $r = u = 1$, i.e. the plasma sound speed was equal to the Alfvén speed. Since the transverse Alfvén wave mode must have zero component of magnetic field perturbation parallel to the wave direction, these perturbations must be caused by magnetosonic modes induced by gradients in the spatial structure of the driving perturbation. This interpretation is supported by the features discussed in figures 2.5 and 2.7.

Figures 2.12 and 2.13 show the plasma velocity field perturbations in the x- and z-directions respectively. The x-velocity perturbations remain dominated by the transverse wave mode just as for the uncoupled example, while the z-velocity perturbations appear to be closely related to the density perturbations, indicating once again that longitudinal wave modes are responsible for both. The neutral gas velocity perturbations are almost identical to these figures and are not reproduced here: due to the momentum coupling the plasma and neutral gas move coherently together.

The magnetic field perturbations are, as always, closely related to the plasma velocity perturbations. Figure 2.14 shows the x-magnetic perturbations are dominated by the transverse Alfvén wave mode, while figure 2.15 depicts the magnetic perturbations in the z-direction and confirms the dominance of longitudinal magnetosonic wave modes.

2.5.3 The Plasma-Neutral Interaction between Imbalanced Populations

For comparison between different imbalanced proportions of plasma and neutral gas, the figures in this section depict all eight quantities at what is equivalent to the final snapshot in time shown in the figures in section 2.5. These figures show the system after an elapsed evolution time which is sufficient for the driven Alfvén wave to have completely crossed the domain. Individual plots show the perturbations from equilibrium for the neutral gas (left-hand column, top 3 rows) and plasma (right hand column, top 3 rows), with the bottom row showing the two magnetic field components. As before, the perturbation has propagated upwards in the positive z-direction, the simulation driver is along the bottom (x-axis) of the simulation box.

Uncoupled calibration case

Figure 2.16 shows a snapshot in the propagation of the Alfvén wave in the absence of coupling, as a contrasting calibration case to which the results from the inclusion of

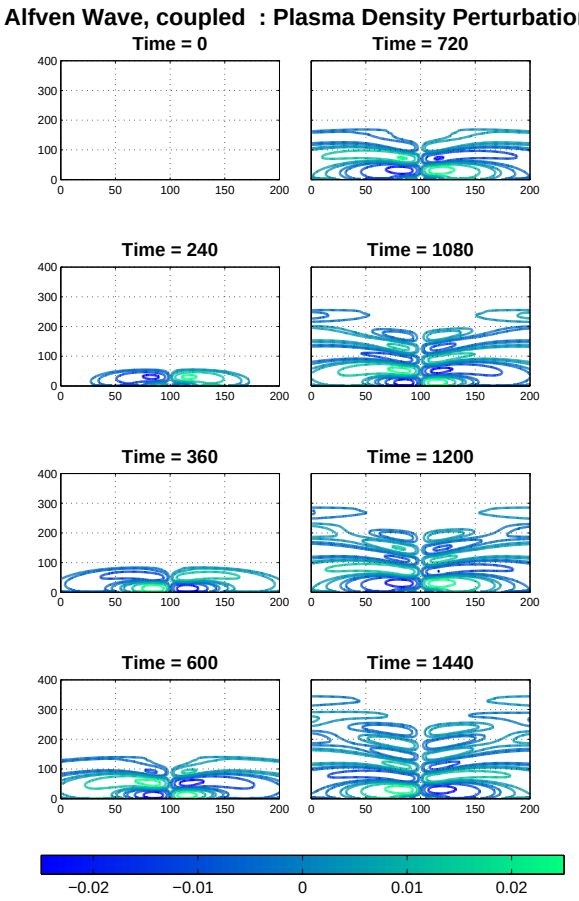

Figure 2.10: Snapshots in time of plasma density perturbations caused by a driven pencil of Alfvén waves in an equal mixture of plasma and neutral gas. The simulation parameters were $r = s = u = 1$, i.e. the plasma sound speed, neutral gas sound speed and plasma Alfvén speed were all equal. The plasma density perturbations are quite different from those in the uncoupled case (figure 2.5). Features are visible near the edges of the domain, especially at later times, that must be related to sound waves in the neutral gas. This conclusion is reached because the same features are also visible in the z-velocity figure 2.13 but *not* in the z-magnetic field.

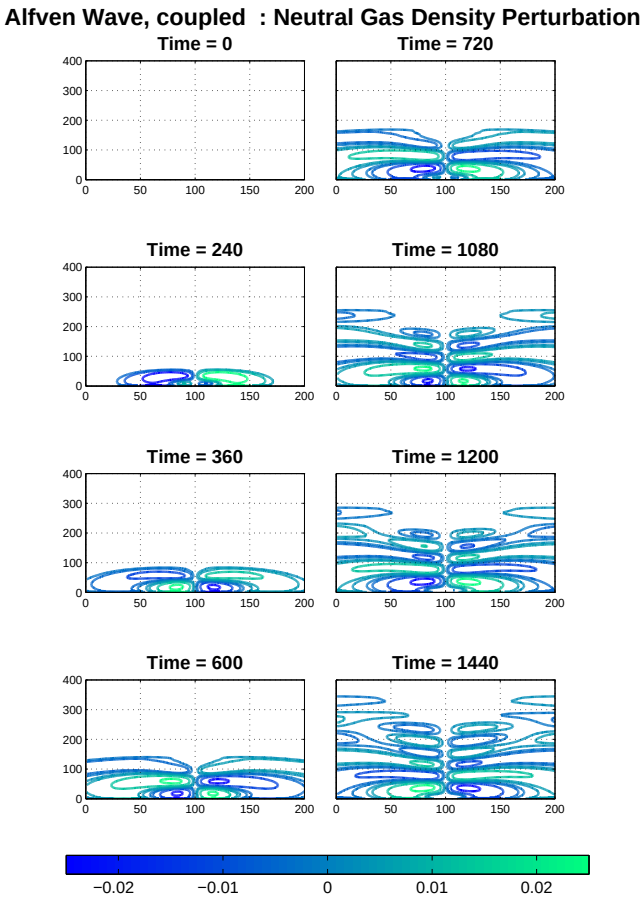

Figure 2.11: Snapshots in time of neutral gas density perturbations caused by a driven pencil of Alfvén waves in an equal mixture of plasma and neutral gas. The simulation parameters were $r = s = u = 1$, i.e. the plasma sound speed, neutral gas sound speed and plasma Alfvén speed were all equal. The momentum coupling means that the plasma and neutral gas density perturbations are almost identical, therefore this figure is almost identical to figure 2.10.

gas-coupling can be compared directly. Since the coupling is zero for this case, there is no gas perturbation. The effect of the transverse structure in the driver is clear in the plasma density (top right) and z-components of the plasma velocity and magnetic field; the spatial modulation can be seen in the x-velocity component of the plasma. Given that the non-transverse magnetic field magnitude is very small compared to the transverse, it can be concluded that the superposition is dominated by an Alfvén wave

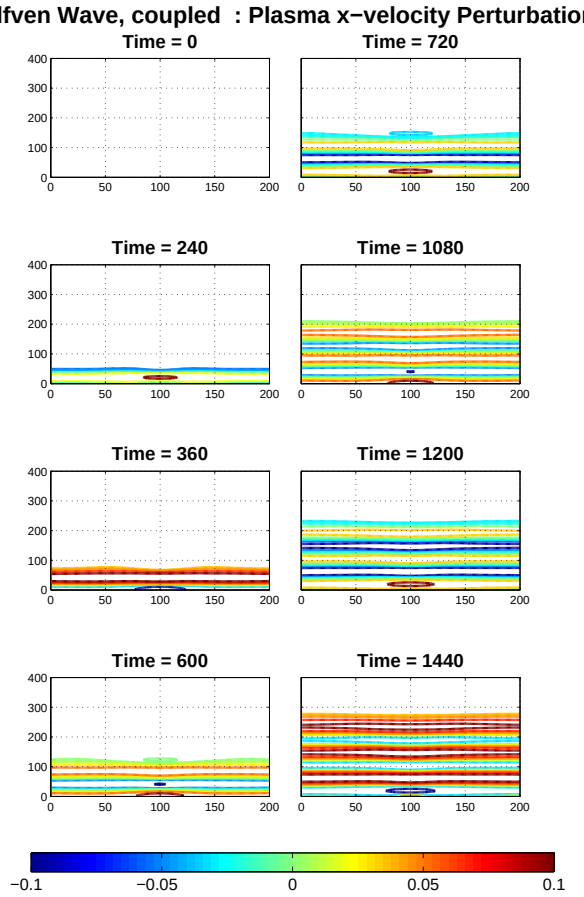

Figure 2.12: Snapshots in time of plasma x-velocity field perturbations caused by a driven pencil of Alfvén waves in an equal mixture of plasma and neutral gas. The simulation parameters were $r = s = u = 1$, i.e. the plasma sound speed, neutral gas sound speed an plasma Alfvén speed were all equal. The transverse wave structure dominates just as it does in the uncoupled case (figure 2.6), but there are other small structures developing along the centre line of propagation which indicate the presence of wave modes which have a wave vector component in the x-direction i.e. compressional waves. These features correlate by eye to the largest magnitude perturbations in figures 2.13 and 2.15, i.e. the wave mode responsible has components in both directions as well as associated magnetic field perturbations. This leads to the conclusion that it is magnetosonic modes which are responsible for the perturbations.

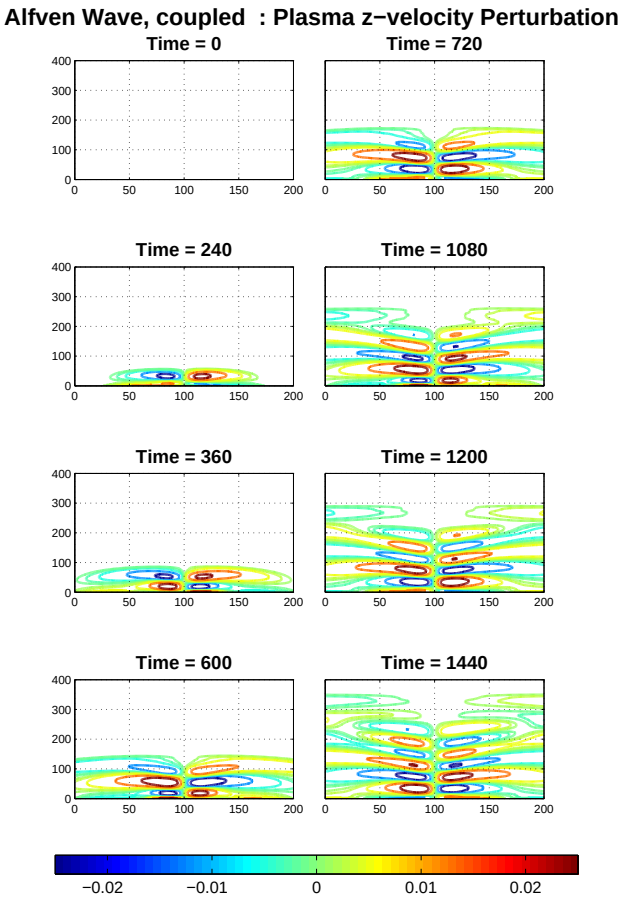

Figure 2.13: Snapshots in time of plasma z-velocity field perturbations caused by a driven pencil of Alfvén waves in an equal mixture of plasma and neutral gas. The simulation parameters were $r = s = u = 1$, i.e. the plasma sound speed, neutral gas sound speed an plasma Alfvén speed were all equal. The longitudinal nature of the wave modes responsible for these perturbations is highlighted by the close resemblance of this figure to figure 2.10. Additionally, the similarities and differences between this figure and figure 2.15 show where the superposition is dominated by magnetosonic modes (near the vertical centre line) and by neutral sonic modes (away from the centre line).

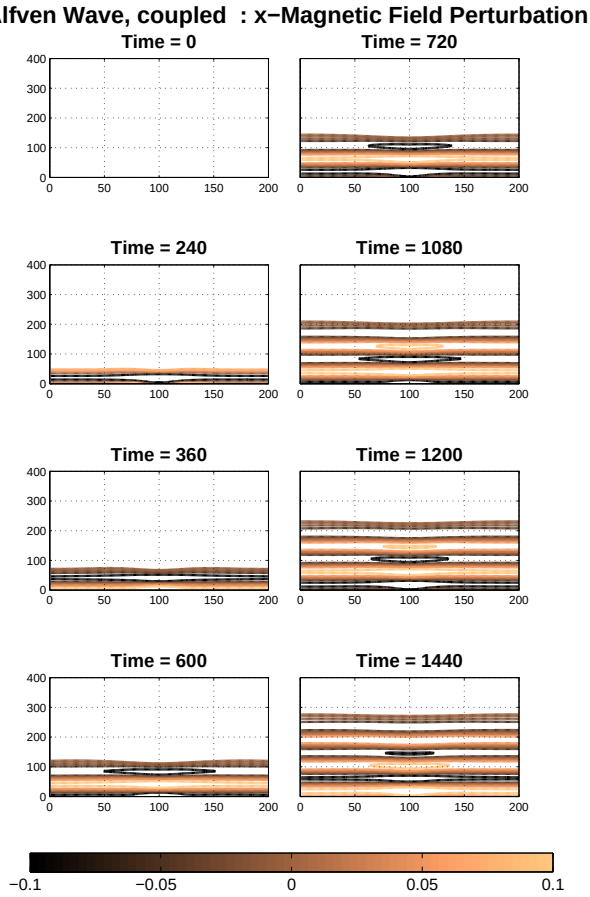

Figure 2.14: Snapshots in time of plasma x-magnetic field perturbations caused by a driven pencil of Alfvén waves in an equal mixture of plasma and neutral gas. The simulation parameters were $r = s = u = 1$, i.e. the plasma sound speed, neutral gas sound speed an plasma Alfvén speed were all equal. The transverse wave structure dominates just as it does the x-velocity (figure 2.12), but there are other small non-transverse (i.e. not plane perpendicular to the z-direction) developing along the centre line of propagation, corresponding to the highest magnitude perturbations in figure 2.15, which indicate the presence of compressional wave modes which have a wave vector component in both directions. In other words, magnetosonic modes.

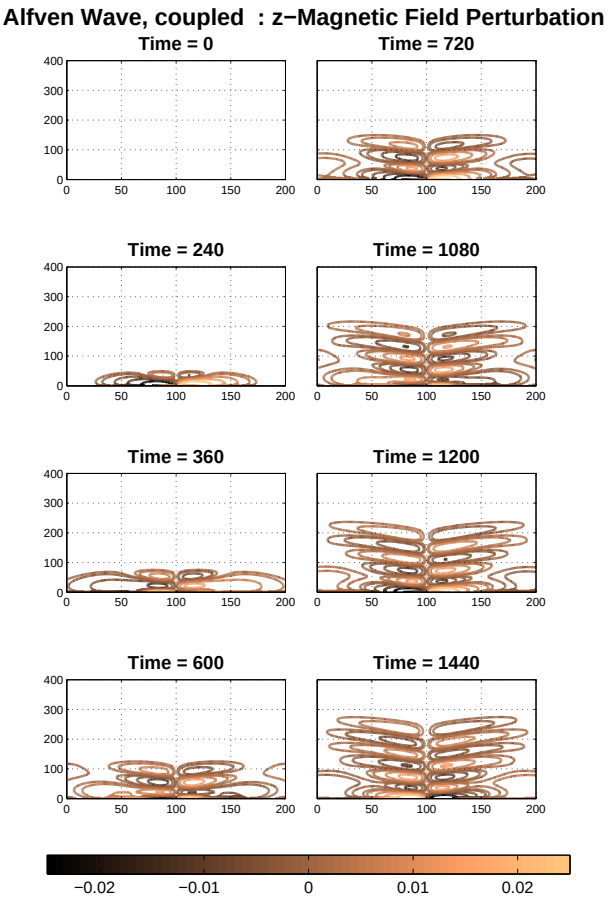

Figure 2.15: Snapshots in time of plasma z-magnetic field perturbations caused by a driven pencil of Alfvén waves in an equal mixture of plasma and neutral gas. The simulation parameters were $r = s = u = 1$, i.e. the plasma sound speed, neutral gas sound speed an plasma Alfvén speed were all equal. The longitudinal nature of the wave modes responsible for these perturbations is highlighted by the close resemblance of this figure to figure 2.10 and figure 2.13. However, features that are present in those two plots near the lateral edges of the domain are clearly not present here, indicating that magnetosonic modes dominate near the centre line while neutral sound waves are more influential further away from the driven region.

mode, with a small associated pressure wave. The density and longitudinal velocity component structure are both collimated parallel to the predominantly vertically propagating wave, with little lateral spread.

Figures 2.17, 2.18, and 2.19 show simulation results for an identical evolution time to the uncoupled simulation shown in figure 2.16. Notice the decrease in wavelength and velocity as the proportions of plasma and neutral gas are altered. Three different cases of coupled mixtures are presented for comparison.

Case 1: a plasma-dominated mixture.

The results for this case are shown in Figure 2.17. Now the plasma sound speed $r = 1$ is equal to the Alfvén speed (u=1) but greater than the neutral gas sound speed $s = 0.6$. Notice that now the neutral gas velocity and density fields are responding to the plasma via the coupling; the influence of the reverse feedback on the transverse magnitude of the plasma wave structure compared to the uncoupled case (Fig. 2.16) is evident mainly in the z-components of the magnetic and velocity fields, which are each less confined than in the uncoupled case: there is a distinct broadening of the longitudinal magnetic structure due to the presence of an additional longitudinal velocity component from the neutral gas. Given that the neutral gas is not directly influenced by the underlying magnetic field, this softening of the anisotropy of the wave characteristic is entirely consistent with the influence of the neutral gas. Notice also that the kinetic energy density of the plasma is shared with the neutral gas, reducing the magnitude of the longitudinal velocity field component of the plasma, and therefore the size of the magnetic perturbation generated by it. Moreover, since the neutral gas sound speed is different from any plasma wave speed, the neutral gas acts to dampen weakly the overall perturbation, and acts as a drag on the original plasma wave.

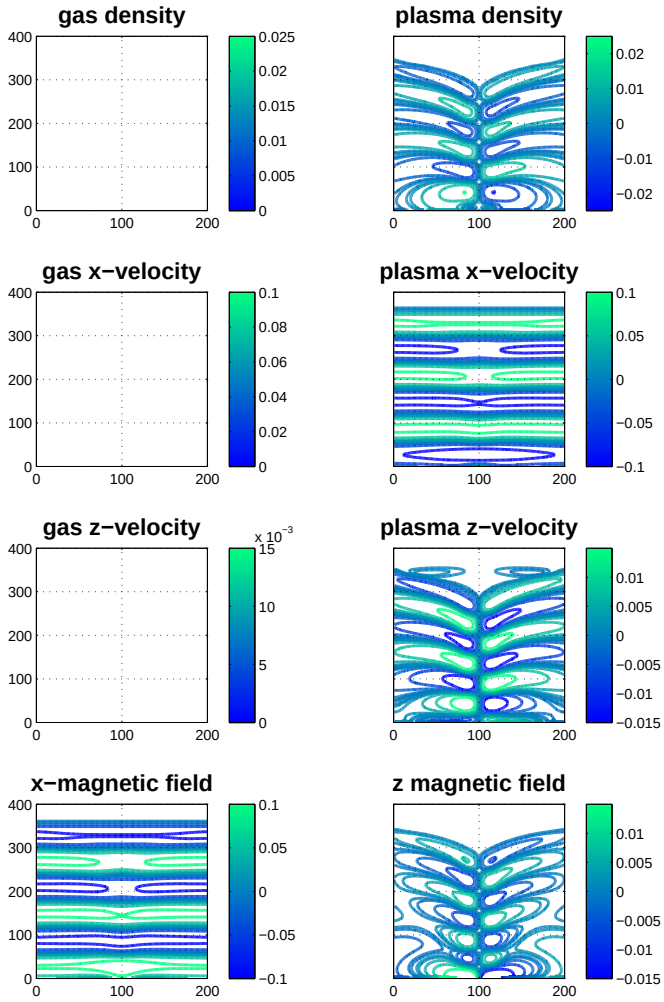

Figure 2.16: For calibration, a snapshot of the simulation results for the case of an Alfvén wave propagating in an uncoupled plasma ($r = 1, u = 1$). The axes for each subplot represent the spatial domain co-ordinates - x in the horizontal direction and z in the vertical direction. As expected, there is no influence on the neutral gas caused by the wave. The characteristic and dominant Alfvén wave driven in the z-direction can be seen in the plasma x-velocity and the x-magnetic field plots. The structure in the z-velocity and z-magnetic field is caused by the spatial structure in the driver, showing that this is not in fact a pure Alfvén wave: there are also sonic and magnetosonic modes present, although these are less prominent in the pure plasma.

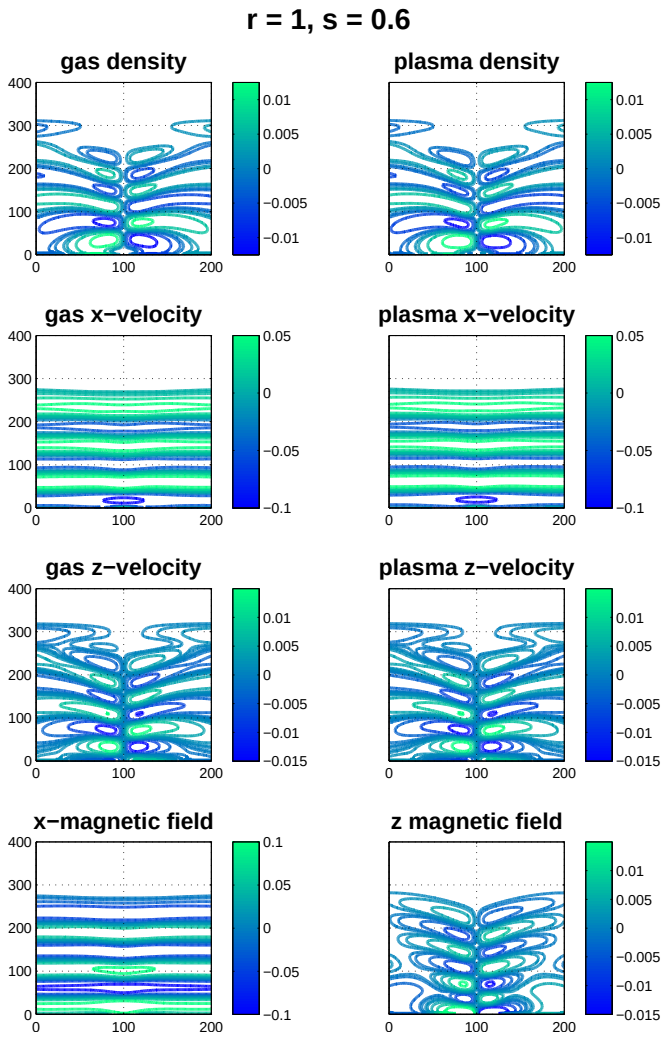

Figure 2.17: Now the coupling is switched on and the plasma population is dominant ($r = 1$, $s = 0.6$). The Alfvén speed and plasma sound speed are equal to each other and higher than the neutral gas sound speed. The density plots show how the momentum coupling means the neutral gas moves coherently with the plasma, while the z-magnetic field and z-velocity plots show the evolution of structure caused by the feedback from the neutral gas. Note that the x-axis is in the horizontal direction and the z-axis is in the vertical direction.

Case 2: parity in plasma and gas

Now in figure 2.18 the sound speed in the gas is matched with the Alfvén speed and the plasma sound speed ($r = 1$, $s = 1$), and so one might expect to see more of a resonant transfer of momentum consistent with the wave propagating at a natural speed in both media. Careful inspection of the longitudinal velocity components show that the expansion of the wavefront laterally is greater here than in the plasma dominated case of Fig. 2.17, as the isotropic character of the neutral gas response comes more into play. The coherent pencil of density and longitudinal field variations spreads out and therefore drops in amplitude as the lateral transport of the neutral gas becomes more important.

Case 3: gas-dominated mixture

Now the gas sound speed is faster than both the plasma sound speed and the Alfvén speed ($r = 1$, $s = 1.4$). The situation here, shown in figure 2.19, is significantly different from the preceding cases. Now sound waves in the neutral gas propagate much faster than any waves in the plasma, carrying energy away isotropically. The x-component of magnetic and plasma velocity fields is imposed by the driver at the $z = 0$ boundary, as before. The longitudinal variations evolve from the coupled fluid equations, and it is clear that the neutral coupling feedback is having a marked effect, diminishing and broadening the longitudinal plasma response, including the density structure.

2.6 Examples: Sound Waves in the Neutral Gas

The example of a transverse Alfvén wave shows the complexity of the combined plasma-neutral response, beginning without any directly driven density perturbations. The other side of the same coin is that sound waves in the neutral gas can indirectly induce magnetic perturbations. Turning around the previous example, if the neutral

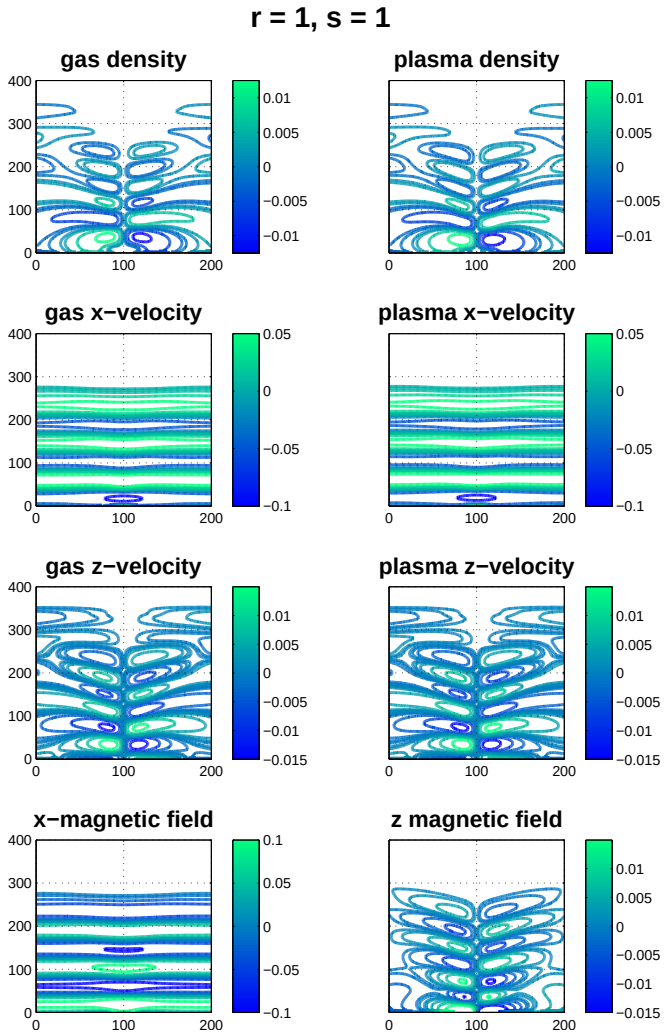

Figure 2.18: Here the simulation was run with equal parts plasma and neutral gas - i.e. the Alfvén speed and plasma and gas sound speeds are all equal ($r = 1$, $s = 1$). The neutral gas motion is not restricted by the magnetic field, so the wavefronts appear to expand laterally as seen in the z-direction plots. Note that the x-axis is in the horizontal direction and the z-axis is in the vertical direction.

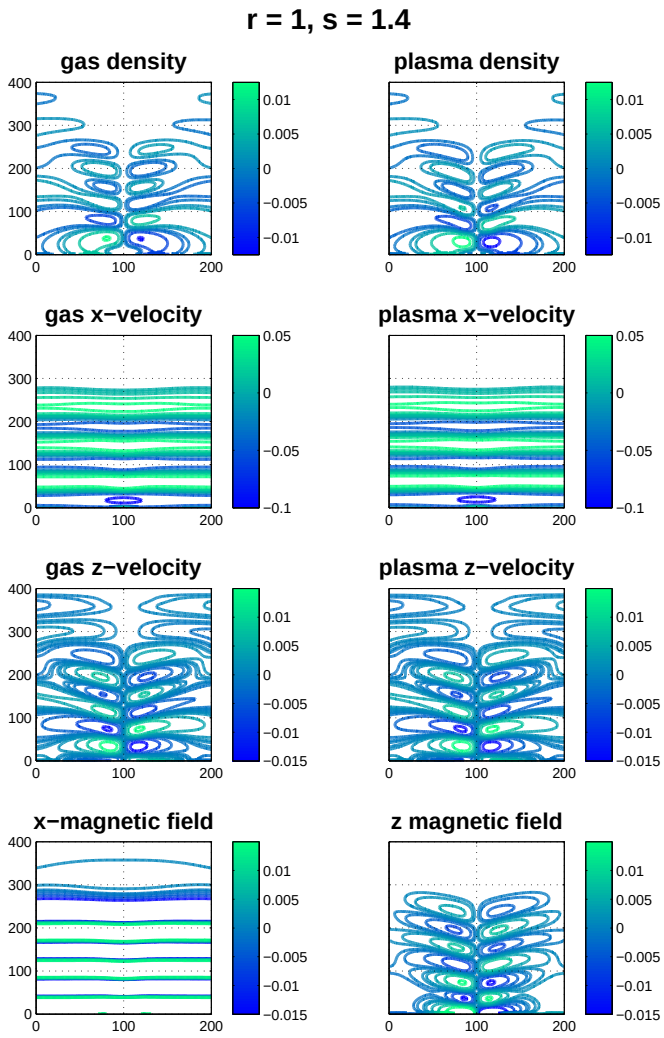

Figure 2.19: Now in a neutral-dominated mixture, the plasma sound speed is lower than the neutral sound speed ($r = 1$, $s = 1.4$). The original driven waves dominate the x-velocity plots. The energy of the Alfvén wave is transferred by momentum coupling to the dominant gas population where it is carried away *in all directions* by damped sound waves. The influence of the neutral gas can be best seen in the two density plots, and the shape of the z-velocity plots shows the sound waves induced in the gas travelling on faster than the original Alfvén wave. Note that the x-axis is in the horizontal direction and the z-axis is in the vertical direction.

gas density, and hence velocity field, is perturbed then the plasma velocity field will follow due to the momentum coupling. Any gradient in the plasma velocity field is then accompanied by a magnetic perturbation. This was highlighted in several of the figures in the previous section, but to demonstrate more clearly and show that the magnetic evolution can be influenced by initially purely neutral gas motion, it is useful to show results from simulations with just such initial conditions.

Exactly as before, consistent perturbations were made along the driving wall of the simulation, but this time the driver affected only the density field of the neutral gas. As before, to account for the computational domain being much larger than the initial perturbation, the driving perturbation had additional spatial structure added to a plane perturbation by an envelope of half-cosine form, one quarter of the width of the computational domain. This launched longitudinal sonic waves not only in the z-direction, but also some with a wave vector component in the x-direction. This is required to demonstrate the full scale of the complexity, just as in the previous example.

2.6.1 Momentum coupling off

It is helpful to consider the case of driven density perturbations in the neutral gas without including any momentum-coupled plasma. The coupling constant was set $\Gamma = 0$, and the characteristic sound speed s was set equal to 1. The driving perturbation along the side of the domain $z = 0$ launched longitudinal sound waves mostly in the positive z-direction.

The neutral gas density perturbations are shown in figure 2.20. The plots show that the dominant wave mode is longitudinal with a wave vector component only in the z-direction. Similarly to the earlier examples, there are signs of wave modes with perpendicular components which are a result of the spatial structure of the driving perturbation. Since this is neutral gas, the only wave mode supported is the sonic mode.

The neutral gas velocity plots hold few surprises as well, with the z-velocity (fig-

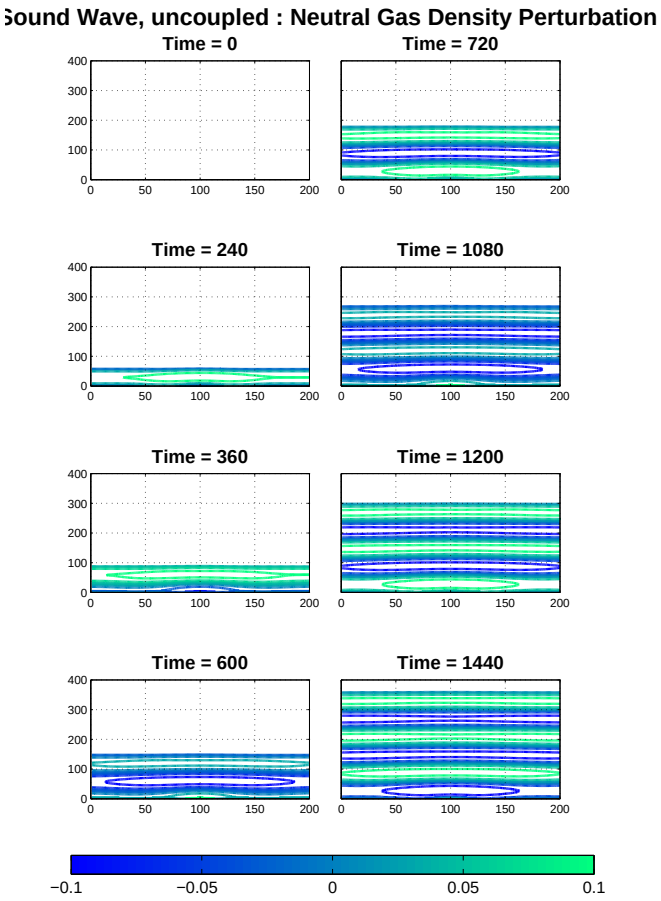

Figure 2.20: Snapshots in time of neutral gas density perturbations caused by a driven pencil of sound waves in a neutral gas. The characteristic speed was $s = 1$. The horizontal structure of the contours and correlation with figure 2.21confirms that the plots are dominated by longitudinal wave modes propagating in the z-direction, as expected.

ure 2.21) copying the density perturbations confirming that the dominant wave mode is longitudinal, while the x-velocity perturbations shown in figure 2.22 demonstrate that some wave modes with a wave vector component in the x-direction are generated and can propagate freely in any direction.

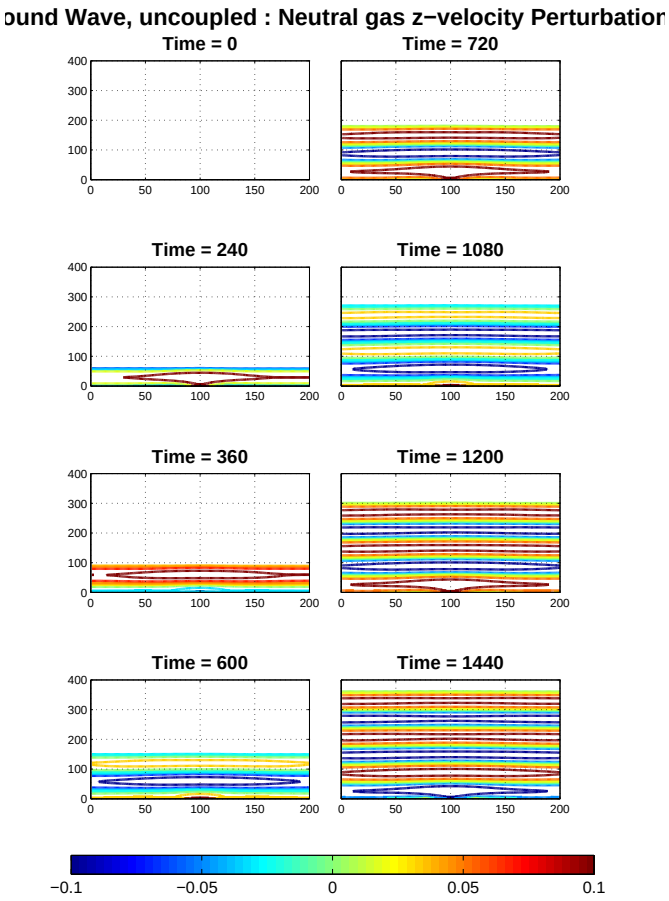

Figure 2.21: Snapshots in time of neutral gas z-velocity perturbations caused by a driven pencil of sound waves in a neutral gas. The characteristic speed was $s = 1$. Unsurprisingly, the dominant wave form is longitudinal sound waves, with the z-velocity matching the gas density perturbations shown in figure 2.20.

2.6.2 Momentum coupling on

Now the momentum coupling constant Γ was set equal to 0.1 in code units, and the same simulation was run again. The most noticeable result from this example is that magnetic perturbations can arise indirectly from density perturbations to the neutral gas. It is perhaps a self-evident fact when one considers the neutral gas and the plasma to co-exist interdependently, but this is often overlooked in the literature.

The neutral gas density is shown in figure 2.23. No significant new features are

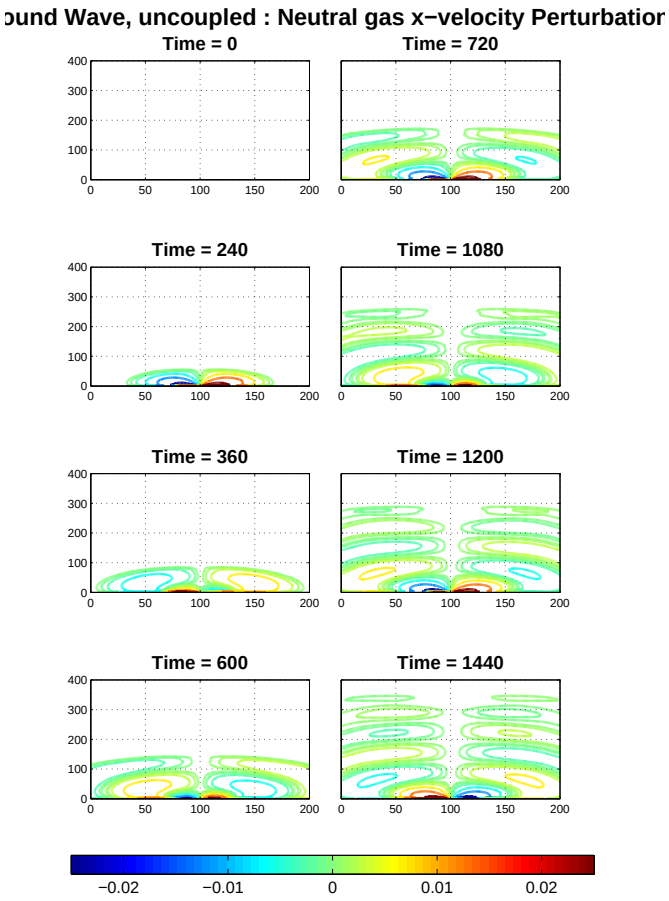

Figure 2.22: Snapshots in time of neutral gas x-velocity perturbations caused by a driven pencil of sound waves in a neutral gas. The characteristic speed was $s = 1$. The perturbations propagate with sound waves which have wave vectors with components in both the x- and z-directions.

apparent between the coupling off and coupling on cases, as the driven longitudinal wave mode still dominates.

Once again, there are no surprises with the neutral gas z-velocity plots (figure 2.24) which are similarly dominated by the longitudinal sound waves with wave vector component only in the z-direction. However, the x-velocity perturbations shown in figure 2.25 show significant differences from the uncoupled case in figure 2.22. The lateral transport is still present, but is far more uniform. In fact it appears to be mostly

constrained to the direction perpendicular to the magnetic field, i.e. without significant longitudinal wave vector components in the z-direction. This is consistent with an interpretation which says once the plasma is coupled in to the neutral gas, the magnetic field can influence which wave modes are dominant. This limits the isotropy that was available to the uncoupled neutral gas, as waves propagating in the x-direction have access to additional magnetic pressure which modes that are more diagonal do not see.

The magnetic field plots here are perhaps the most significant: the fact that there is anything at all in these figures is interesting, but the fact that even perturbations only to the neutral gas density can indirectly induce coherent magnetic perturbations is significant both for the Chandrasekhar-Fermi observational method and potentially for wider astrophysical problems[12]. Though small in magnitude, all of the magnetic perturbations induced are caused by motion of the plasma, coherently with the neutral gas velocity field. The z-magnetic field shown in figure 2.26 shows magnetosonic wave modes which, careful inspection reveals, corresponds to the non-uniform structure in both the neutral gas density (figure 2.23) and z-velocity (figure 2.24) plots. Meanwhile, the x-magnetic field plots in figure 2.27 appear closely related to the x-velocity in figure 2.25, with small differences between the two figures accounted for by the difference in colourbar scales.

2.6.3 Imbalanced Populations and Neutral Sound Waves

As for the previous example in section 2.5.3, these results show the differences between the balanced situation shown above, and cases where one population is dominant. The calibration case is shown in figure 2.28, where the plasma-neutral momentum coupling was not present.

The figure shows a snapshot of the system after an evolution time which is sufficient for the driven sound wave to have completely crossed the domain. Individual plots

[12] An explanation of a physical method of first generating magnetic fields still eludes many areas of astrophysics, for several reasons.

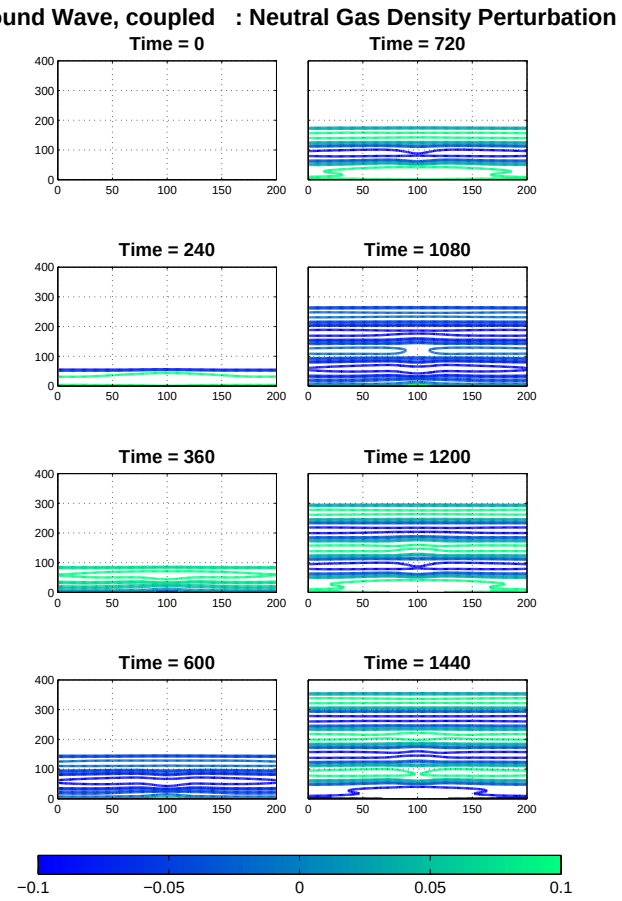

Figure 2.23: Snapshots in time of neutral gas density perturbations caused by a driven pencil of sound waves in the neutral gas population of a partially-ionised plasma. The characteristic speeds were $r = s = u = 1$, meaning the plasma and neutral gas sound speeds and the Alfvén speed are all equal. The density perturbations are dominated by the original driven sound wave but there are some small effects related to lateral transport, particularly near the central column of the plots i.e. near the edge of the spatial structure of the driver.

show the perturbations from equilibrium for the gas (left-hand column, top 3 rows) and plasma (right hand column, top 3 rows), with the bottom row showing the magnetic field components. The perturbation has propagated upwards in the positive z-direction, the driver is along the bottom (x-axis) of the simulation box.

Since the coupling is zero for this case, the plasma is not perturbed, and so there

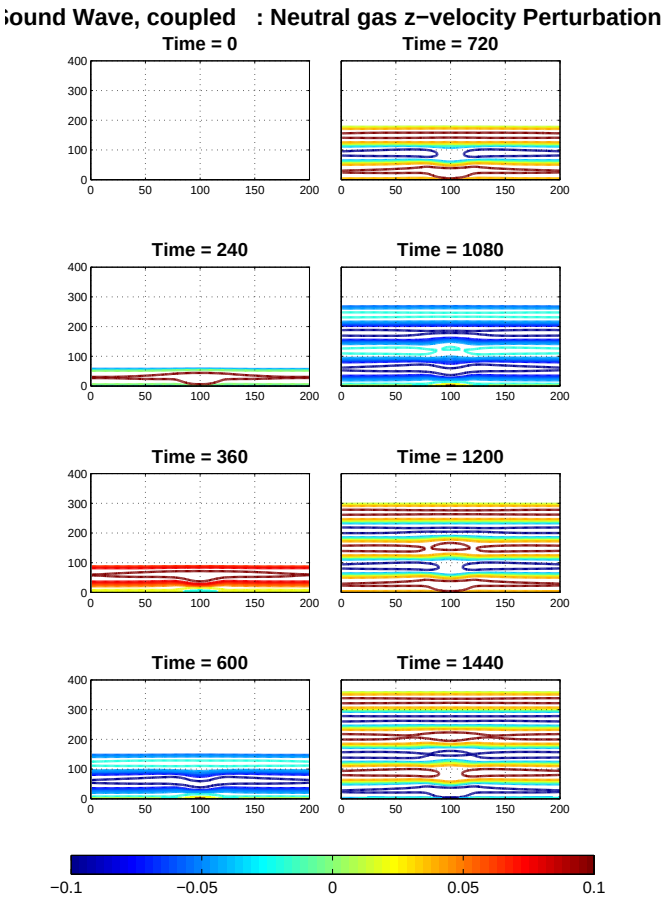

Figure 2.24: Snapshots in time of neutral gas z-velocity perturbations caused by a driven pencil of sound waves in the neutral gas population of a partially-ionised plasma. The characteristic speeds were $r = s = u = 1$, meaning the plasma and neutral gas sound speeds and the Alfvén speed are all equal. The velocity perturbations are dominated by the original driven sound wave but there are some small effects related to lateral transport, particularly near the central column of the plots i.e. near the edge of the spatial structure of the driver.

is no magnetic disturbance either. The dominant wave mode is the longitudinal wave mode seen in the gas density and z-velocity plots. The effect of the transverse structure in the driver is clear near the middle column in the x-component of the neutral gas velocity.

Figures 2.29, 2.30, and 2.31 show simulation results for three momentum cou-

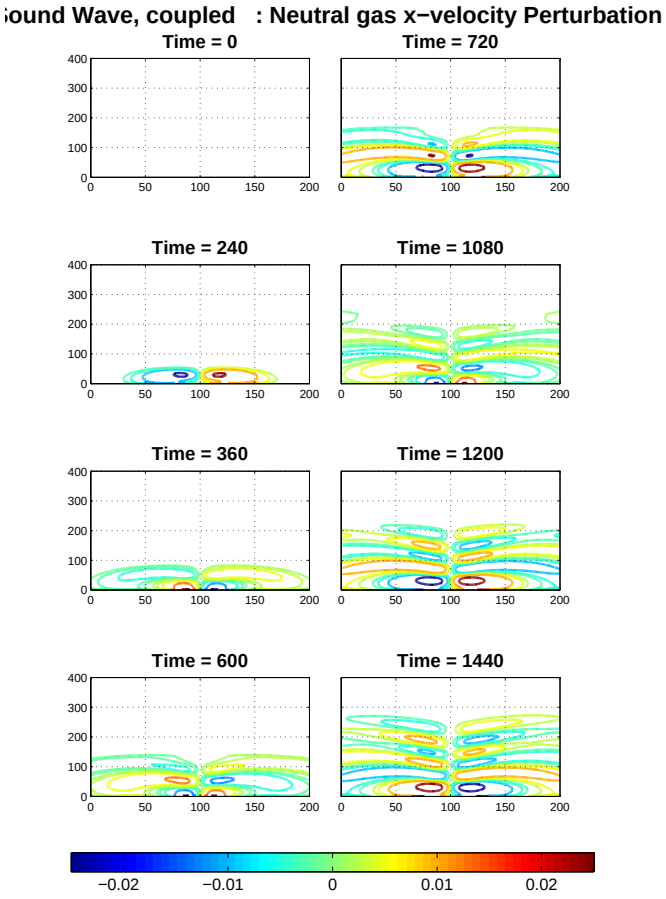

Figure 2.25: Snapshots in time of neutral gas x-velocity perturbations caused by a driven pencil of sound waves in the neutral gas population of a partially-ionised plasma. The characteristic speeds were $r = s = u = 1$, meaning the plasma and neutral gas sound speeds and the Alfvén speed are all equal. Significant differences are apparent between the uncoupled case figure 2.22 and the coupled case here. The isotropic propagation of sound waves is suppressed as the momentum coupling to the plasma means the background magnetic field can get in on the act, and sonic wave modes with only x-component of wave vector see the extra magnetic pressure available while waves propagating in other directions do not. This results in what is seen here: the velocity perturbations are more collimated, with sonic (really magnetosonic now) waves propagating along or a small angle from the perpendicular direction.

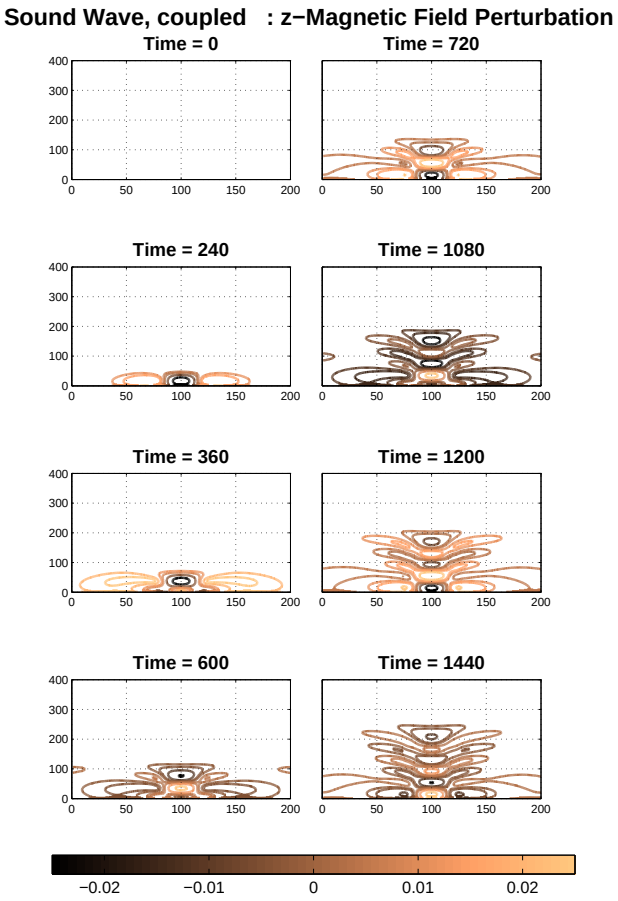

Figure 2.26: Snapshots in time of neutral gas z-magnetic field perturbations caused by a driven pencil of sound waves in the neutral gas population of a partially-ionised plasma. The characteristic speeds were $r = s = u = 1$, meaning the plasma and neutral gas sound speeds and the Alfvén speed are all equal. The perturbations are correlated to the structure seen in both the neutral gas density (figure 2.23) and z-velocity (figure 2.24) plots. This confirms that magnetosonic modes are induced which have wave vector components in both directions, as the background magnetic field is coupled in to the neutral gas motion via the gas-plasma interaction.

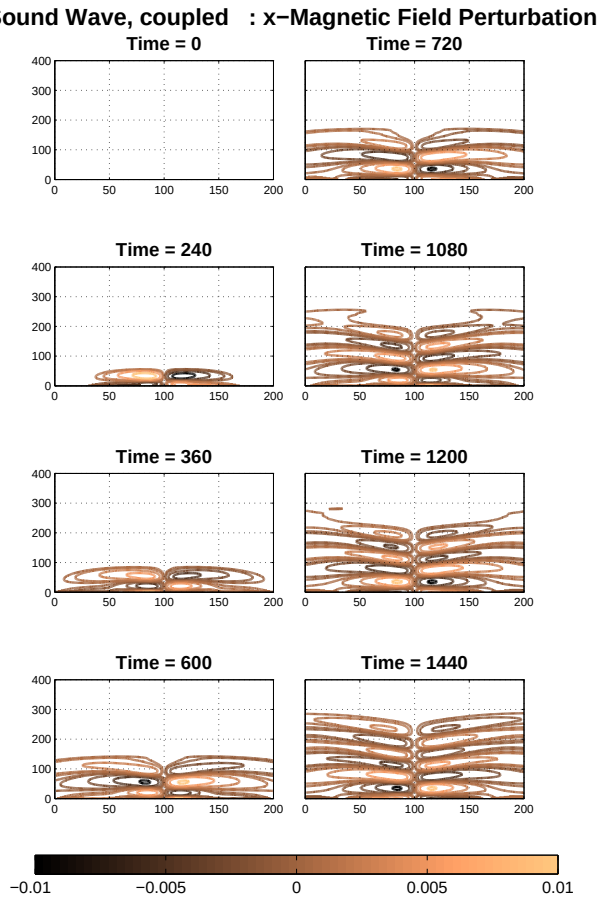

Figure 2.27: Snapshots in time of neutral gas x-magnetic field perturbations caused by a driven pencil of sound waves in the neutral gas population of a partially-ionised plasma. The characteristic speeds were $r = s = u = 1$, meaning the plasma and neutral gas sound speeds and the Alfvén speed are all equal. As before, these perturbations are directly correlated with the x-velocity since it is the gas motion that drives the plasma motion coherently, and hence a magnetic perturbation is induced. The wave mode responsible for these perturbations are magnetosonic in nature and propagate along or at an angle close to the perpendicular to the background magnetic field.

pled cases after an identical evolution time to the uncoupled simulation shown in figure 2.28.

Case 1: a neutral-dominated mixture.

The results for this case (in which $r = 0.6$ and $s = 1$) are shown in figure 2.29. Now the momentum coupling has a clear and important effect: tellingly now there are magnetic perturbations which have arisen only because of the coherent combined response of the plasma to the neutral gas being perturbed. The superposition of wave modes present is still dominated by sound waves in the neutral gas, but sonic modes in the plasma as well as magnetosonic waves are now also implicated as the plasma responds. The plasma and neutral gas populations are closely tied together, but furthermore the background magnetic field constrains the motion of *both*, as seen by directly comparing the x-velocity plots in figures 2.28 and 2.29.

Case 2: parity in plasma and gas

Now in figure 2.30 the sound speed in the neutral gas is matched with the Alfvén speed and the plasma sound speed ($r = 1$, $s = 1$). Careful inspection of the density and z-velocity plots shows that compared to figure 2.29, the wave front has travelled slightly further in the same time, indicating a faster propagation speed. The only speed in the system that has changed is the neutral gas sound speed, confirming that the dominant mode remains sound waves in the neutral gas. Furthermore, the magnetic field plots in figures 2.29 and 2.30 are nearly identical, indicating that the propagation speed has not changed. This, along with the clear similarities (near the centre vertical line) between the plasma x-velocity and x-magnetic field plots, suggest that some transverse Alfvén waves are being induced due to the spatial gradients in the driving perturbation.

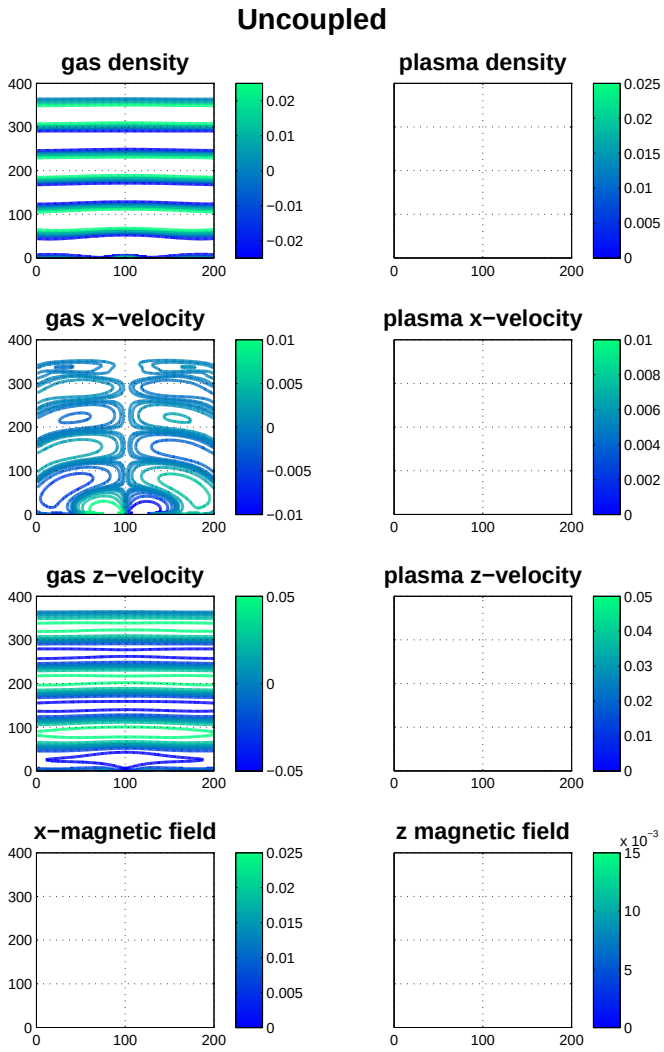

Figure 2.28: For comparison, a snapshot of the simulation results for the case of a sound wave, excited by perturbing the density to launch longitudinal sound waves, propagating in an uncoupled neutral gas ($r = 1$, $s = 1$). The driving perturbation was constrained by an envelope with cosine form half the size of the domain. The axes for each plot represent the spatial domain co-ordinates - x in the horizontal direction and z in the vertical direction. The plasma is not affected by the wave since there is no momentum coupling accounted for here. The dominant feature is the longitudinal sound wave that is prominent in the gas density (top left) and gas z-velocity plots. The disturbances in the x-velocity plot indicate the presence of sound waves with a component in the x-direction which were induced by the transverse structure in the driving perturbation.

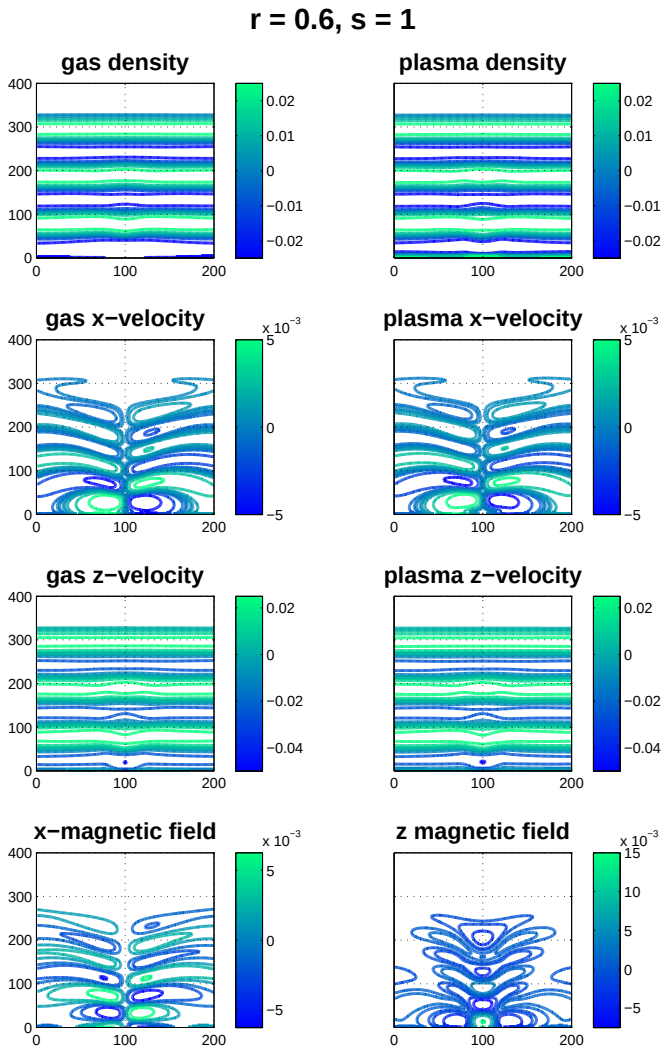

Figure 2.29: Shows the results after the coupling is switched on and the neutral gas population is dominant ($r = 0.6$, $s = 1$). The Alfvén speed and plasma sound speed are higher than the neutral gas sound speed. The density and velocity plots show how the momentum coupling means the plasma moves coherently with the driven neutral gas. Compared to figure 2.28, the x-velocity plots show the influence of the background magnetic field in terms of anisotropic transport: the perturbations are concentrated along the line $x = 100$ and spread out far less as z increases. The non-zero magnetic perturbations in both directions are related to the plasma velocity field. The important point is that this clearly shows that even a perturbation to the neutral population can have an impact on the magnetic evolution of the system. Note that the x-axis is in the horizontal direction and the z-axis is in the vertical direction.

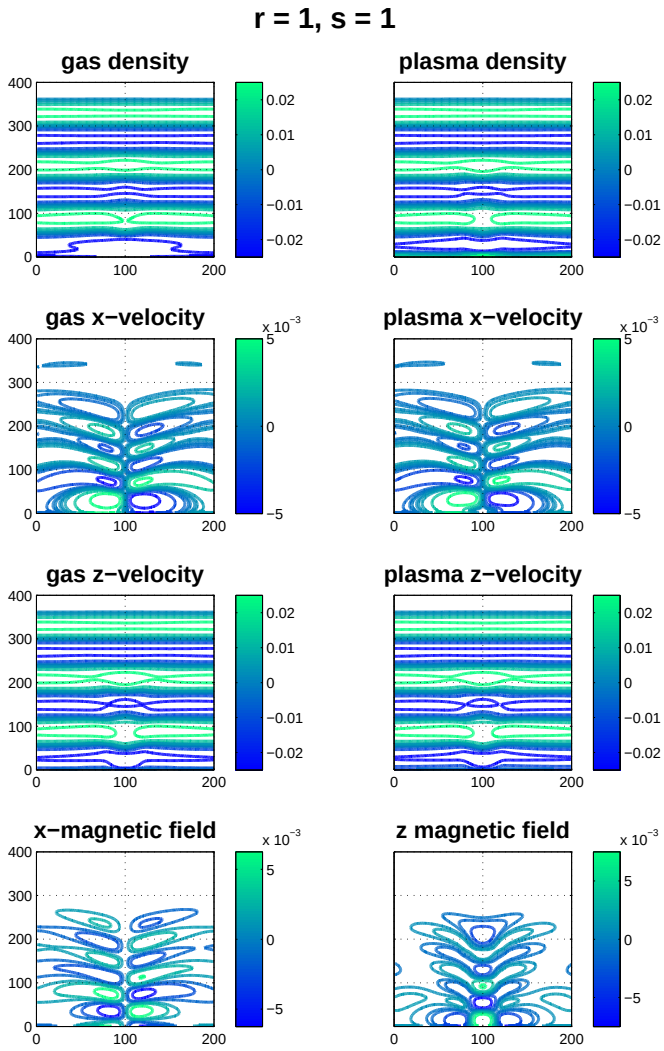

Figure 2.30: This figure shows the results for a sound wave excited in the neutral gas in an equal mixture of plasma and neutral gas ($r = s = 1$). The most noticeable difference to figure 2.29 is that the sound speed is now higher. Both sound speeds are now equal to each other and to the Alfvén speed in the plasma. The higher sound speed also allows perturbations to propagate more quickly in the z-direction as seen in the density and z-velocity plots. These perturbations are not followed by magnetic perturbations however, as there is almost no difference between the magnetic field plots in this figure and in figure 2.29. The magnetic perturbations are strongest near the centre line and appear to be closely related to the spatial structure of the driving perturbation, once again the agreement between the plasma x-velocity and x-magnetic field plots indicates the presence of transverse Alfvén modes, although these are overwhelmingly dominated by the driven sound wave.

Case 3: plasma-dominated mixture

Now in figure 2.31 the plasma sound speed is faster than both the neutral sound speed and the Alfvén speed ($s = 1$, $r = 1.4$). Not much has changed here, but there are small differences to look out for. The wave speed appears to have increased again slightly when comparing the density and z-velocity plots with those in figure 2.30, indicating that the dominant sonic mode depends on the *total* density of the mixture. In the x-velocity plots, the outer sides of the wave front are further ahead of the centre than in the earlier figures too, indicating that the isotropic momentum transfer happens more quickly in directions not parallel to the background magnetic field. Once again magnetic perturbations in both directions, including small bursts of transverse Alfvén waves (shown by the plasma x-velocity and x-magnetic field perturbations), have been induced indirectly by a purely compressional perturbation to neutral fluid.

2.7 Discussion

In this chapter the fluid model of a partially-ionised plasma has been developed. The model considers a momentum-coupled mixture of a magnetohydrodynamic fluid and a neutral fluid, with the collisional aspects between the plasma and neutral gas taken into account *ab initio* as extra terms similar to drag friction in the momentum equations of each fluid. The specific examples of transverse Alfvén waves in the plasma and sound waves in the neutral gas demonstrate that any perturbation to either the plasma or the neutral gas populations will necessarily affect *both* populations. The interaction between the plasma and neutral gas is calculated from first principles, and therefore avoids having to make any prior assumptions about the equipartition of energy between coherent and incoherent gas dynamics.

The neutral gas moves coherently along with the plasma, so Alfvén waves are modified by their interaction with the neutral population, exciting a superposition of transverse Alfvén, sonic and magnetosonic wave modes in both the plasma and the neutral

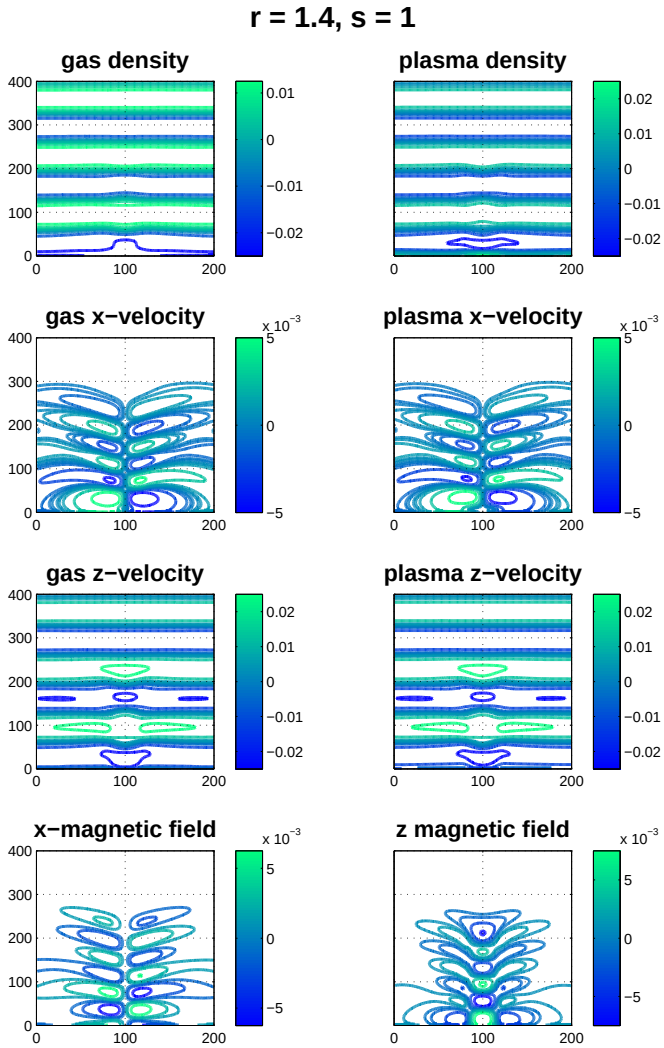

Figure 2.31: Now the plasma is the dominant population, so sound waves are faster in the plasma than in the neutral gas ($r = 1.4$, $s = 1$). The dominant wave speed appears to have increased again slightly when comparing the density and z-velocity plots with those in figure 2.30, indicating that the dominant sonic mode depends on the *total* density of the mixture. In the x-velocity plots, the outer sides of the wave front are further ahead of the centre than in the earlier figures, indicating that the isotropic momentum transfer happens more quickly in directions not parallel to the background magnetic field. Once again magnetic perturbations in both directions have been induced indirectly by a purely longitudinal perturbation to neutral fluid. Small bursts of transverse Alfvén waves, shown by the plasma x-velocity and x-magnetic field perturbations, are induced.

gas. The sonic modes in the neutral gas also feed momentum back into the plasma later, inducing further sonic/magnetosonic waves which cause further disruption. The immediate observational impact of this is in the remote diagnosis of magnetic fields in astrophysical objects. These results apply to any low-temperature, partially-ionised plasma such as, for example, the photosphere of the Sun, or the cooler edge regions of tokamaks. The general point for emphasis is that when dealing with a fluid that is composed of a mixture of two different populations, the interaction between the two populations cannot be neglected.

The crucial results from this chapter are as follows:

1. In a partially-ionised plasma, even purely magnetic disturbances such as transverse Alfv́en waves can indirectly, and coherently, implicate wave modes in the neutral component of the population.

2. Conversely, entirely neutral phenomena such as sound waves can induce magnetic perturbations in a coherent, i.e. deterministic fashion.

3. The *combined response* and interplay of wave modes must be taken into account to gain a full understanding of the response of a partially-ionised plasma to perturbative effects.

4. Analysis predicated on assumptions about equipartition of energy between e.g. the plasma velocity field and the magnetic field may not result in correct predictions about the behaviour of the system. Similarly, analysis that assumes the neutral gas motion is entirely incoherent or "turbulent" may also be incorrect.

5. In order to correctly account for the physics of partially-ionised plasmas, the coherent interaction between plasma and neutral gas wave modes must be considered.

These results apply to any partially-ionised plasma, and analogously they also apply to complex or dusty plasmas, or plasmas with populations of more than one kind of

positive ion. The effects discussed above of sound waves in the neutral population inducing magnetic perturbations in the plasma may be small, but could still be significant. For example, even a tiny magnitude magnetic field could affect the gravitational collapse of gas and dust to form stars or galaxies. Furthermore, instabilities in fusion plasmas can grow (sometimes rapidly) from small initial 'seed' magnetic fields, so it is important to consider these effects as experimental requirements become ever more precise.

2.8 Summary

This chapter set out to build on the work carried out by Diver et al. (2006) and develop the partially-ionised fluid plasma model to be applied in the specific astrophysical context discussed in chapter 3. The computational model was modified in three ways: to allow plane wave, as opposed to point, input perturbations; to handle the input of transverse Alfvén waves; and to allow the third characteristic speed to be modified, moving towards a recombining plasma model. The driving perturbation was spatially limited (2.2) such that it was of smaller scale than the size of the overall computational domain. This meant that the response of the mixed plasma-neutral population was a hybrid of the individual responses: neither perfect plasma wave modes nor perfect neutral gas sound waves were induced, but some combination of all modes propagated in the mixture.

It was shown (figures 2.5- 2.31) that when considering the momentum coupling between the plasma and neutral gas populations, the combined response to perturbations meant that if one of the plasma and neutral gas populations is excited coherently then they both move together coherently. This means that even purely neutral input in the form of sound waves in the neutral gas can induce magnetic perturbations via the plasma. Furthermore, the multiple wave modes implicated by the interaction between the populations can happen continuously: an initial Alfvén wave perturbation in the plasma will induce sound waves in the neutral gas, which can then induce new

sonic/magnetosonic waves in the plasma again, and so on. It is important to take this interaction into account when considering, say, an observational diagnostic based on Alfvén waves in the plasma. This will be discussed in chapter 3.

"The story so far: In the beginning the Universe was created. This has made a lot of people very angry and been widely regarded as a bad move."

Douglas Adams, 'The Restaurant at the End of the Universe'

3

The Chandrasekhar-Fermi Method

In this chapter the MHD fluid model of partially-ionised plasmas will be applied to study the underlying theory of one particular observational method. The results will demonstrate that in the current era of precision polarisation measurements, the details discussed in chapter 2 must now be considered when making diagnostics of magnetic field in astrophysical objects. Of particular interest is the diagnostic technique first formulated by Chandrasekhar and Fermi (1953), known today simply as the Chandrasekhar-Fermi method. Henceforth it shall be referred to as the CF53 method, or simply CF53.

3.1 History of the Chandrasekhar-Fermi Method

3.1.1 Original Motivation

The original purpose of the CF53 method was as a diagnostic to measure the magnetic field in a spiral arm of our galaxy. In their paper, Chandrasekhar and Fermi proposed two potential methods to achieve this: one involving the balance of gas pressure and magnetic pressure against gravitational collapse; the other method was to relate observed velocity disturbances and polarisation dispersion. It is the second of these methods that has endured to this day. The central assumption of CF53 is that

long wavelength, coherent Alfvén waves excited in an astrophysical plasma will propagate at the Alfvén speed and can be observed as velocity disturbances (by measuring Doppler shift) and magnetic field perturbations (from polarisation dispersion measurements). Combining these results, the background magnetic field in the plasma can be calculated, within limits taking into account the direction relative to line of sight.

At the time this was work of great foresight. They realised that the first measurements of polarisation of starlight afforded an opportunity to test the recent hypothesis about galactic-scale magnetic field in our own galaxy. Indeed they were well ahead of their time, since it is only recently that high-resolution polarisation data has become available and the full scope of their method could finally be applied.

3.1.2 Derivation

The reasoning presented in Chandrasekhar and Fermi (1953) was that if there exists in the spiral arms of our galaxy a magnetic field with a coherent scale length comparable to the radius of the galaxy, then dust particles would naturally align with the direction of the magnetic field. As starlight passes through the dust, some of it will be absorbed, but different amounts of absorption for each polarisation of light would take place depending on the direction of light propagation relative to the magnetic field. In other words, the light that reaches the observer on Earth would have no net polarisation along a line of sight parallel to the magnetic field, and maximum polarisation in the perpendicular direction. At the time of CF53, observations had just been made which suggested that the net galactic magnetic field is aligned along the spiral arm the Earth is located in within our galaxy. However there is slight deviation from the expected direction, that is there is a dispersion of polarisation that appears to suggest the magnetic field is “wavy”. Identifying the cause of these wavy lines of polarisation direction as transverse Alfvén wave modes, the CF53 derivation begins with the definition of the Alfvén speed:

$$v_A = \frac{B_0}{\sqrt{\mu_0 \rho}} \tag{3.1}$$

where B_0 is the background magnetic flux density, μ_0 is the permeability of free space, and ρ is the density of the plasma only, i.e. just the ionised material, *not* including any neutral gas or dust.

In the fluid plasma theory magnetohydrodynamics (MHD), transverse Alfvén waves are completely analogous to waves on a string, with magnetic tension replacing the usual physical tension of the string. Therefore the equation for transverse motion of a wave with wavenumber k_z, propagating in the z-direction is of the form

$$x = A \cos k_z (z - v_A t) \tag{3.2}$$

where x is the transverse direction and t is time. Next, take the derivatives with respect to z and t:

$$\frac{\partial x}{\partial z} = -Ak_z \sin k_z (z - v_A t) \tag{3.3}$$

$$\frac{\partial x}{\partial t} = Ak_z v_A \sin k_z (z - v_A t) \tag{3.4}$$

Combining equations 3.3 and 3.4 results in

$$\left(\frac{\partial x}{\partial z}\right)^2 = \frac{1}{v_A^2}\left(\frac{\partial x}{\partial t}\right)^2 \tag{3.5}$$

which is well known as the wave equation. Under the CF53 derivation, the transverse speed of the plasma at each point is caused only by the component of "turbulent" gas motion that points in the transverse direction, i.e. if v_{rms}^2 is the root mean square turbulent velocity,

$$\left(\frac{\partial x}{\partial t}\right)^2 = \frac{1}{3} v_{rms}^2 \tag{3.6}$$

where the factor of $1/3$ comes from the fact that it is only one component of the rms motion that counts. Meanwhile, Chandrasekhar and Fermi relate the spatial derivative of x to the change in the polarisation direction from a straight line projected along the direction of the background magnetic field. In other words, the change in polarisation direction is a result of a small component of perturbed magnetic field in the direction perpendicular to the background field.

$$\left(\frac{\partial x}{\partial z}\right)^2 = \theta^2 \tag{3.7}$$

where θ is approximately the (small) angle between the polarisation direction and the background magnetic field direction. Substituting equations 3.5, 3.6 and 3.7 into equation 3.1 returns the result:

$$B_0 = \sqrt{\frac{\mu_0 \rho}{3}} \frac{v_{rms}}{\theta} \tag{3.8}$$

The result means that given observational values of v_{rms}, θ and ρ, the background magnetic flux density B_0 can be inferred. That is, the large-scale magnetic field in the object being observed, be it a spiral arm, molecular cloud or nebula.

3.1.3 Modern Uses

The CF53 method is used in the literature (Falceta-Gonçalves et al. 2008; Hildebrand et al. 2009; Houde et al. 2009; Andersson and Potter 2005) to infer magnetic fields in the direction perpendicular to line of sight in objects such as molecular clouds, and does so by assuming that a linear relationship exists between the observations of line of sight velocity, magnetic field perturbations, and dispersion of the polarisation angle (PLANCK Science Team 2005; Novak et al. 2009). It has been used for almost 50 years and in that time improvements and refinements have been sought. For example, it is now possible to compare predictions made by CF53 to the results of MHD turbulence simulations as a test, before applying the results to observations made to infer magnetic field strength in distant objects. Like every other kind of astronomical observation, all that the observer has to go on is a small quantity of light. Therefore it is important that the limited information gathered is interpreted properly, in order to gain the maximum possible physical insight from the observations.

Recently several major missions commenced that will dramatically improve the precision of available polarisation observations. The PLANCK cosmic microwave background (CMB) explorer satellite completed its first full year of surveying in mid-2011 (PLANCK Science Team 2005; Planck Collaboration et al. 2011b,c). The satellite has been mapping the full-sky temperature anisotropies and polarisation of the CMB. One of the primary goals of PLANCK is to study magnetic fields in the Uni-

verse, in both cosmological and astrophysical settings (Enßlin et al. 2006; Aumont and Macías-Pérez 2009; Baccigalupi 2010). Also in 2011, the SOFIA mission finally began flights (Gehrz et al. 2011). SOFIA is a fascinating experiment consisting of a modified Boeing 747 that can fly above most of the water vapour in the Earth's atmosphere, allowing infrared observations over a wide wavelength range, almost completely free from absorption. Polarimetry will also be a major part of SOFIA's studies. These missions, along with others in the future, will provide polarisation measurements allowing unprecedented precision in the study of magnetic fields in astrophysics.

However, it is of paramount importance that this fantastic data is not misinterpreted. There is already evidence in the literature that the CF53 method needs to be refined. Magnetic field strength inferred using the CF53 method has been found to be out of step with that calculated using other methods and CF53 has appeared to have overestimated by about a factor of 10 (Mao et al. 2010) or even by as much as a factor of 90 (Bhat and Andersson 2011). In a recent paper (Chapman et al. 2011), it was reported that CF53 *underestimated* by a factor of up to 4, when compared directly to another method (Hildebrand et al. 2009). Others such as Heitsch et al. (2001) and de Avillez and Breitschwerdt (2004) explicitly question one of the assumptions made in CF53, that is the assumption of equipartition of energy between the Alfvén wave-induced plasma motion and magnetic perturbations.

Despite the unprecedented precision in the observations now available, the current interpretation leads to systematic errors in the inferred results. Attempts have been made recently to improve the CF53 method; comparisons have been made between the observed polarisation dispersion and MHD simulations in order to gain more insight using modern methods of modelling turbulence (Zweibel 1990; Heitsch et al. 2001; Ostriker et al. 2001). These authors seem to make the same assumption as CF53 did, that the neutral gas velocity contribution is due only to incoherent motion. However, Heitsch et al. (2001) in particular concluded that CF53 overestimates the true magnetic field, and they did question some of the starting assumptions made in applying the CF53 method.

By modelling the plasma-neutral interaction ab initio, the assumptions made in CF53 can be tested and this will provide insight into possible refinements for the theory.

3.1.4 Areas for Refinement

Due to the complex, hybrid response of the plasma-neutral mixture discussed in the previous chapter, the CF53 method may need to be refined and certain assumptions may need to be re-examined. The CF53 method assumes that a pure Alfvén wave is observed, and that all magnetic evolution propagates at the Alfvén speed. In fact it is impossible to avoid a superposition of waves being excited in the plasma-neutral mixture. This means that the magnetic evolution can progress at multiple characteristic speeds, therefore one cannot unambiguously infer the background magnetic field from such observations. If it is assumed that *only* Alfvén waves are present then the inferred magnetic field will be incorrect. The method will over- or under-estimate depending on whether the true evolution speed is lower or higher than the Alfvén speed respectively.

The CF53 method distinguishes between the plasma and neutral populations by considering both conducting and non-conducting species velocities, with only the former entering the Alfvén speed. The plasma-neutral interaction is considered by assuming that the neutral gas motion is random and incoherent, and that only one third of the random motion needs to be considered to deduce information about the Alfvén speed. However, the Alfvén wave is not random and incoherent, and due to the collisional momentum coupling between the two populations, the neutral gas actually follows the plasma behaviour in a coherent way. Additionally, the motion is imposed via the fluid limit, in which the random motion is assumed to be averaged out over the bulk behaviour. Since the plasma and the neutral jointly contribute equally to the magnetic evolution (in the sense that the plasma generates the magnetic perturbation, but only at the expense of dragging the neutrals along with it) the CF53 result will have to be refined.

The three specific problems in the current interpretation of CF53 to be highlighted are:

1. It is assumed in CF53 that the speed of any wave excited in the plasma-neutral mixture is equal to the Alfvén speed, i.e. that the wave is just a transverse Alfvén wave. However, this is not the case; the combined response is not a pure mode of either medium. This means the assumption that the magnetic structure evolves at the Alfvén speed may not be a good one, especially since the propagation speed varies with direction.

2. CF53 assumes that the neutral gas contribution to the observed velocity dispersion is only due to turbulent, incoherent motion. In the fluid limit, the random motion is assumed to be averaged out over the bulk behaviour. In this limit, the neutral gas and plasma are entrained in a mutually coherent response. This might actually clarify the interpretation of Doppler velocity measurements, since if it can be assumed that the plasma and neutral gas are moving together then separating the motions is not an issue.

3. Finally, the averaging of the polarisation dispersion may need to be revised to take into account the superposition of wave modes and the different influence that each mode has on the magnetic field perturbations. For example, there are longitudinal magnetic perturbations which would not be generated without the plasma-neutral interaction. Assuming that only a transverse Alfvén wave caused the magnetic structure could lead to inaccurate results.

3.2 The Partially-Ionised Fluid Plasma Model and CF53

The fluid model developed in chapter 2 affords a way of testing the CF53 method with a slightly different physical model than is normally used in the literature. Specifically, it allows comparison between what the CF53 method expects to observe, and what

the partially-ionised fluid plasma model expects to observe. The two main areas of contrast are

1. CF53 assumes energy is equipartitioned between the plasma kinetic energy and magnetic potential energy. The partially-ionised fluid model makes no such assumption.

2. Modern applications of CF53 usually assume a certain turbulent, incoherent form for the neutral gas motion and interaction with the plasma. Here no such assumption is made, and the plasma and neutral gas motion are both treated from first principles using the momentum coupling term.

3.2.1 The Impact of Momentum Coupling

For an incident pencil of transverse Alfvén waves with a cosine envelope giving spatial structure to the driving perturbation, exactly as described in the previous chapter, figures 3.1 and 3.2 show a snapshot of the x-velocity and x-magnetic field along the line $x = 100$ in the domain for two cases. These figures show a 1-dimensional slices in the z-direction through the velocity and magnetic field subplots of figures 2.16 and 2.18. This represents a view of the plane perpendicular to the observer's line of sight. Figure 3.1 shows the results for a mixture composed of equal parts plasma and neutral gas (the plasma sound speed, neutral gas sound speed, and Alfvén speed are all equal i.e. $r = s = 1$), but with coupling constant $\Gamma = 0$ i.e. no momentum coupling between the plasma and neutral gas. Figure 3.2 shows the results for identical initial conditions, this time with the momentum coupling between the two species taken into account ($\Gamma = 0.1$).

In both figures, the dashed green line shows the magnitude of the magnetic perturbation in the x-direction and the solid blue line shows the magnitude of the plasma x-velocity. For completeness, the dashed blue line shows the magnitude of the neutral gas x-velocity.

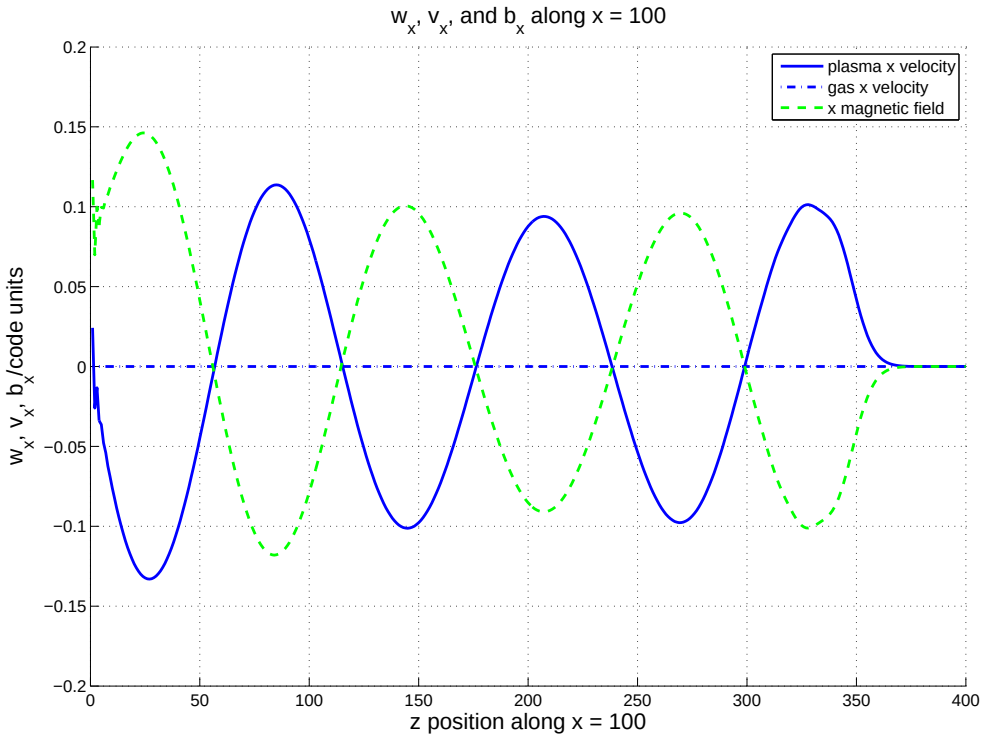

Figure 3.1: This plot shows a 1D slice along the line $x = 100$ in the velocity and magnetic field subplots of figure 2.16 - i.e. this is the plasma x-velocity, neutral x-velocity and the magnetic field perturbation (in the x-direction). The neutral gas velocity is zero because there is no momentum coupling between the plasma and neutral populations. The sinusoidal form of the perturbations indicates that, as expected, the wave mode mainly responsible for propagating them is the transverse Alfvén mode. This figure effectively represents what the CF53 method assumes has been observed when it is used to infer background magnetic field magnitudes.

It is clear that the momentum coupling makes a significant difference to the progress of the wave. A diminished wave continues across the domain, because although the energy in the initial Alfvén wave is equipartitioned between the plasma kinetic energy and magnetic potential energy, by the second half of each wave cycle some of the kinetic energy has been coupled and hence transferred to the neutral gas, which cannot interact with the magnetic field. Each half cycle the kinetic energy that can be recovered by the magnetic restoring force of the wave is less than in the previous half cycle. Physically this energy can be carried away isotropically by sound waves in the neutral

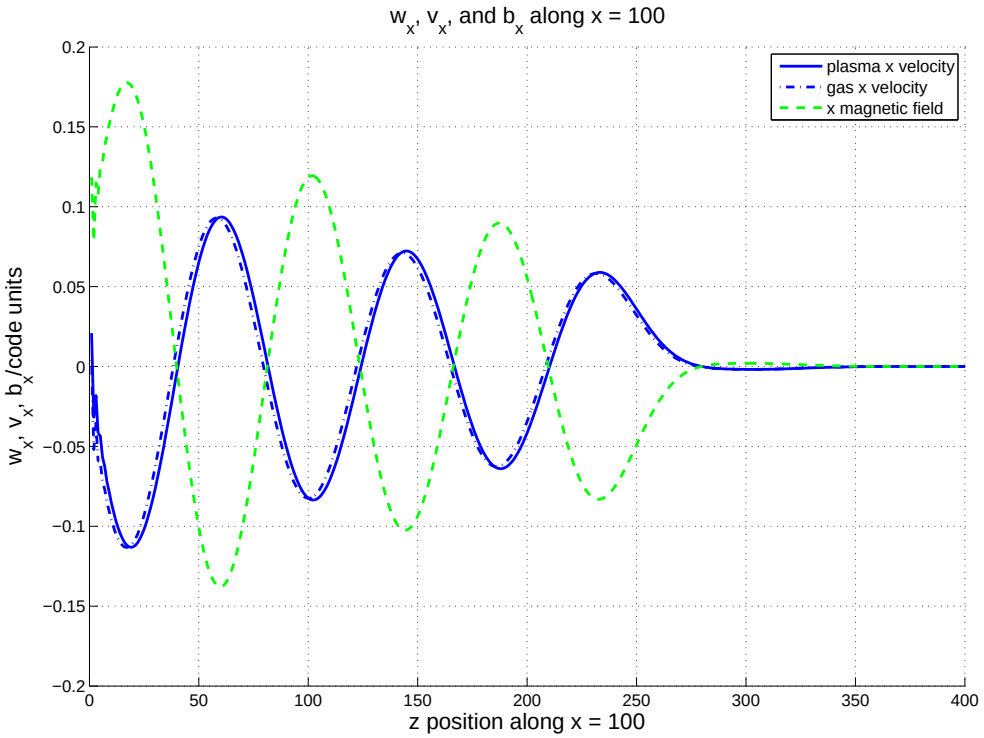

Figure 3.2: This plot shows a 1D slice along the line $x = 100$ in the x-velocity and x-magnetic field subplots of figure 2.18. This plot is for otherwise identical initial conditions to figure 3.1, the only difference is that the momentum coupling between the plasma and neutral populations is taken into account here. The sinusoidal form of the perturbations indicates that the wave mode mainly responsible for propagating them is the transverse Alfvén mode. The magnitude of the perturbations is damped as the wave progresses, because the momentum is shared between the plasma and neutral gas populations meaning that less energy is recoverable as magnetic potential energy during each subsequent wave cycle.

gas, and in the simulations energy can leave the system by crossing the transparent boundaries.

Careful inspection of figure 3.2 reveals that (i) there is a slight phase lag between the plasma x-velocity and neutral gas x-velocity perturbations, as expected due to the momentum coupling, and (ii) unlike in the uncoupled case, the peak magnitudes of the velocity terms are always noticeably less than the corresponding peak magnetic field magnitudes. Each half cycle some of the kinetic energy gained by the plasma

moving to sustain the wave is coupled into the neutral gas, meaning that in the next half cycle less kinetic energy is recoverable into magnetic potential energy by the magnetic restoring force of the wave. The "lost" energy has been mode-converted into, initially, sound waves in the neutral gas which can propagate isotropically, inducing further sonic and magnetosonic waves in the plasma as they move.

3.2.2 The Energy Transfer Between Wave Modes

In chapter 2 it was shown that an initially-driven Alfvén wave will induce sonic and magnetosonic modes in a plasma/neutral gas mixture by demonstrating that certain quantities such as density and the velocity fields were perturbed in particular ways. However, a more direct picture of the energy transfer between wave modes can be shown by comparing the kinetic energy of the plasma and neutral gas motion in each direction with the magnetic potential energy which acts as the restoring force for transverse Alfvén waves. Figures 3.3 and 3.4 show that the energy associated with transverse Alfvén waves is equipartitioned in the uncoupled plasma as expected. However, in a plasma/neutral gas mixture compressional waves in the neutral gas carry much of the energy away, draining energy from the quantities related to the transverse Alfvén mode. This is for an equal mixture of plasma and neutral gas, as an example.

3.2.3 The Change in Wavelength

A direct comparison between the coupled and uncoupled cases demonstrates the change in the wavelength of the dominant wave mode. The plasma is being driven magnetically through initially static neutral gas, which exerts a pressure acting against the plasma motion. Hence the gas pressure opposes the magnetic pressure rather than adding to it, and so one would expect the slow magnetosonic mode to be excited. See section 3.2.2 for a clearer depiction of this. This transfer of energy between modes is entirely consistent with e.g. the work of Kulsrud and Pearce (1969), but it is important to note that their formulation is in the Fokker-Planck limit, a quite different regime

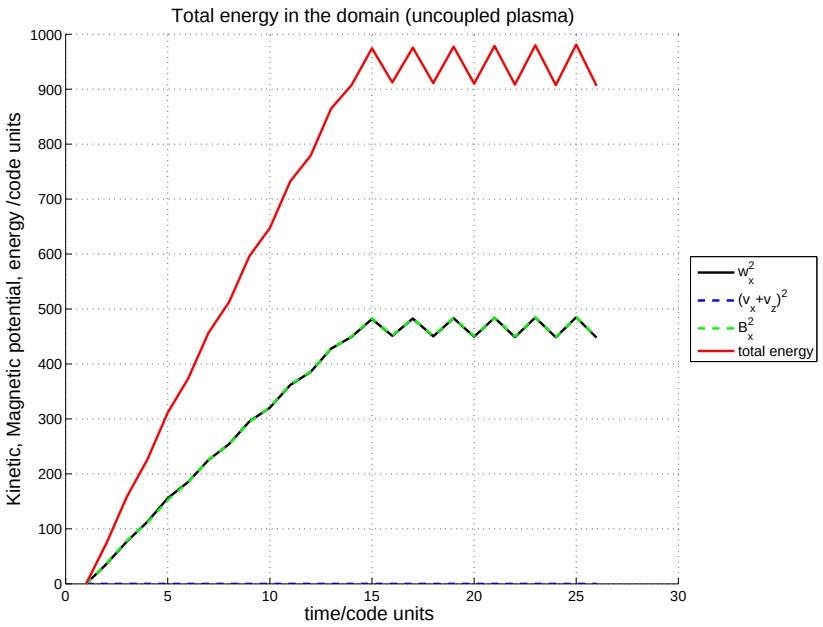

Figure 3.3: The time evolution of the total energy in the domain as kinetic energy and magnetic potential energy. Driven transverse Alfvén wave in an uncoupled plasma ($r = u = 1$). The total energy rises since the driving perturbation is constantly putting energy into the system. Eventually the total plateaus when wave modes reach the edges of the domain and propagate through the transparent boundaries. The energy 'stored' in the two quantities that are related to the transverse Alfvén wave, x-magnetic field (B_x) and plasma x-velocity (w_x), are always equal - indicating that in this uncoupled example the CF53 assumption of equipartition of energy is valid. The sawtooth features are a result of interference between the driving and data sampling frequencies.

from the long-wavelength, hydromagnetic limit that we are working in here.

It can be seen in figures 3.1 and 3.2 that the wavelength drops about 30% when the momentum coupling is taken into account, indicating that the character of the wave has changed: The combined response can no longer be a pure transverse Alfvén wave because the momentum coupling creates a density perturbation with a component along the wave vector, leading to a compressible contribution. This allows the slow magnetosonic mode to assert itself, leading to isotropic energy transfer. Meanwhile the density perturbations can also induce ordinary sonic waves in the plasma and the neu-

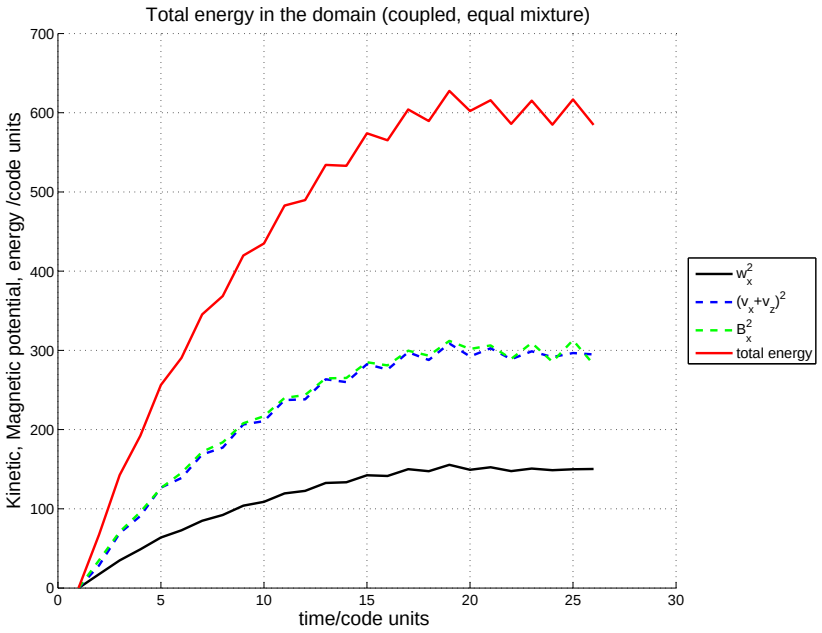

Figure 3.4: The time evolution of the total energy in the domain as kinetic energy and magnetic potential energy. Driven transverse Alfvén wave in an coupled equal mixture of plasma and neutral gas ($r = s = u = 1$). The total energy rises since the driving perturbation is constantly putting energy into the system. Eventually the total plateaus when wave modes reach the edges of the domain and propagate through the transparent boundaries. The energy 'stored' in the two quantities that are related to the transverse Alfvén wave, x-magnetic field (B_x) and plasma x-velocity (w_x), are now decoupled: only roughly half of the transverse magnetic energy is related to Alfvén waves (recall that transverse Alfvén waves can *only* have w_x and B_x components, nothing else), while the other half *must be* related to compressional wave modes as shown by the magnitude total neutral gas kinetic energy ($v_x^2 + v_z^2$). The coupling between the plasma and neutral gas quite clearly breaks the equipartition of energy between transverse magnetic energy and transverse plasma kinetic energy. The sawtooth features are a result of interference between the driving and data sampling frequencies.

tral gas. A superposition of different plasma *and* neutral wave modes is excited because of the interaction between the two populations.

To illustrate the wavelength change clearly, figure 3.5 directly compares the x-component of the magnetic field for the same two cases as in figure 3.1 and figure 3.2. It is clear that in the coupled case, the dominant magnetic structure evolves at a speed about 25% slower than the Alfvén speed (indicated by the uncoupled example which remains dominated by the original transverse Alfvén wave). See figures 3.7 and 3.6 later for further examples of the changing propagation speed of magnetic perturbations.

3.2.4 The Change in Magnetic Evolution Speed

With momentum coupling between the plasma and neutral gas populations, magnetic perturbations do not necessarily propagate at the Alfvén speed. A key assumption in CF53 is that all magnetic evolution happens at that speed. This assumption could lead to incorrect results when inferring the background magnetic field.

In the following figures the results from several simulation runs are shown. In all cases, the input driving perturbation was the same as for the simulation runs in the previous section, i.e. a pencil of transverse Alfvén waves generated by consistent perturbations to the plasma x-velocity field with equal and opposite perturbations to the x-magnetic field. Once again a cosine form spatial envelope was applied to the driving perturbation as shown in figure 2.2.

The propagation speed of transverse magnetic perturbations in simulations with different parameters can be compared by considering the number of timesteps it takes for x-magnetic perturbations to reach a single point of reference. The timestep that perturbations to b_x were first detected at the point ($x = 100$, $z = 300$) was recorded for each case studied. To eliminate noise, perturbations were considered to be detected when a minimum gradient magnitude of 10^{-5} was present at the point[1]. Similarly, the

[1]The Lax-Wendroff solver provides the dominant accuracy limit and is accurate to second order (h^2 for step size h), so any fluctuations smaller than 10^{-5} are considered to be random noise.

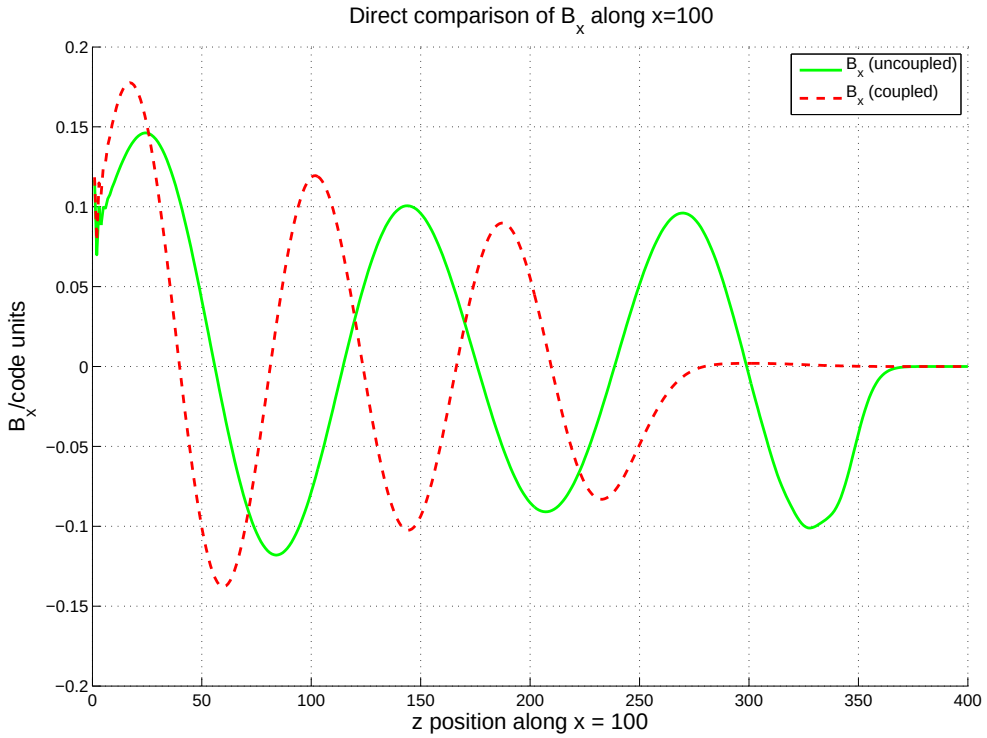

Figure 3.5: This plot shows the difference in the dominant wave mode (with a wave vector component only in the z-direction) brought about just by momentum coupling the plasma and neutrals together. CF53 assumes the magnetic evolution happens at the Alfvén speed but this isn't the case in the momentum-coupled mixture studied here. Predominantly the magnetic structure evolves at a speed 25% slower than the Alfvén speed. The CF53 method could be slightly modified to take this into account and also account for the fact that dispersive magnetosonic modes propagate at different speeds in different directions, eliminating systematic errors that might arise from assuming the speed is greater, or indeed less, than it actually is.

timestep that b_z perturbations are first detected at the same point ($x = 100$, $z = 300$) can be recorded as an indication of the speed of propagation of longitudinal magnetic perturbations. Results showing the propagation speeds for magnetic perturbations in both directions are presented below.

Recall that the control parameters of the simulations are r and s, which are the plasma sound speed and neutral gas sound speed respectively, normalised to some initial Alfvén speed. The third characteristic parameter is u, which is the plasma Alfvén

speed normalised to the same initial Alfvén speed, i.e. $u = 1$ for most static (i.e. homogeneous) cases. The parameters r and s act as handles to effectively alter the plasma and neutral gas densities. Varying u can be interpreted as changing the plasma density or the background magnetic field. On each of figures 3.6 and 3.7, the bold line $y = 1$ shows the normalising Alfvén speed: i.e. it shows the propagation speed for a driven Alfvén wave in an uncoupled plasma in which the sound speed is equal to the Alfvén speed.

Figures 3.6 and 3.7 show the results of several simulations. The four subplots in figure 3.6 show the change in transverse and longitudinal magnetic propagation speeds for a range of parameter s, for four fixed values of r. Effectively each subplot shows the effect of adding more neutral gas in to a mixture. The plasma density is fixed, with two subplots showing two cases of magnetically-dominated plasma ($r < u$), one hydrostatically-dominated ($r > u$), and one balanced ($r = u$). Figure 3.7 shows the same parameter range, but with s fixed and r varying. This shows the effect of adding more plasma into a mixture with constant neutral gas density, while increasing the background magnetic field accordingly.

It can be seen in all but one subplot that increasing the neutral gas density results in a linear increase in longitudinal velocity. This shows that the neutral gas density plays an active role in the dominant longitudinal wave mode in each case, contributing via the plasma-neutral momentum coupling in the cases dominated by plasma sonic or magnetosonic modes. The transverse velocity is a little more complicated. In all but the most hydrostatically-dominated cases, there is a discontinuity in the otherwise monotonic trend. Most of these discontinuities are accompanied by a noticeable change in gradient, for those cases with approximately linear dependence on the input variable parameter. An interpretation of this is that there is a possible switchover from transverse wave mode dominance affecting the transverse magnetic field (B_x perturbations) which happens at a tipping point near where the mixture becomes hydrostatically dominated. Longitudinal wave modes may have non-zero wave vector components in the x- *and* z-directions, unlike transverse waves which are confined to x-perturbations

only. It could be that the shift in dependence shown in six of the eight subplots in the two figures is caused by a change to the dominant source of B_x perturbations i.e. after the gradient switch, it is fast-moving diagonal longitudinal wave modes contributing to the perturbations rather than transverse modes only.

3.3 Comparing the Effect of Coupling on Neutral Sound Waves

Figures 3.8 and 3.9 show, for an incident sound wave in the neutral gas with a cosine envelope, a snapshot of the x-velocity and x-magnetic field along the line $x = 100$ in the domain for two cases. These figures show a 1-dimensional slices in the z-direction through figures 2.28 and 2.30. This represents a view of the plane perpendicular to the observer's line of sight. Figure 3.8 shows the results for a mixture composed of equal parts plasma and neutral gas (i.e. $r = s = 1$), but crucially there is no momentum coupling between the plasma and neutral gas. Figure 3.9 shows the results for identical initial conditions, but taking into account the momentum coupling between the two populations.

In both figures, the dashed green line shows the magnitude of the magnetic perturbation in the x-direcion and the solid blue line shows the magnitude of the plasma x-velocity. For completeness, the dashed blue line shows the magnitude of the neutral gas x-velocity.

3.3.1 Neutral Sound Waves Generating Magnetic Perturbations

A direct coupling on/off comparison showing the indirect magnetic influence of the neutral gas is shown in figure 3.10. With no momentum coupling (green line) between the plasma and neutral gas, perturbing the neutral population has no magnetic effect. However, when the populations are coupled, movement of the neutral gas causes the plasma to move with it, resulting in a non-zero plasma velocity field that induces an

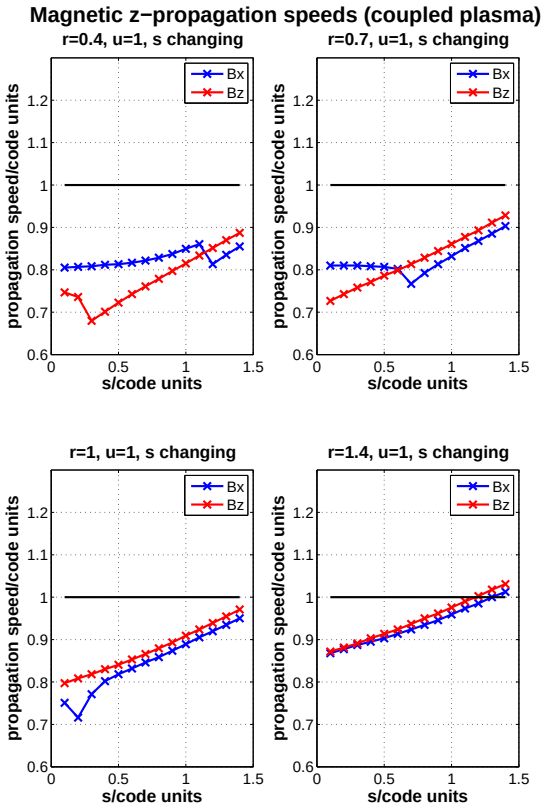

Figure 3.6: The change in transverse and longitudinal magnetic propagation speeds for a range of parameter s between 0.1 and 1.4, for four fixed values of r. The blue points show the magnetic perturbations in the x-direction, while the red points show the z-perturbations. Perturbations in the z-direction can only be provided by longitudinal wave modes, while x-perturbations are primarily caused by transverse wave modes but could also have a longitudinal mode contribution. The discontinuity in the B_x dependence is interpreted as a possible indication that the dominant contribution to B_x perturbations comes from longitudinal modes with components in both directions while the mixture is hydrostatically-dominated (i.e. when $r > 1$ and $s > 1$). B_z is not usually discontinuous because it contributions to it are always hydrostatically-dominated, except in the very low-density cases where the Alfvén speed dominates both sound speeds. See section 3.2.4 for a detailed explanation of this interpretation.

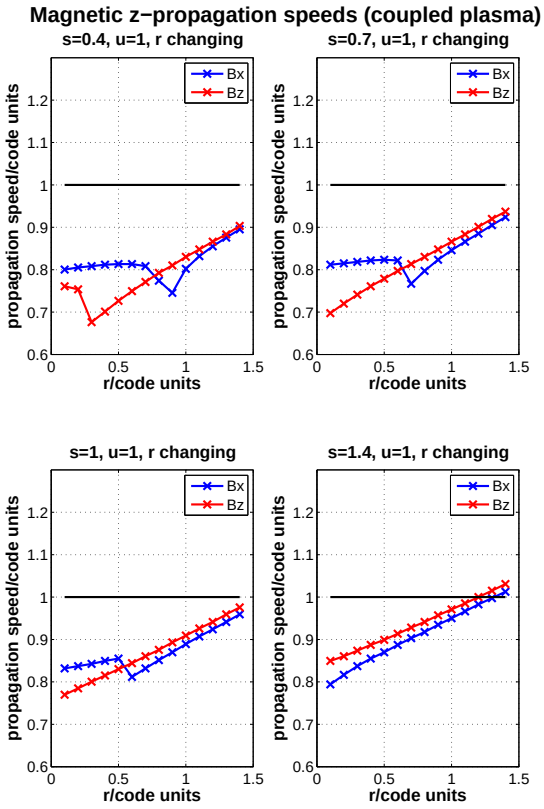

Figure 3.7: The change in transverse and longitudinal magnetic propagation speeds for a range of parameter r between 0.1 and 1.4, for four fixed values of s. The blue points show the magnetic perturbations in the x-direction, while the red points show the z-perturbations. Perturbations in the z-direction can only be provided by longitudinal wave modes, while x-perturbations are primarily caused by transverse wave modes but could also have a longitudinal mode contribution. The discontinuity in the B_x dependence is interpreted as a possible indication that the dominant contribution to B_x perturbations comes from longitudinal modes with components in both directions while the mixture is hydrostatically-dominated (i.e. when $r > 1$ and $s > 1$). i.e. to the left of the discontinuity, the dominant B_x contribution comes from the transverse Alfvén mode, but once the mixture becomes hydrostatically dominated the main contribution to B_x comes from compressional waves. See section 3.2.4 for a detailed explanation of this interpretation.

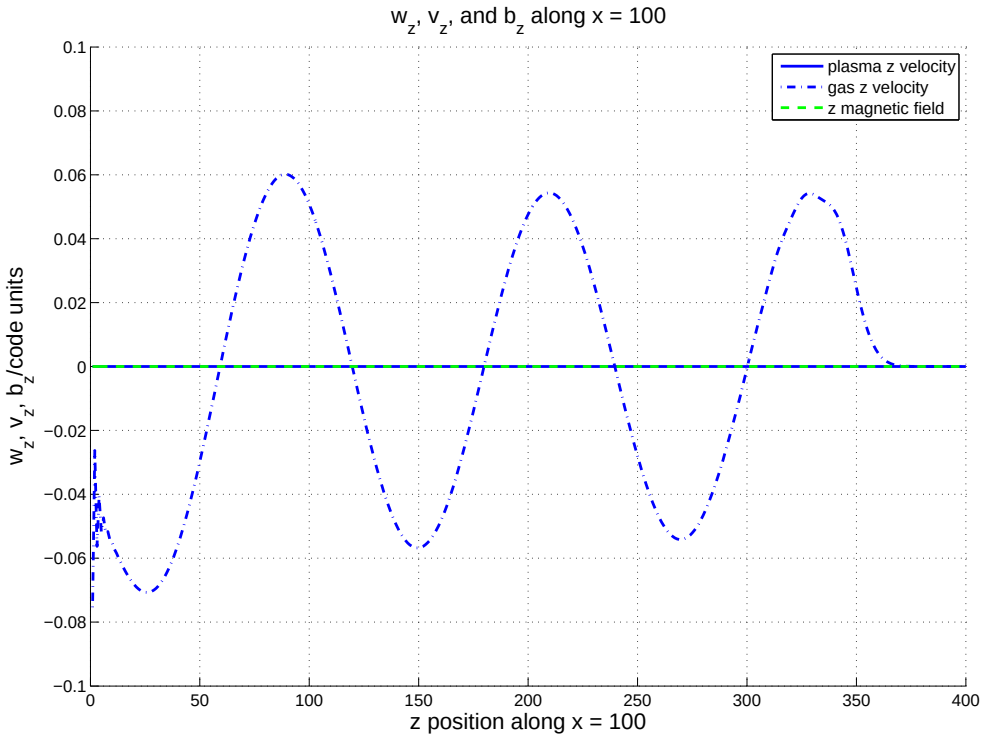

Figure 3.8: This plot shows a 1D slice along the line $x = 100$ in figure 2.28 - i.e. this is the plasma x-velocity, neutral x-velocity and the magnetic field perturbation (in the x-direction). The driving perturbation in this simulation was a sound wave in the neutral gas. The plasma velocity and magnetic perturbation are zero because there is no momentum coupling between the plasma and neutral populations.

associated magnetic perturbation (red line on the plot).

3.4 Discussion

One approach used in the literature (discussed in section 3.1.3) for refining the CF53 method is to compare "expected" polarisation dispersion from MHD turbulence simulations with the observed data. However, these simulations make the same assumptions about the plasma-neutral interaction that CF53 makes. A particular form of turbulent power spectrum is assumed for the neutral gas motion, and the data is interpreted as in CF53, i.e. that any neutral gas motion aligned with the plasma motion is coinciden-

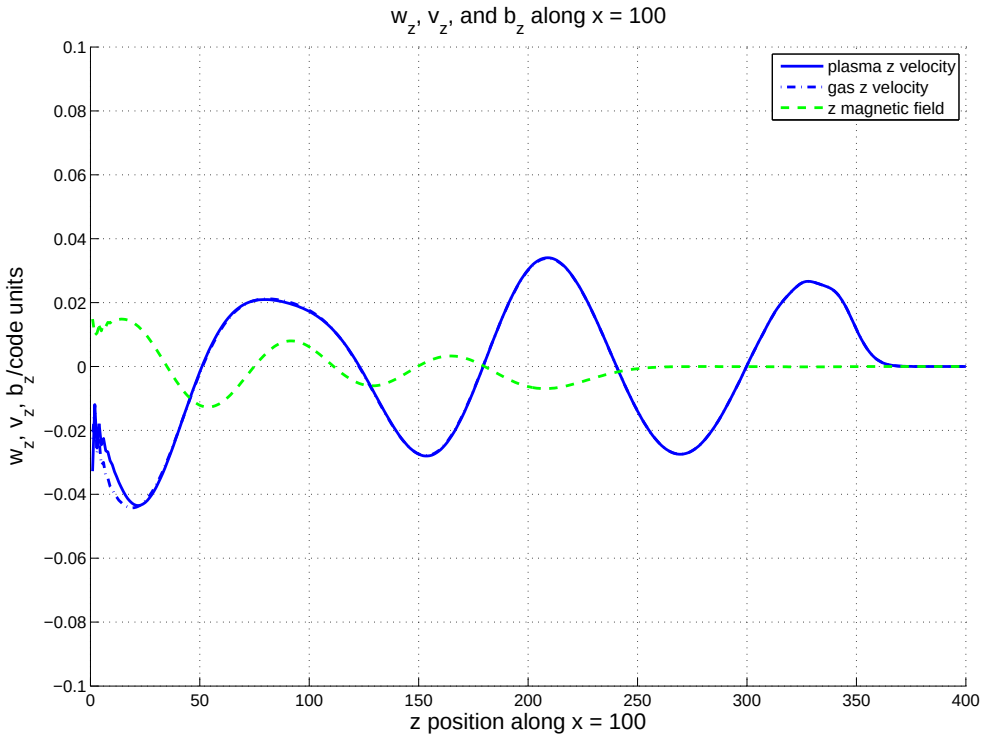

Figure 3.9: This plot also shows a 1D slice along the line $x = 100$, this time in figure 2.30. This plot is for identical initial conditions to figure 3.8, the only difference is that the coupling between the plasma and neutral populations was taken into account. Now a response is forced in the plasma population, as the moving neutral gas collides with it and drags it along. The moving plasma causes magnetic perturbations. It is through only the plasma-neutral interaction that an initially neutral process can produce such a magnetic response.

tal and, therefore, neutral gas motion in other directions can be ignored as incoherent motion. In fact, as has been shown above, that kind of analysis will result in inaccurate results for the background magnetic field, because the combined response of the plasma-neutral mixture is more complicated than expected. Figures 3.1, 3.2 and 3.5 show the change in wavelength and wave speed when a population of neutral gas is added to the plasma. Figures 3.6 and 3.7 show the relationship between the density of plasma and neutral gas and the magnetic evolution speed: the dominant wave modes almost always have a propagation speed of less than the expected Alfvén speed. Figures 3.3 and 3.4 show that the equipartition of energy assumption needs to be carefully

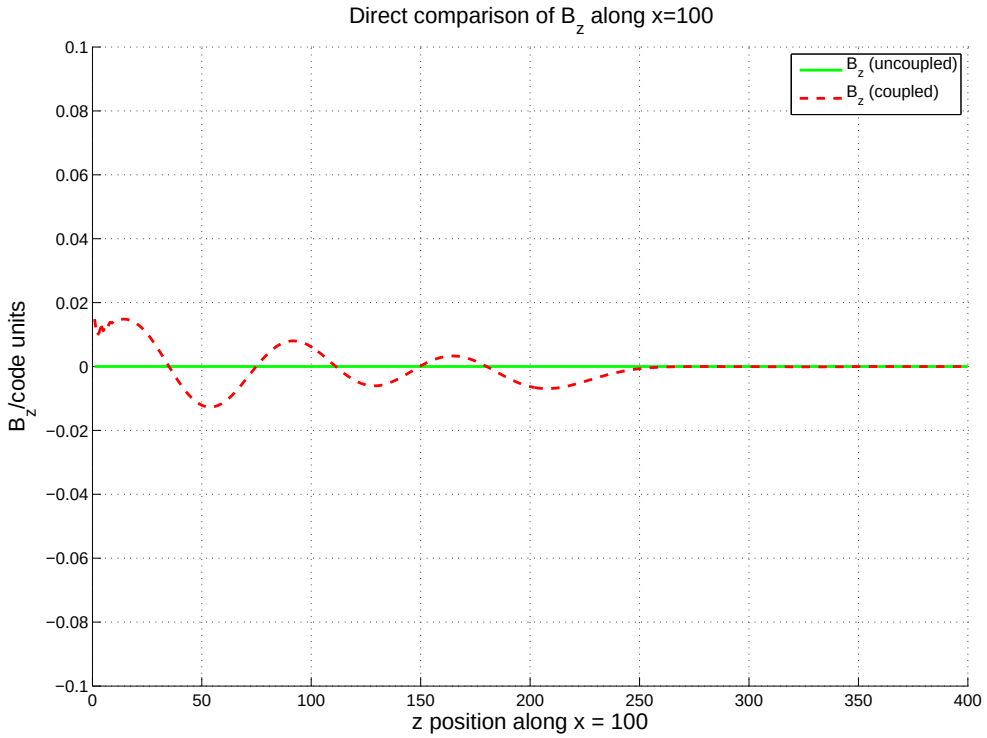

Figure 3.10: A direct comparison between momentum coupling on and off shows that the plasma-neutral interaction is responsible for magnetic perturbations induced indirectly by sound waves in the neutral gas. The combined response of the plasma-neutral mixture induces a non-zero curl in the magnetic field of the plasma.

handled.

At the beginning of this chapter, three issues with the Chandrasekhar-Fermi method were highlighted:

1. It is assumed in CF53 that the speed of any wave excited in the plasma-neutral mixture is equal to the Alfvén speed, i.e. that the wave is just a transverse Alfvén wave. However, this is not the case; the combined response is not a pure mode of either medium. This means the assumption that the magnetic structure evolves at the Alfvén speed may not be a good one, especially since the propagation speed varies with direction.

2. CF53 assumes that the neutral gas contribution to the observed velocity disper-

sion is only due to turbulent, incoherent motion. In the fluid limit, the random motion is assumed to be averaged out over the bulk behaviour. In this limit, the neutral gas and plasma are entrained in a mutually coherent response. This might actually clarify the interpretation of Doppler velocity measurements, since if it can be assumed that the plasma and neutral gas are moving together then separating the motions is not an issue.

3. Finally, the averaging of the polarisation dispersion may need to be revised to take into account the superposition of wave modes and the different influence that each mode has on the magnetic field perturbations. For example, there are longitudinal magnetic perturbations which would not be generated without the plasma-neutral interaction. Assuming that only a transverse Alfvén wave caused the magnetic structure could lead to inaccurate results.

Simulations modelling the plasma-neutral interaction *ab initio*, as opposed to assuming zero plasma motion but a particular turbulent form for the neutral gas, have highlighted all three issues. Figures 3.1, 3.2 and 3.5 show that the magnetic perturbations induced by the combined response is in fact unlikely to propagate at the Alfvén speed, and depending on the ionisation fraction of the plasma the actual propagation speed will be slower[2]. All figures in this chapter show that the neutral gas, rather than moving incoherently and minding its own business, actually moves coherently along with coherent plasma motion.

Finally, the fact that a perturbation to the neutral gas can indirectly induce magnetic field perturbations via the plasma, as shown in figures 3.8- 3.10 is potentially important. This could have an impact on the third item in the list above, contradicting the assumption that magnetic perturbations are generated *only* by transverse Alfvén wave modes, although this is a small effect.

However, small effect or not, the induction of magnetic perturbations by neutral sound waves could be significant, especially in the context of stellar or large scale

[2]or possibly faster in some cases

structure formation: even a magnetic field of tiny magnitude could have an influence over the exact dynamics of gravitational collapse. This effect could also contribute to the development of persistent magnetic fields in the early post-decoupling Universe. Many theories postulate that large-scale magnetic fields observed today at galaxy or even at galaxy cluster scale grew from very small magnitude "seed" fields, but it remains a major challenge of astrophysics to find both a viable theory and observational evidence for this. It is possible that the effect of sound waves inducing magnetic perturbations seen in the simulations here could have some application towards that discussion. Another implication of this is the fact that while Alfvén waves are stable[3], magnetosonic modes are compressional and therefore can become unstable: if their amplitude becomes too large, shocks can form or the waves can break. Even though the simulations presented here are linear, they show that magnetosonic modes are unavoidable. In a higher-order simulation with turbulence, compressional mode instability could become significant.

The model presented here is linear, and as such the parameter range covered by it may not include examples expected of certain real-life astrophysical plasmas. Rather, this study is intended to motivate a more detailed investigation of the issues highlighted here, and to encourage more careful consideration of the assumptions employed in the interpretation of data, especially polarisation data, for the purposes of astrophysical magnetic field diagnostics. Results presented here show the impact of neutral gas with a ratio of density to plasma density of ten to one: consider the trends demonstrated e.g. in figures 3.6 and 3.7 of the change in propagation speed of magnetic perturbations caused by increasing the density proportion of neutral gas. Consider the differences between figures 2.16 -2.19 in the wave modes induced for small density ratios, and the magnetic perturbations shown in figures 2.28-2.31 that are induced by plasma motion as momentum is transferred from the neutral gas.

Realistic examples of ionisation fractions include:

[3]Unless the pressure balance is such that the firehose instability is implicated.

1. The interstellar medium[4] (ISM): Chemical abundance calculations put a lower limit on ionisation fraction of order 10^{-4}, though the average measured using pulsar dispersion data measured 10^{-2} [5].

2. The warm ionised medium (WIM) of the galaxy, i.e. the medium near stars, has been measured to have ionisation fractions of over 0.9.

3. HII regions, very hot galactic locations containing mostly ionised Hydrogen, are almost fully-ionised to within 1 part in 10^5.

For the example of the ISM, plasma with an ionisation fraction of 10^{-4} (in a single-element mixture, i.e. a neutral gas to plasma density ratio of 10^5 to 1) still behaves like a plasma, yet assuming as current analysis does that *only* transverse Alfvén waves propagate coherently neglects the considerable influence that the neutral gas can exert. The linear model presented in this thesis is capable of modelling ionisation fractions consistent with the WIM, and developing a more detailed model will allow the investigation of the more extreme parameter ranges discussed.

For actively and practically refining the CF53 method, the simulations detailed here pave the way for the next generation of simulations to compare observed data to. Simulating turbulence is missing the point. Applying the physics developed above, there will remain an uncertainty about the exact value of the magnetic field that is to be measured while the ionisation fraction of the plasma is unknown. The current CF53 equations should be treated as an approximation - i.e. as returning an estimate of magnetic field assuming that the observed magnetic structure evolves at the Alfvén speed. The true evolution speed is likely to be slower than this, but depending on the proportion of neutral gas it could actually be faster than the Alfvén speed. This uncertainty in the observed evolution speed is reflected in uncertainty in the diagnosed magnetic field. The refined version of the method outlined here will be able to provide upper and lower limits to the observed background magnetic field.

[4]For which Chandrasekhar and Fermi originally formulated their observational method.

[5]http://www.astronomy.ohio-state.edu/ pogge/Ast871/Notes/Intro.pdf

3.5 Summary

In this chapter refinements to the Chandrasekhar-Fermi observational method were tested. It was demonstrated that some of the current assumptions may have to be re-examined: the assumption of energy equipartition (figures 3.3- 3.4); the speed of magnetic evolution (figures 3.6 and 3.7); and the assumption that the neutral gas moves randomly and incoherently (figure 3.2, figure 3.9). The simulation results demonstrate possible future considerations which could be made, and also suggest a possible computational model for comparison to observation, in a similar way to what is already done with MHD turbulence simulations. The results from this linear model motivate more complex simulations capable of modelling all parameter ranges for comparison with observations.

"Baldrick, I would advise you to make the explanation you are about to give...
phenomenally good."

Edmund Blackadder

4

Computational Model of Particles and Fields

This chapter will develop the numerical model used to simulate the motion of charged particles accelerated by the transient electric and magnetic fields induced in a rapidly-evolving magnetised plasma. In particular, the model is designed to consider the effect that a decaying magnetic flux has on the acceleration of particles via the transient induced electric field. This is applicable to any magnetised plasma where recombination is a significant process, such as in pulsed devices, or in the decoupling era (also called the "epoch of recombination") of the early Universe. Since the residual charged-particle number density is small as a result of the recombination, the model will consider the magnetic and electric fields essentially to be imposed, neglecting the feedback from any minority accelerated population.

The purpose of the general model developed in this chapter is to provide simulations of the motion of charged particles in potentially unusual configurations of electric and magnetic fields. This chapter will derive the model equations and computational solutions, and as a test will also show some examples of charge motion solved by the model under simple field configurations. In chapter 5, much more complex electric and magnetic field configurations will be derived before the model is put to use in

predicting high-energy electrons accelerated by magnetic collapse during the epoch of recombination in the early Universe.

4.1 Deriving the Model Equations

The two-dimensional equations of motion for a charge moving under the influence of electric and magnetic fields are as follows, where $\mathbf{x} = (x, y)$ is the position vector, $\mathbf{v} = (v_x, v_y)$ is the velocity vector, t is the time, $\mathbf{E} = (E_x, E_y)$ and $\mathbf{B} = \hat{z}B_z$ are the electric and magnetic field vectors, and q_e and m_e are the particle charge and mass respectively.

$$\frac{dx}{dt} = v_x \tag{4.1}$$

$$\frac{dy}{dt} = v_y \tag{4.2}$$

$$\frac{dv_x}{dt} = \frac{q_e}{m_e}(E_x + v_y B_z) \tag{4.3}$$

$$\frac{dv_y}{dt} = \frac{q_e}{m_e}(E_y - v_x B_z) \tag{4.4}$$

These equations can be non-dimensionalised by splitting each of the variable parameters into a dimensional and a non-dimensional part. The substitutions are as follows:

$$x = x_0 \xi \tag{4.5}$$

$$y = x_0 \zeta \tag{4.6}$$

$$v_x = v_0 u_\xi \tag{4.7}$$

$$v_y = v_0 u_\zeta \tag{4.8}$$

$$t = t_0 \tau \tag{4.9}$$

$$E_x = E_0 e_\xi \tag{4.10}$$

$$E_y = E_0 e_\zeta \tag{4.11}$$

$$B_z = B_0 b \tag{4.12}$$

where e.g. ξ is the dimensionless scaling part of x which ranges, say, between zero and one, and x_0 is a dimensional factor, in this case the characteristic length of the physical

system. Substituting into equations 4.1- 4.4 and rearranging:

$$\frac{d\xi}{d\tau} = \frac{v_0 t_0}{x_0} u_\xi \tag{4.13}$$

$$\frac{d\zeta}{d\tau} = \frac{v_0 t_0}{x_0} u_\zeta \tag{4.14}$$

$$\frac{du_\xi}{d\tau} = \frac{q_e t_0 E_0}{m_e v_0} e_\xi + \frac{q_e B_0 t_0}{m_e} u_\zeta b \tag{4.15}$$

$$\frac{du_\zeta}{d\tau} = \frac{q_e t_0 E_0}{m_e v_0} e_\zeta + \frac{q_e B_0 t_0}{m_e} u_\xi b \tag{4.16}$$

Rewriting these equations slightly, three dimensionless control parameters emerge: P_1, P_2 and P_3.

$$\frac{d\xi}{d\tau} = P_1 u_\xi \tag{4.17}$$

$$\frac{d\zeta}{d\tau} = P_1 u_\zeta \tag{4.18}$$

$$\frac{du_\xi}{d\tau} = P_2 e_\xi + P_3 u_\zeta b \tag{4.19}$$

$$\frac{du_\zeta}{d\tau} = P_2 e_\zeta + P_3 u_\xi b \tag{4.20}$$

where

$$P_1 = \frac{v_0 t_0}{x_0} \tag{4.21}$$

$$P_2 = \frac{q_e E_0 t_0}{m_e v_0} \tag{4.22}$$

$$P_3 = \frac{q_e B_0 t_0}{m_e} \tag{4.23}$$

P_1 can be set to unity by identifying that the characteristic speed of the system v_0 is related to the characteristic length (x_0) and time (t_0) scales as follows:

$$v_0 = \frac{x_0}{t_0} \tag{4.24}$$

Simplifying further, P_3 can also be set to unity since the electron cyclotron period t_c (the time taken for an electron with mass m_e and charge q_e to execute one gyro-orbit in a magnetic field B_0) is given by

$$t_c = \frac{m_e}{q_e B_0} \tag{4.25}$$

Thus identifying the characteristic time t_0 to be equal to t_c, the system of equations reduces to the following:

$$\frac{d\xi}{d\tau} = u_\xi \tag{4.26}$$

$$\frac{d\zeta}{d\tau} = u_\zeta \tag{4.27}$$

$$\frac{du_\xi}{d\tau} = P_2 e_\xi + u_\zeta b \tag{4.28}$$

$$\frac{du_\zeta}{d\tau} = P_2 e_\zeta + u_\xi b \tag{4.29}$$

The free parameter P_2 is only partly constrained by the choice of $P_1 = P_3 = 1$. P_2 can be set to unity as well, in the first instance, and changed to study different parameter choices.

4.2 The Runge-Kutta Solver

These model equations were solved numerically using a 4th-order Runge-Kutta method (Press et al. 1992). This is an iterative numerical technique which closely approximates exact solutions to systems of differential equations. Runge-Kutta (RK) methods basically match the first n terms of the Taylor series expansion to the function that is the solution, where n is the order required for the solution. The technique is such that low order errors cancel each other out, meaning that for the fourth order method, each step h has an error of order $O(h^5)$. The overall solutions are accurate to $O(h^4)$.

The RK method can be illustrated as follows. Consider a simple example of an ordinary differential equation of the form

$$\frac{dy}{dx} = f(x, y) \tag{4.30}$$

where f is some arbitrary, well-behaved function of x and $y(x)$, with the initial values $x = x_0$ and $y(x_0) = y_0$ specified in the problem. Then one fourth-order Runge-Kutta method for finding iterative solutions is the following:

$$y_{n+1} = y_n + \frac{1}{6}(k_1 + 2k_2 + 2k_3 + k_4) \tag{4.31}$$

$$\begin{aligned} \text{where } k_1 &= hf(x_n, y_n) \\ k_2 &= hf(x_n + \frac{h}{2}, y_n + \frac{k_1}{2}) \\ k_3 &= hf(x_n + \frac{h}{2}, y_n + \frac{k_2}{2}) \\ k_4 &= hf(x_n + h, y_n + k_3) \end{aligned} \tag{4.32}$$

where h is the step size of each numerical iteration, x_n is the value of the input variable x at each step n, and y_n denotes the value of function y at step n ($y_n = y(x_n)$). Starting with the boundary values at $n = 0$, the solution cascades forwards as the method is applied at each step, and eventually the numerical solutions for all steps y_n are computed.

Runge-Kutta and Systems of ODEs

In this case numerical solutions are required for each timestep of a system of four equations, i.e. the dimensionless charged particle equations of motion shown in equations 4.26 - 4.29. Expressed in the form of equation 4.30 these equations are

$$\frac{d\xi}{d\tau}(\tau, \xi) = u_\xi(\tau) \tag{4.33}$$

$$\frac{d\zeta}{d\tau}(\tau, \zeta) = u_\zeta(\tau) \tag{4.34}$$

$$\frac{du_\xi}{d\tau}(\tau, u_\xi) = P_2 e_\xi(\tau, \xi, \zeta) + u_\zeta(\tau) b(\tau, \xi, \zeta) \tag{4.35}$$

$$\frac{du_\zeta}{d\tau}(\tau, u_\zeta) = P_2 e_\zeta(\tau, \xi, \zeta) + u_\xi(\tau) b(\tau, \xi, \zeta) \tag{4.36}$$

where $(\xi(\tau),\ \zeta(\tau))$ is the particle position, $(u_\xi(\tau),\ u_\zeta(\tau))$ are the components of velocity in each direction. $e(\tau, \xi, \zeta)$ is the electric field and $b(\tau, \xi, \zeta)$ is the magnetic field; both are functions of the two-dimensional position and time. At each iterative step n during the Runge-Kutta solution, these four derivative equations are called several times during the calculation of the $(n + 1)$-th step. For example, given the initial conditions ξ_0, ζ_0, $u_{\xi,0}$, $u_{\zeta,0}$ the solutions ξ_n for all n can be found using the iteration:

$$\xi_{n+1} = \xi_n + \frac{1}{6}(k_1 + 2k_2 + 2k_3 + k_4) \tag{4.37}$$

$$
\begin{aligned}
\text{where } k_1 &= h\frac{d\xi}{d\tau}\left(\tau_n + \frac{h}{2},\, \xi_n + \frac{h}{2}\frac{d\xi}{d\tau}(\tau_n, \xi_n)\right) \\
k_2 &= h\frac{d\xi}{d\tau}\left(\tau_n + \frac{h}{2},\, \xi_n + \frac{1}{2}k_1\right) \\
k_3 &= h\frac{d\xi}{d\tau}\left(\tau_n + \frac{h}{2},\, \xi_n + \frac{1}{2}k_2\right) \\
k_4 &= h\frac{d\xi}{d\tau}\left(\tau_n + h,\, \xi_n + k_3\right)
\end{aligned}
$$

The step size h is the step between τ_n and τ_{n+1}.

The functions $e(\tau, \xi, \zeta)$ and $b(\tau, \xi, \zeta)$ in equation array 4.33 for electric and magnetic field are specified depending on the problem at hand. They could have a very simple form as for the test cases below in section 4.3, or they could be very complex such as in the detailed study in chapter 5. There is scope to extend the model by defining the functions to take account of the position and velocity of charges, meaning it would become a fully self-consistent plasma model, but this would dramatically increase the computational workload and will be an interesting part of the future development of this work.

4.2.1 The Algorithm

A code was written in FORTRAN-77 for solving the system of equations with the following structure:

1. Using the analytic forms (equations 5.41 and 5.42), construct lookup tables that contain the electric and magnetic field values for each spatial position.

2. Establish the initial conditions (in this case the initial position and velocity of each particle).

3. Calculate the electric and magnetic field at the position of each particle using the lookup tables.

4. Apply Runge-Kutta method to the model equations to find the particle positions and velocities at the next timestep.

5. Update the initial conditions to instead hold the solutions for this step at the start of the next loop.

6. Go to step 3.

7. Continue looping until all values for the desired range of timesteps have been solved for.

The results for particle position and velocity and values of the electric and magnetic fields were periodically written to file. The analytic forms of the electric and magnetic fields were passed to the code at the start. Since it would be computationally inefficient to analytically compute the field values multiple times per timestep, lookup tables were calculated during initialisation. The tables held $1,000$ discretised values for the spatial positions of each field, meaning the only calculation required during step 3 was the linear interpolation[1] between table values. The time variation was obviously taken into account at each timestep, and again used field forms that had been solved for analytically before computation.

Since the code considered electric and magnetic fields imposed from the current density decay that were many orders of magnitude higher than the self-fields induced by electrons moving with 10keV kinetic energy, the fields from moving particles are neglected for now. This is consistent with the test-particle concept. This will be discussed in more detail in the next chapter.

4.3 Test Study of the Solver

As a test, the code evolved the dynamics of a single electron in imposed electric and magnetic fields. Several simple configurations were studied to make sure the simulations worked as expected, before the full solutions were implemented. In all cases,

[1] In the cases studied here, the linear interpolation was a good approximation since the spatial variation was slow. For more spatially-structured cases the interpolation could easily be changed to higher order.

fields constant in time were applied to a single electron. In all cases, the electron behaved exactly as expected.

4.3.1 Constant z-Magnetic Field, Zero Electric Field

This simplest possible case considered an electron moving in the x-y plane with non-zero initial velocity in the y-direction only encountering a uniform magnetic field with a non-zero component in the z-direction only. In the non-dimensional form of equations 4.35 and 4.36 the electron equations of motion are:

$$\frac{du_\xi}{d\tau} = u_\zeta b \tag{4.38}$$

$$\frac{du_\zeta}{d\tau} = -u_\xi b \tag{4.39}$$

Rearranging and taking the time derivative (where now a dot above a quantity represents the derivative $d/d\tau$):

$$\ddot{u}_\xi = -b^2 u_\xi \tag{4.40}$$

$$\ddot{u}_\zeta = -b^2 u_\zeta \tag{4.41}$$

In the units the electron cyclotron frequency is $\omega_c = b$, meaning solutions to these equations are given by

$$u_\xi(\tau) = A_1 \cos\omega_c\tau + B_1 \sin\omega_c\tau \tag{4.42}$$

$$u_\zeta(\tau) = A_2 \cos\omega_c\tau + B_2 \sin\omega_c\tau \tag{4.43}$$

Applying the initial conditions $u_\zeta = u_0$, $u_\xi = 0$ at time $\tau = 0$, we find that the coefficients are $A_1 = 0$, $B_1 = u_0$, $A_2 = u_0$, and $B_2 = 0$:

$$u_\xi(\tau) = u_0 \sin\omega_c\tau \tag{4.44}$$

$$u_\zeta(\tau) = u_0 \cos\omega_c\tau \tag{4.45}$$

These equations describe circular motion, i.e. the electron gyro motion in the magnetic field. Figure 4.1 shows the results of the simple simulation for this case. The velocity

plots show clearly that the initial velocity u_0 was equal to 1. Note that for easy comparison, the axes of the three velocity plots as well as the x-position plot are identical to the axes of the same plots in figure 4.2.

4.3.2 Constant z-Magnetic Field, Non-zero x-Electric Field

Now consider a second well-understood situation: an electron moving in crossed electric and magnetic fields. Consider a constant, uniform electric field in the x-direction and constant, uniform magnetic field in the z-direction.

$$\frac{du_\xi}{d\tau} = e_\xi + u_\zeta b \tag{4.46}$$

$$\frac{du_\zeta}{d\tau} = -u_\xi b \tag{4.47}$$

where the form of equations 4.35 and 4.36 is used again, and the parameter P_2 in equation 4.35 is set equal to unity. Rearranging and taking the time derivative:

$$\ddot{u}_\xi = -b^2 u_\xi \tag{4.48}$$

$$\ddot{u}_\zeta = -b^2\left(u_\zeta - \frac{e}{b}\right) \tag{4.49}$$

The electron cyclotron frequency is $\omega_c = b$ in these units, and we define a drift speed $u_D = e/b$ so that

$$\ddot{u}_\xi = -\omega_c^2 u_\xi \tag{4.50}$$

$$\ddot{u}_\zeta = -\omega_c^2(u_\zeta + u_D) \tag{4.51}$$

solutions to these equations are given by

$$u_\xi(\tau) = A_1 \cos\omega_c\tau + B_1 \sin\omega_c\tau \tag{4.52}$$

$$u_\zeta(\tau) = A_2 \cos\omega_c\tau + B_2 \sin\omega_c\tau - u_D \tag{4.53}$$

Applying the same initial conditions as in the previous example: $u_\zeta = u_0$, $u_\xi = 0$ at time $\tau = 0$, we find that the coefficients are $A_1 = 0$, $B_1 = u_0$, $A_2 = u_0 + u_D$, and $B_2 = 0$,

meaning the solutions are

$$u_{\xi}(\tau) = u_0 \sin \omega_c \tau \tag{4.54}$$

$$u_{\zeta}(\tau) = (u_0 + u_D) \sin \omega_c \tau - u_D \tag{4.55}$$

So the electron is accelerated by the electric field, and orbits in the magnetic field in gyro motion. Meanwhile the guiding centre drifts in the direction perpendicular to both the electric and magnetic field, i.e. in the y-direction[2]. Simulation results for this case are shown in figure 4.2.

4.3.3 Collapsing z-Magnetic Field

As a final pathway to the full problem, it is instructive to show the case of a constant uniform axial (z-) magnetic field decaying exponentially in magnitude. The electromagnetic response to such an example will be fully derived in chapter 5 and results in an azimuthal[3] electric field being induced. Since the magnetic field is forced to decay exponentially by imposing such a decay on the current density sustaining it, the induced electric field also decays exponentially at the same rate. The equations are solved in detail in chapter 5.

Analysing the equations of motion predicts a very similar result to the previous example, i.e. gyro motion with a guiding-centre drift. In fact, mathematically the only difference from the previous case is a coordinate transform. By the usual sign conventions we expect the electron to drift radially outwards from the starting point (1,1). Figure 4.3 shows that this is indeed the case.

4.3.4 Energy Conservation

A crucial requirement of any computational work is that the simulations obey the law of energy conservation. Figure 4.4 shows the change in total energy[4] of an electron

[2] In this example the drift is in the negative y-direction.

[3] ϕ-direction, i.e. with components in both the x- and y-directions

[4] Kinetic energy plus potential energy.

moving in crossed electric and magnetic fields, the exact electron shown earlier in figure 4.2.

This was calculated by considering the equation for the scalar field electric potential V, which is related to the electric field $\mathbf{e}$ in dimensionless code units as follows:

$$\mathbf{e} = -\nabla V \tag{4.56}$$

Since the case described in section 4.3.2 has a uniform non-zero component of electric field only in the ξ-direction, equation 4.56 simplifies to

$$e_\xi = -\frac{dV}{d\xi} \tag{4.57}$$

The electron potential energy U is related to the electric potential by:

$$U = q_e V \tag{4.58}$$

where q_e is the electron charge. In dimensionless code units (i.e. scaling out the constant q_e), equations 4.56 and 4.58 combine to find

$$\frac{dU}{d\xi} = -e_\xi \tag{4.59}$$

Since the electric field is uniform and constant, as a function of time the change in potential energy δU for a small change in electron ξ-position $\delta\xi$ can be calculated as follows:

$$\delta U(\tau) = -e_\xi \delta\xi(\tau) \tag{4.60}$$

Therefore at each timestep the difference in potential energy between the electron's current position and its position at the previous timestep could be calculated.

The change in kinetic energy δK as a function of time for small changes in velocity δu_ξ and δu_ζ (also functions of time), scaled in dimensionless code units, is calculated by

$$\delta K(\tau) = \frac{1}{2}\left(\delta u_\xi(\tau)^2 + \delta u_\zeta(\tau)^2\right) \tag{4.61}$$

Figure 4.4 shows the plot of the sum $\delta K + \delta U$ for each timestep. Each point on the plot shows the change in total energy compared to the previous timestep. Energy is conserved to within rounding errors, indicating that the simulations are working as required.

4.4 Discussion

This chapter developed the computational model for solving the motion of charged particles under the influence of imposed arbitrary electric and magnetic fields. A Runge-Kutta solver method was used to numerically solve the system of equations of motion. Figures 4.1, 4.2 and 4.3 show three test studies of the solver which are consistent with theoretical predictions, confirming its accuracy. Figure 4.4 shows that energy is conserved by the solver. The purpose of the model is to allow scope for the study of much more complex configurations of electric and magnetic fields. This will be exploited in the next chapter, where a transient case with rapidly-changing fields which has particular relevance to an interesting cosmological problem will be considered.

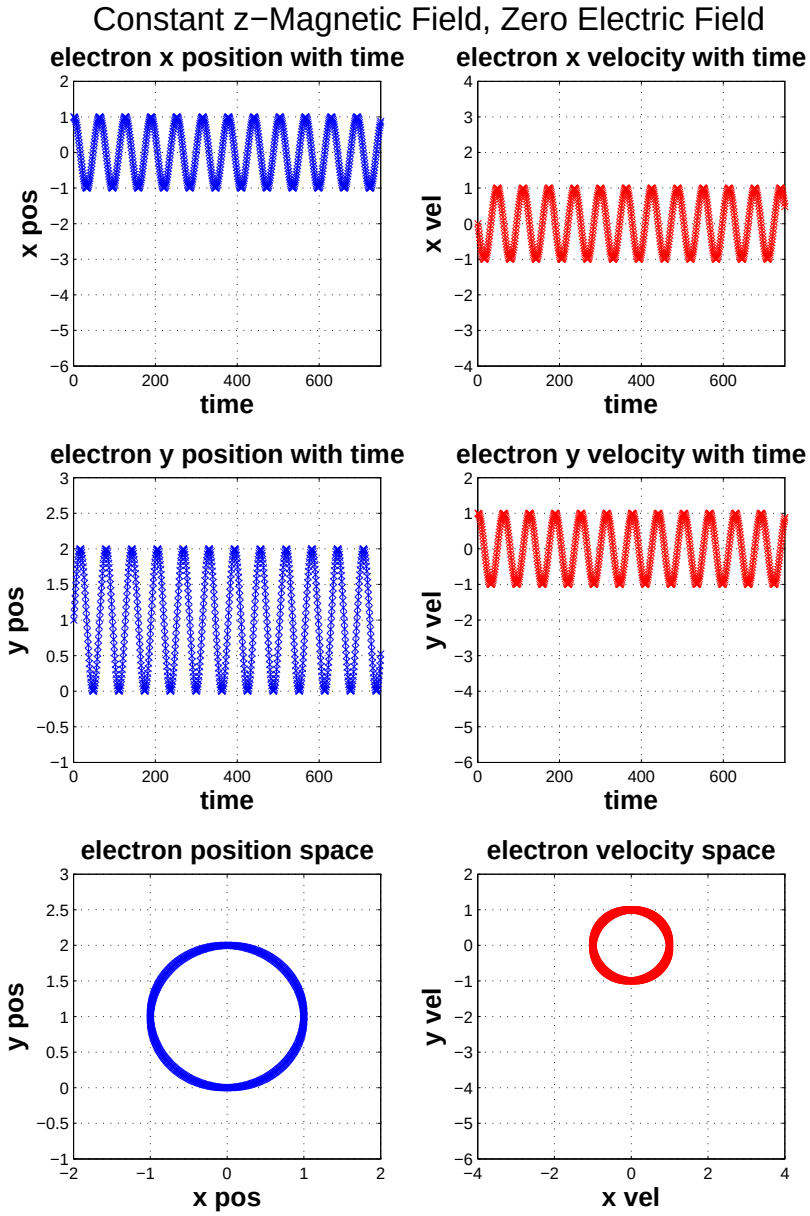

Figure 4.1: Solver test of a single electron with starting position (1,1) and initial velocity (0,1) moving in a uniform constant magnetic field. The left subplots show the electron position data, with the top two plots depicting the x- and y-positions as a function of time and the bottom plot showing the entire position space. The right hand subplots show the velocity data in the same arrangement. The motion in both dimensions is simple harmonic, characteristic of a gyro orbit centred on the plot origin, and the position and velocity space plots confirm that the electron moves in a circular orbit as described by equations 4.44 and 4.45.

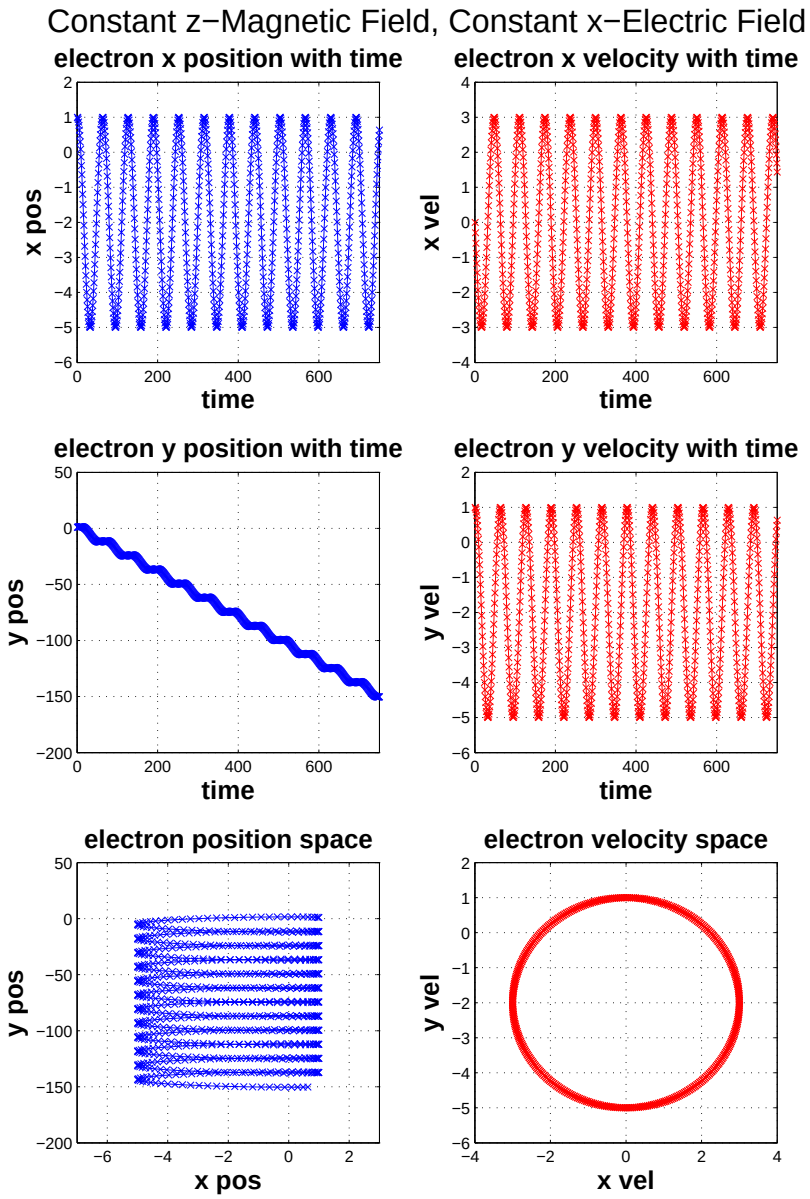

Figure 4.2: Simulation test of a single electron with starting position (1,1) and initial velocity (0,1) moving in constant, uniform, crossed electric (magnitude = 2) and magnetic (magnitude = 1) fields. The magnetic field points out of the page, while the electric field points in the positive x-direction. The left subplots show the electron position data, with the top two plots depicting the x- and y-positions as a function of time and the bottom plot showing the entire position space. The right hand subplots show the velocity data in the same arrangement. The motion is simple harmonic, with a component of drift in the y-direction. The drift component has magnitude 2, consistent with the $E \times B$ drift speed derived in chapter 1, and is well understood from the equations of motion. Notice that for comparison the plot axes of the three velocity plots and the x-position plot are identical to those of figure 4.1.

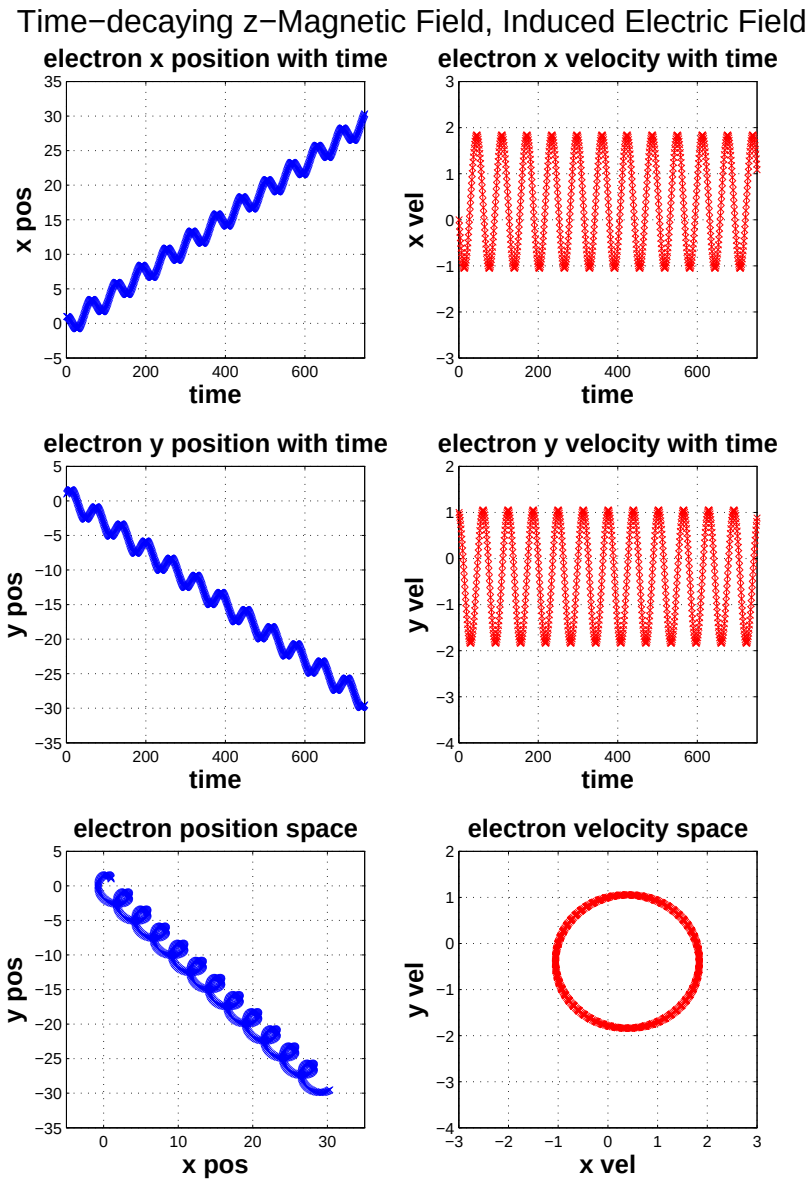

Figure 4.3: Final simulation test example, showing the motion of a test electron with starting position (1,1) and initial velocity (0,1) in a collapsing magnetic field. The magnetic field was uniform and decreased in magnitude exponentially, inducing an electromagnetic response in the form of an azimuthal electric field. This resulted in the electron acquiring an $E \times B$ drift radially outwards, as seen clearly in the position space subplot. Note that although B is decaying exponentially, the magnitude of E *also* decays at the same rate, meaning the drift velocity is constant.

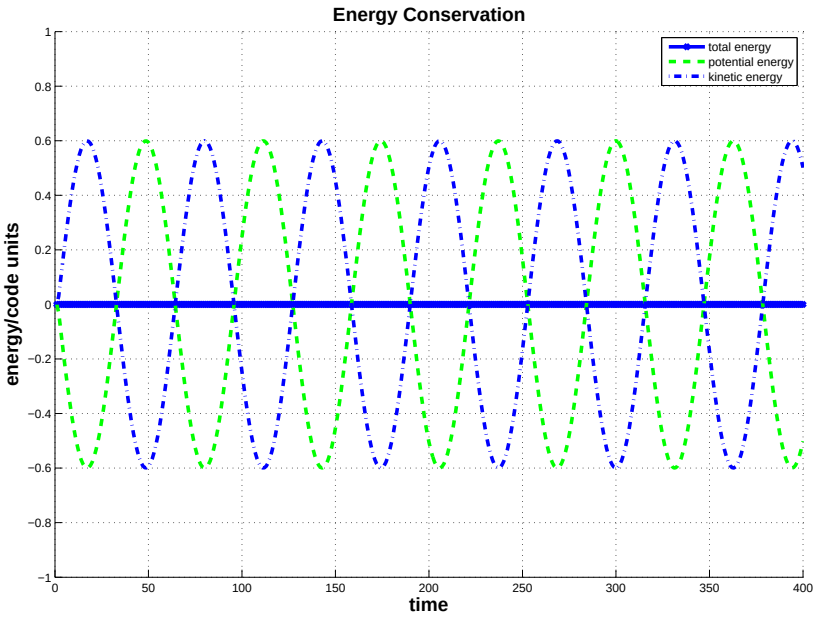

Figure 4.4: The total of the change in kinetic energy and potential energy of an electron moving in crossed electric and magnetic fields, exactly as for figure 4.2. Each point shows the total energy difference between the current timestep and the previous timestep. All points are zero to within small rounding errors.

"Well, my time of not taking you seriously is certainly coming to a middle."

Malcolm Reynolds

5

Magnetic Collapse at the Epoch of Recombination

This chapter will seek to address an often-overlooked question related to the early Universe; what happens to an inhomogeneously-magnetised plasma when it is rapidly neutralised? The setting for this question is primarily during the cosmological epoch of recombination, but it also has relevance to terrestrial plasmas such as those found in pulsed devices or the cooler edge regions of tokamaks.

5.1 Unplugging the Universe

In this chapter the model first developed by Diver and Teodoro (2008) will be expanded, using the theoretical magnetic structures described in section 1.3.2. To recap: if the Universe did indeed contain large-scale coherent magnetic fields before the recombination era, then it must have been pseudo-stochastically arranged such that the total field summed to zero (Moffatt 1978; Rusbridge 1991; Ichiki et al. 2006; Durrer 2007). This assumption preserves the cosmological principles of isotropy and homogeneity, i.e. that there can be no preferred direction and no "special places" in the Universe. Therefore it is reasonable to assume that if large-scale magnetic fields did exist at this epoch, the Universe was divided into magnetic *domains*, each coherent and

with different direction. The boundary between domains must have been provided by conduction currents in the high-conductivity plasma, although this would change after the start of global recombination.

The question is: what happens to these magnetic domains as the Universe undergoes the phase change during decoupling, from fully-ionised to just 1 part in 10^5 ionised (Padmanabhan 1993). The large-scale neutralisation will remove charges from the current-carrying parts of the plasma (as it does globally from the entire plasma), causing the conduction current density to decrease, meaning the magnetic field sustained by the conduction current will also decrease. During such a transition, the displacement current asserts itself to restore the balance and sustain the magnetic field structure, according to Lenz's law. The energy stored in the magnetic field has to go somewhere, and accordingly the time-varying electric field of the displacement current acts to transfer this energy by accelerating any remaining free charges[1]. This electric field perturbation, accompanied by a small magnetic field perturbation, propagates at the speed of light into the domain from the edge. Hence remaining free charges are accelerated throughout the domain by the electromagnetic disturbance.

This idea was developed by Diver and Teodoro (2008) in their paper "Unplugging the Universe: the neglected electromagnetic consequence of decoupling". They posed the question; what is the correct physical model that encompasses the critical physics? The paper constructed the model by identifying the appropriate timescales that have to be considered. There are three such timescales: the time for changes to communicate electromagnetically across the domain, which propagate at the speed of light; the timescale over which the magnetic domains recombine, which is fast because it is governed by atomic processes; and finally the timescale for this process to happen all over the Universe, which is the slowest. In order to accurately model the physics of this epoch, the crucial, fastest timescale is the first one: electromagnetic changes communicated at the speed of light. In other words, the standard cosmological models

[1]Here free charges means those charges in the domain that are not part of the conduction current density

that use a magnetohydrodynamic (MHD) plasma (Durrer et al. 1998; Subramanian and Barrow 1998a,b; Jedamzik et al. 2000), which is limited by the fact that it only works for slow, fluid timescales, is fundamentally compromised. Diver and Teodoro (2008) concluded that the only model that takes account of the appropriate physics timescales is a fully-electromagnetic model.

An overview of their model reveals that they have discovered a physical process whereby a small but non-zero population of charges, that are close to but not taking part in the current density region between two magnetic domains, are accelerated by the time-varying electric field induced by the displacement current when the conduction current rapidly decays. The simple example they use to illustrate made an estimate of the maximum kinetic energy electrons can obtain is around $\sim 7\,\mathrm{keV}$, roughly equivalent to about 1.4% of their rest mass energy. The important point is that this is a direct result of the large-scale neutralisation of an inhomogeneously-magnetised plasma. It is a physical consequence of the recombination during the epoch of decoupling. The resulting small population of energetic charges has a very small cross-section so many of the charges will persist into the early Universe, where they will be well out of thermal equilibrium with the rest of the baryonic matter. This has the possibility of providing a (tiny) contribution to an ultra-low-frequency non-thermal component of the microwave background. Perhaps more interestingly, however, is the potential effect this population could have on large-scale structure formation, since a charge imbalance of just 1 part in 10^{39} could bias the gravitational collapse of gas and dust.

5.1.1 Numerically Simulating the Acceleration of Charges by Magnetic Collapse

As described in section 1.3.2, the magnetic domains are assumed to be sustained by a tiny proportion of the charges in the plasma differentially orbiting around the domain edges, with the magnetic field coherent over a scale length greater than the radius of the domain. This must be true since in order to refract the coherent magnetic field i.e.

to change the direction of it at the boundary between two domains, there must either be a material change or a current density located at the boundary. In the cosmological context, the latter case must be true, and the current density located at the boundary of a domain sustains the coherent magnetic field within it. A single domain can be approximated initially as an infinite solenoid.

The conduction current at the domain boundaries consists of a tiny minority of the charged particles in the domain, which would also recombine into neutral atoms just as the vast majority of "free" charges[2] within the domain would. Removing charges from the current density in this way would make the conduction current decrease, which induces an electromagnetic response. The magnetic field sustained by the conduction current would also decrease, but this would be opposed by an induced displacement current. The displacement current is a time-varying electric field, which will propagate into the domain along with a magnetic perturbation (and the background magnetic collapse), affecting and accelerating the remaining free charges[3].

In the following section, the electromagnetic response to current collapse in an infinite solenoid will be derived, and the analytic form of the induced electric and magnetic fields will be applied to the computational model developed in chapter 4. Diver and Teodoro (2008) predicted that electrons could reach energies of $\sim$ 7keV when accelerated by magnetic collapse. These simulations will test their predictions, and the model will be expanded and generalised such that more complex systems and arrangements of magnetic field can be studied.

The simulations track the response of a number of test electrons to the electric and magnetic fields which are essentially imposed. The electron population is sparse enough, especially towards the end of global recombination, such that the electron-electron field interaction is utterly negligible compared to the imposed background and induced fields. The electromagnetic feedback on charges in the current-carrying region (the narrow ring at the boundary where the imposed current density is located)

[2]Free in this context means the general charges that are not taking part in the conduction current.

[3]Around 1 in 10^5 of the initial number.

is not considered in this simple model for now, but should be a priority in future work.

5.2 Electromagnetic Evolution

To study the electromagnetic evolution of any system, Maxwell's equations are always the best starting point. From there a second-order partial differential equation can be derived that describes the electric field evolution. Solving this equation yields the analytic form of the electric field as a function of both space and time. The analytic form of the magnetic field evolution follows by combining this solution with Faraday's law.

The simplest case of magnetic domain that we can study is the form of a single solenoid. The solenoid can be considered to have infinite length since its radius is much less than the scale length of any significant changes along its axis. Solutions of this kind can also be used as building blocks to construct solutions to more complex systems, and this will be discussed later.

Consider an infinite solenoid 5.1with the axis pointing in the axial (z-) direction of a cylindrical polar co-ordinate system. The current density $\mathbf{J}$ is entirely confined to a narrow band in the azimuthal (ϕ-) direction, and accordingly the magnetic field sustained by the conduction current is uniform in the axial direction inside the solenoid, and zero everywhere outside it. This geometry means that when the current density decreases with time, the resultant induced electric field is azimuthal only, and the induced magnetic perturbation is confined to the z-direction.

5.2.1 The Electric Field Evolution

To derive the equation describing the electric field evolution, begin with Faraday's law and the complete form of Ampere's law:

$$\nabla \times \mathbf{E} = -\frac{\partial \mathbf{B}}{\partial t} \tag{5.1}$$

$$\nabla \times \mathbf{B} = \mu_0 \mathbf{J} + \frac{1}{c^2}\frac{\partial \mathbf{E}}{\partial t} \tag{5.2}$$

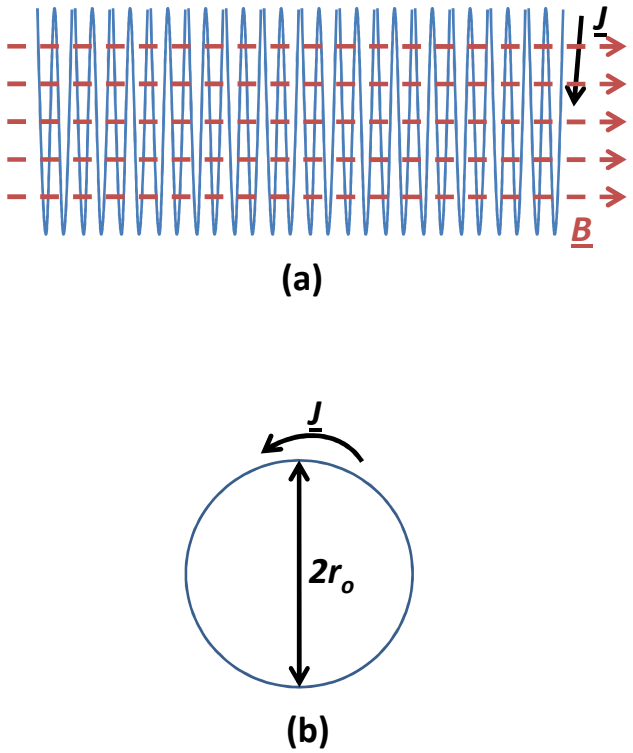

Figure 5.1: Diagram of an infinite solenoid. The top picture (a) shows the coils of radius r_o carrying current density **J** in the *phi*-direction only, resulting in a uniform magnetic field **B** inside the coil. For clarity, picture (b) shows the same solenoid from the perspective along the antiparallel direction to the magnetic field.

where $\mathbf{E} = E_\phi\hat{\phi}$ is the electric field, $\mathbf{B} = B_z\hat{\mathbf{z}}$ is the total magnetic field, $\mathbf{J} = J_\phi\hat{\phi}$ is the current density, μ_0 is the permeability of free space and c is the speed of light in vacuum.

Write the components explicitly in cylindrical polar co-ordinates $(\hat{r}, \hat{\phi}, \hat{z})$, taking

the curl of equation 5.1 and the time-derivative of equation 5.2:

$$\nabla \times (\nabla \times \mathbf{E}) = -\hat{\phi}\left(\frac{\partial^2 E_\phi}{\partial r^2} + \frac{1}{r}\frac{\partial E_\phi}{\partial r} - \frac{1}{r^2}E_\phi\right) \tag{5.3}$$

$$= -\frac{\partial}{\partial t}\nabla \times \mathbf{B} \tag{5.4}$$

$$\frac{\partial}{\partial t}(\nabla \times \mathbf{B}) = \mu_0\hat{\phi}\left(\frac{\partial J_\phi}{\partial t} + \frac{1}{c^2}\frac{\partial^2 \mathbf{E}}{\partial t^2}\right) \tag{5.5}$$

Now by combining equations 5.4 and 5.5 to eliminate B_z, a second-order hyperbolic differential equation in E_ϕ emerges:

$$\frac{1}{c^2}\frac{\partial^2 E_\phi}{\partial t^2} - \frac{\partial^2 E_\phi}{\partial r^2} - \frac{1}{r}\frac{\partial E_\phi}{\partial r} + \frac{1}{r^2}E_\phi = -\mu_0\frac{\partial J_\phi}{\partial t} \tag{5.6}$$

Since this is for a computational model, all quantities must be dimensionless. The following substitutions were made in order to non-dimensionalise the equations. In each case the quantity with subscript 0 is the dimensional part, and the Greek letter is the dimensionless variable to cast the equations in. First substitute the main variables:

$$r = r_0\rho \tag{5.7}$$

$$t = t_0\tau \tag{5.8}$$

This means the derivatives are now

$$\frac{d}{dr} = \frac{1}{r_0}\frac{d}{d\rho} \tag{5.9}$$

$$\frac{d}{dt} = \frac{1}{t_0}\frac{d}{d\tau} \tag{5.10}$$

Now, recognising that if the current density is constant then there will be no electric field, the variables are separable as follows:

$$J_\phi(\rho,\tau) = J_0 f(\rho)T(\tau) \tag{5.11}$$

$$E_\phi(\rho,\tau) = E_0 g(\rho)\partial_\tau T(\tau) \tag{5.12}$$

$$B_z(\rho,\tau) = B_0 h(\rho)T(\tau) \tag{5.13}$$

where $f(\rho)$ is a dimensionless function representing the spatial form of the current density which will be specified according to the physical problem studied, and $g(\rho)$

and $h(\rho)$ are the spatial forms of the electric and magnetic fields respectively, and are to be solved for. The simplest form of $f(\rho)$ that can be chosen is $f(\rho) = \delta(\rho - \rho_j)$, i.e. a Dirac delta function centred on $\rho = \rho_j$, where ρ_j is the radius of the solenoid. The delta function can act as a building block and superpositions of multiple delta functions can be substituted to study more complex current densities. $T(\tau)$ is the dimensionless function describing the decay of the current density with time. J_0, E_0 and B_0 are the dimensional parts of the current density and fields.

Substituting equations 5.7 - 5.13 into equation 5.6 and simplifying:

$$\partial_{\rho\rho}g(\rho)\partial_\tau T(\tau)+\frac{1}{\rho}\partial_\rho g(\rho)\partial_\tau T(\tau)-\frac{1}{\rho^2}g(\rho)\partial_\tau T(\tau)-\frac{{r_0}^2}{{t_0}^2}\frac{1}{c^2}g(\rho)\partial_{\tau\tau\tau}T(\tau) = \frac{\mu_0 r_0^2 J_0}{t_0 E_0}f(\rho)\partial_\tau T(\tau) \tag{5.14}$$

where in the usual fashion a ∂ symbol denotes a derivative, with the subscript indicating in which dimension, i.e. the derivatives with respect to our new dimensionless variables ρ (space) and τ (time). Now assume that

$$\frac{\partial\tau\tau\tau T(\tau)}{\partial_\tau T} = \kappa^2 \tag{5.15}$$

where κ is a constant. This gives the form of $T(\tau)$ as

$$T(\tau) = \exp[(-\kappa\tau)] \tag{5.16}$$

and if β is defined as

$$\beta = \frac{r_0\kappa}{ct_0} \tag{5.17}$$

then equation 5.14 now looks like this:

$$\partial_{\rho\rho}g(\rho) + \frac{\partial_\rho g(\rho)}{\rho} - \left(\frac{1}{\rho^2} + \beta^2\right)g(\rho) = \frac{\mu_0 {r_0}^2 J_0}{t_0 E_0}f(\rho) \tag{5.18}$$

The Homogeneous Solution

Examining the homogeneous form of equation 5.18 (i.e. setting the right hand side to zero, see equation 5.19 below), it is clearly a form of the Modified Bessel equation, which has solutions of the form of modified Bessel functions of the first and second

kinds. These are special functions normally associated with cylindrically-symmetric systems.

$$\partial_{\rho\rho} g(\rho) + \frac{\partial_\rho g(\rho)}{\rho} - \left(\frac{1}{\rho^2} + \beta^2\right) g(\rho) = 0 \tag{5.19}$$

The two linearly-independent homogeneous solutions to equation 5.19 are as follows:

$$g_1(\rho) = I_1(\beta\rho) \tag{5.20}$$

$$g_2(\rho) = K_1(\beta\rho) \tag{5.21}$$

where I_1 is the first order modified Bessel function of the first kind, and K_1 is the first order modified Bessel function of the second kind, sometimes known as the first Hankel function. The factor β is related to the rate of decay of the current density during recombination.

The Inhomogeneous Solution

Now use the variation of parameters technique can be used to find the inhomogeneous solution. The technique yields the solution $g(\rho)$ from the two linearly-independent homogeneous solutions $g_1(\rho)$ and $g_2(\rho)$ like so:

$$g(\rho) = g_2(\rho) \int \frac{g_1(\rho) F(\rho) d\rho}{W(g_1, g_2)} - g_1(\rho) \int \frac{g_2(\rho) F(\rho) d\rho}{W(g_1, g_2)} \tag{5.22}$$

where $F(\rho)$ is the right hand side of the inhomogeneous equation, and $W(g_1, g_2)$ is the usual Wronskian, defined as

$$W(u_1(x), u_2(x)) = \frac{du_1(x)}{dx} u_2(x) - u_1(x) \frac{du_2(x)}{dx} \tag{5.23}$$

The Wronskians of I and K functions are well known, and are (Abramowitz and Stegun 1965)

$$W(I_1(\beta\rho), K_1(\beta\rho)) = \frac{1}{\beta\rho} \tag{5.24}$$

The equation for $g(\rho)$, the spatial distribution of the electric field, can now be written

$$g(\rho) = \beta K_1(\beta\rho) \int I_1(\beta\rho') \rho' F(\rho') d\rho' - \beta I_1(\beta\rho) \int K_1(\beta\rho') \rho' F(\rho') d\rho' \tag{5.25}$$

Applying boundary conditions, we can neglect the second part of this solution since it is the region of the domain inside the solenoid that will be studied, i.e. between $r = 0$ and $r = r_j$. Since $K_1(r) \to \infty$ as $r \to 0$, including this term would be unphysical. Finally, the electric field can be expressed fully as

$$E_\phi(\rho, \tau) = \frac{\mu_0 {r_0}^2 J_0}{c t_0 E_0} \kappa \rho_j K_1(\beta\rho_j) I_1(\beta\rho) \exp(-\kappa\tau) \tag{5.26}$$

5.2.2 The Magnetic Field Evolution

Now the electric field evolution is known, the evolution in the total magnetic field can be found using Faraday's law (which must always hold)

$$\nabla \times \mathbf{E} = -\partial_t \mathbf{B} \tag{5.27}$$

In cylindrical coordinates with components written explicitly this is

$$\frac{1}{r} \partial_r (r E_\phi) = -\partial_t B_z \tag{5.28}$$

Now substitute equations 5.12 and 5.13 and change to dimensionless variables using equations 5.7, 5.8 and 5.16:

$$\frac{E_0}{r_0} \frac{1}{\rho} \partial_\rho (\rho g(\rho)) \kappa T(\tau) = \frac{B_0}{t_0} h(\rho) \kappa T(\tau) \tag{5.29}$$

After rearranging and taking the derivatives with respect to ρ:

$$\partial_\rho h(\rho) = \frac{E_0 t_0}{B_0 r_0} \left(\partial_{\rho\rho} g(\rho) + \frac{1}{\rho} \partial_\rho g(\rho) - \frac{1}{\rho^2} g(\rho) \right) \tag{5.30}$$

Now after combining equation 5.30 with equation 5.18 and simplifying:

$$\partial_\rho h(\rho) = \frac{r_0 \mu_0 J_0}{E_0} f(\rho) + \frac{r_0^4 \mu_0 J_0}{c^3 t_0^3 B_0} \kappa^3 \rho_j K_1(\beta\rho_j) I_1(\beta\rho) \tag{5.31}$$

and integrate over ρ to find the final form of the magnetic field equation:

$$B_z(\rho, \tau) = B_0 \exp(-\kappa\tau) \left(\frac{r_0 \mu_0 J_0}{B_0} + \frac{r_0^3 \mu_0 J_0}{c^2 t_0^2 B_0} \kappa^2 \rho_j K_1(\beta) \rho_j I_0(\beta\rho) \right) \tag{5.32}$$

5.2.3 Identifying the Control Parameters

Examining equations 5.26 and 5.32, there are three groups of dimensional quantities. Each of these groups can be identified as an overall non-dimensional control parameter that can be used to vary the simulations. These are

$$Q_1 = \frac{r_0^3 \mu_0 J_0}{c t_0^2 E_0} \tag{5.33}$$

$$Q_2 = \frac{r_0 \mu_0 J_0}{B_0} \tag{5.34}$$

$$Q_3 = \frac{r_0^3 \mu_0 J_0}{c^2 t_0^2 B_0} \tag{5.35}$$

Recognising that r_0 and t_0 represent the physical size of space- and time-steps, the characteristic velocity is $v_0 = r_0/t_0$. Furthermore, this velocity can be related to the magnitude of the drift velocity acquired by a charge in the presence of crossed electric and magnetic fields. The drift velocity is given by

$$\mathbf{v}_d = \frac{\mathbf{E} \times \mathbf{B}}{|\mathbf{B}|^2} \tag{5.36}$$

therefore the magnitude is given by $|\mathbf{v}_d| = \frac{|\mathbf{E}|}{|\mathbf{B}|}$. This is the characteristic velocity of the system.

$$v_0 = |\mathbf{v}_d| = \frac{E_0}{B_0} \tag{5.37}$$

Finally, identifying B_0 as the characteristic magnetic field sustained by a current density of J_0 over a scale length of r_0, at the onset of global recombination, Q_2 can be set to be equal to unity. Then substituting equations 5.17 and 5.37 and simplifying the three dimensionless control parameters are now

$$Q_1 = \frac{\beta}{\kappa} \tag{5.38}$$

$$Q_2 = 1 \tag{5.39}$$

$$Q_3 = \frac{\beta^2}{\kappa^2} = Q_1^2 \tag{5.40}$$

The two constants β and κ are related to the spatial scale of the system and the decay constant in the exponential current collapse respectively. These affect the time

an electron spends under the influence of the induced field perturbation. For example, if κ is small then a test electron will experience stronger electric field perturbations over a longer time than if κ was large. Now the full, dimensionless analytic expressions for the electric and magnetic fields can be written:

$$E_\phi(\rho,\tau) = Q_1\kappa\rho_j K_1(\beta\rho_j)I_1(\beta\rho)\exp(-\kappa\tau) \quad (5.41)$$

$$B_z(\rho,\tau) = \left(1 + Q_1^2\kappa^2\rho_j K_1(\beta)\rho_j I_0(\beta\rho)\right)\exp(-\kappa\tau) \quad (5.42)$$

5.3 The Full Simulations

With the full analytic form of the electric and magnetic field equations, there are just two final stages that must be accounted for. First, the special functions need to be approximated numerically. This can be done very well using a standard approximation. Second, the co-ordinate systems are different; for computational convenience, the Runge-Kutta solver is in Cartesian co-ordinates, but the model equations for the electric and magnetic fields are in cylindrical polar co-ordinates. It is simple to transform between the two however, as long as care is taken.

5.3.1 The Modified Bessel Functions

The solutions for the electric and magnetic field contain special functions known as modified Bessel functions of the first (I_ν for the function of order ν) and second (K_ν) kind. These are related to the more well-known Bessel functions and are actually a special case of those, where normal Bessel functions have a purely imaginary argument. However the modified Bessel functions are functions in their own right with real or complex arguments. They can be written as

$$I_\nu(x) = \imath^{-\nu}J_\nu(\imath x) \quad (5.43)$$

$$= \sum_{m=0}^{\infty}\frac{1}{m!\Gamma(m+\nu+1)}\left(\frac{x}{2}\right)^{2m+\nu} \quad (5.44)$$

$$K_\nu(x) = \frac{\pi}{2}\frac{I_{-\nu}(x) - I_\nu(x)}{\sin\nu\pi} \quad (5.45)$$

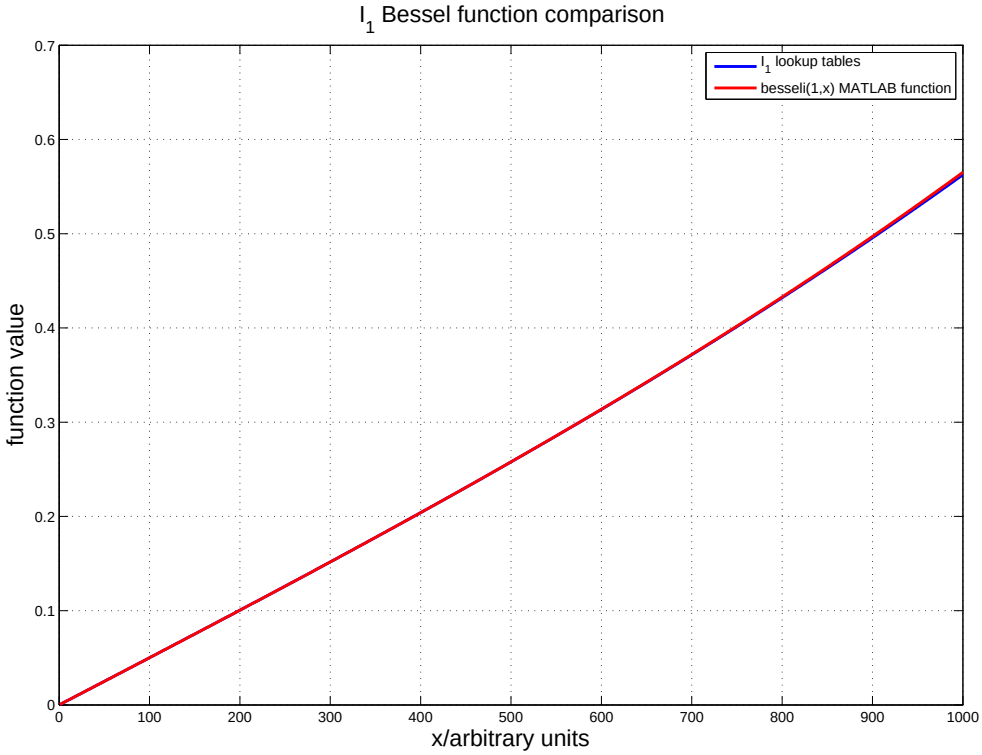

Figure 5.2: The modified Bessel function I_0. This plot shows both the numerical approximation used in the code (blue line), and the comparison to the function built in to MATLAB (red line). There is a noticeable difference of about 2% between the values at one end, but for most of the domain the two are indistiguishable.

where $J_\nu(x)$ is the normal Bessel function of the first kind, of order ν. Rather than oscillating as periodic functions, the modified Bessel functions I_ν and K_ν are exponentially growing and decaying respectively. Some programming packages such as MATLAB have these special functions built in, but since the main code was written in FORTRAN-77 a numerical approximation found in Press et al. (1992) was used.

Figures 5.2, 5.3 and 5.4 show a comparison of the numerical approximations with the special functions built into MATLAB. The two are indistinguishable for the functions I_1 and K_1, and only a maximum of around 2% different for the function I_0.
During startup, the FORTRAN-77 code generated lookup tables for each of the three functions over $1,000$ steps covering the range studied. At each timestep during the

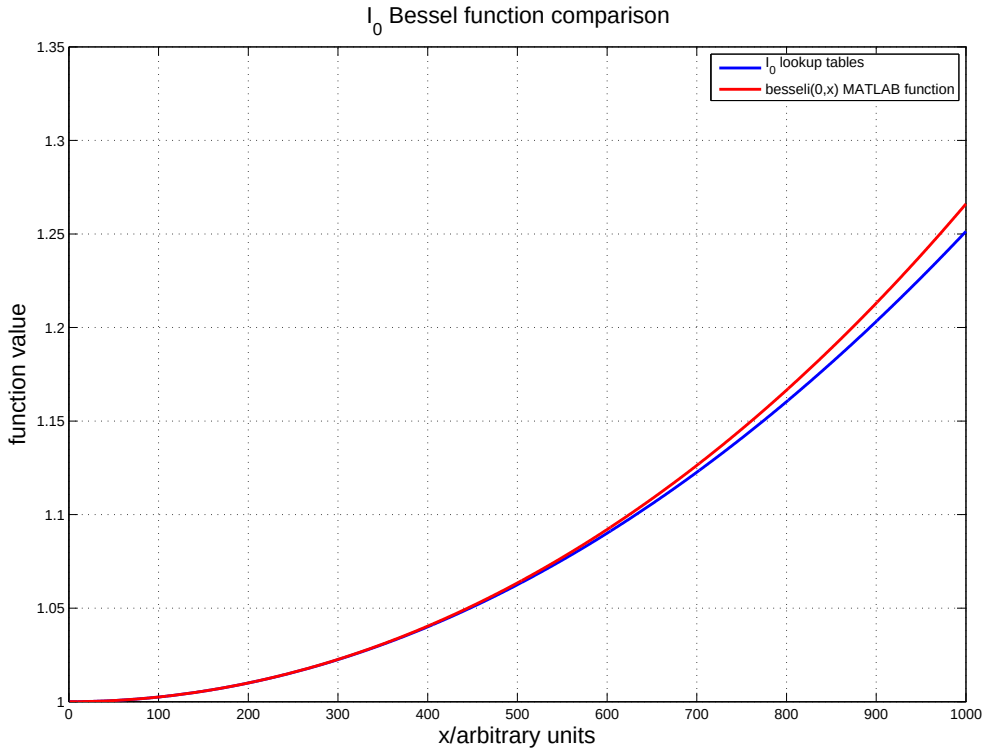

Figure 5.3: The modified Bessel function I_1. This plot shows both the numerical approximation used in the code (blue line), and the comparison to the function built in to MATLAB (red line). The two lines are almost indistinguishable, indicating that the numerical approximation is at least as valid over this range as the MATLAB function.

solution, the electron position was used to look up the value of each function while calculating the electric and magnetic fields at that location. To look up the table, the radial position ρ of the electron was calculated and this was scaled to between 0 and 1 by multiplying by β, which is a scaling factor. Then multiplying by $1,000$ returns which entry is required from the lookup tables. Of course, it is only as simple as that if an integer value is returned. If not, then a simple linear interpolation method was used to find the correct value of the special functions, e.g. for function I_1, lookup value lookbi1:

$$\rho_{table} = \rho * \beta * 1000 \tag{5.46}$$

$$\rho_{round} = \text{floor}(\rho_{table}) \tag{5.47}$$

then (5.48)

$$\text{lookbi1} \quad = \quad \text{bbi1}(\rho_{table}) + (\text{bbi1}(\rho_{round} + 1) - \text{bbi1}(\rho_{round}))\,(\rho_{table} - \rho_{round}) \quad (5.49)$$

where floor(x) is a function that rounds x down to the nearest integer, bbi1(n) refers to the n-th entry of the table bbi1, for looking up values of I_1.

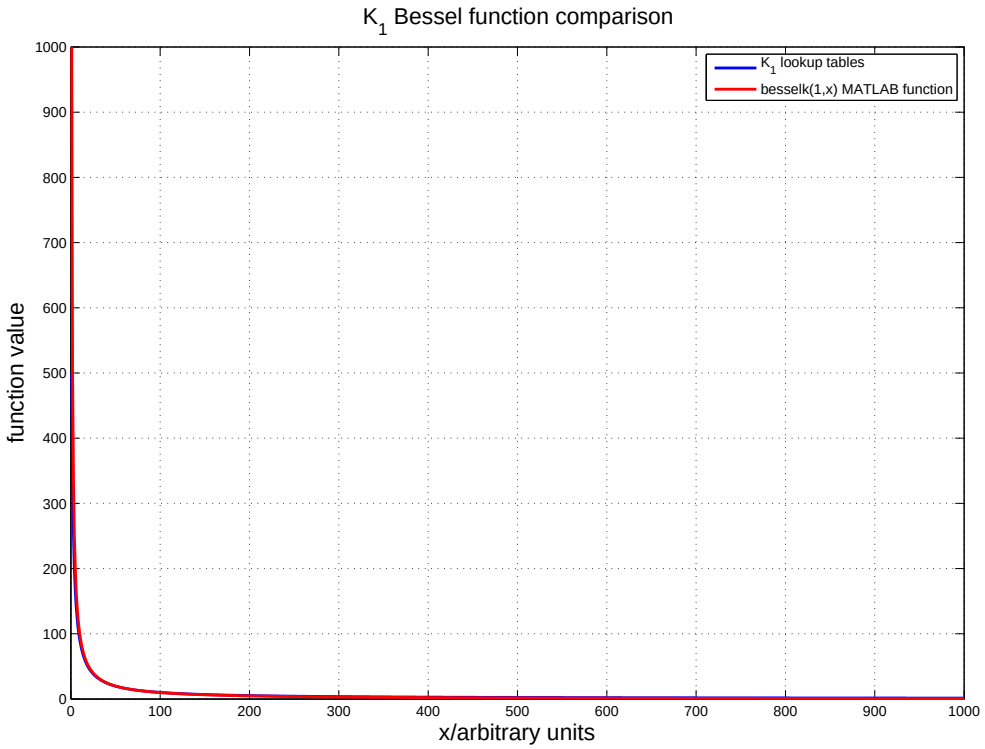

Figure 5.4: The modified Bessel function K_1. This plot shows both the numerical approximation used in the code (blue line), and the comparison to the function built in to MATLAB (red line).

5.3.2 Computing the Full Solutions

Now that it has been established that the simulations are working correctly, and the full analytic field solutions have been derived, the simulations can be used to study the complete system. To recap, the full expression for the electric field induced when the

current density in an infinite solenoid decays exponentially with time is (equation 5.26)

$$E_\phi(\rho,\tau) = \frac{\mu_0 {r_0}^2 J_0}{ct_0 E_0}\kappa\rho_j K_1(\beta\rho_j) I_1(\beta\rho)\exp(-\kappa\tau) \tag{5.50}$$

and the equation for the magnetic field in the system was given in equation 5.32:

$$B_z(\rho,\tau) = B_0\exp(-\kappa\tau)\left(\frac{r_0\mu_0 J_0}{B_0} + \frac{r_0^3\mu_0 J_0}{c^2 t_0^2 B_0}\kappa^2\rho_j K_1(\beta\rho_j I_0(\beta\rho)\right) \tag{5.51}$$

The code equations for the electron dynamics were given in equations 4.26 - 4.29:

$$\begin{aligned}
\frac{d\xi}{d\tau} &= u_\xi \\
\frac{d\zeta}{d\tau} &= u_\zeta \\
\frac{du_\xi}{d\tau} &= P_2 e_\xi + u_\zeta b \\
\frac{du_\zeta}{d\tau} &= P_2 e_\zeta + u_\xi b
\end{aligned}$$

where P_2 is a dimensionless control parameter, set equal to unity in the first instance.

The code equations for the electric and magnetic fields were given in equations 5.41 and 5.42. In order to use them with the solver in Cartesian co-ordinates, the electron's position must be transformed into cylindrical polar co-ordinates, then the ϕ-component of electric field found, and finally the component is transformed back into $x-$ and $y-$components (e_ξ and e_ζ respectively).

$$\rho = \sqrt{\xi^2+\zeta^2} \tag{5.52}$$

$$\phi = \arctan\left(\frac{\zeta}{\xi}\right) \tag{5.53}$$

$$e_\xi(\rho,\tau) = \cos\phi\, Q_1\kappa\rho_j K_1(\beta\rho_j) I_1(\beta\rho)\exp(-\kappa\tau) \tag{5.54}$$

$$e_\zeta(\rho,\tau) = \sin\phi\, Q_1\kappa\rho_j K_1(\beta\rho_j) I_1(\beta\rho)\exp(-\kappa\tau) \tag{5.55}$$

$$b(\rho,\tau) = \left(1 + Q_1^2\kappa^2\rho_j K_1(\beta\rho_j I_0(\beta\rho)\right)\exp(-\kappa\tau) \tag{5.56}$$

and Q_1 is another dimensionless control parameter, again set to unity in the first instance.

5.3.3 Electric and Magnetic Fields

Figure 5.5 shows an example of how the magnitude and spatial form of the electric and magnetic fields inside an infinite solenoid change over time as the magnitude of the current density decreases. The six plots each show a snapshot in time evolution, beginning with the instant an exponential current density decay was first imposed. The blue axes and lines show the magnitude of the z-magnetic field, while the red axes and lines display the total magnitude (i.e. in the ϕ-direction) of the electric field.

5.4 Results

The simulations studied the dynamics of a single electron in the imposed electric and magnetic fields, but hundreds or even thousands of electrons could be studied by looping the main algorithm. As a first approximation it was assumed that modelling hundreds of electrons spaced relatively far apart would mean that the imposed electric field from the current collapse seen by each electron would overwhelmingly dominate over the fields from other electrons, so particle-particle interaction has been neglected for the moment. The electron density is sparse, especially away from the current-carrying region and as global recombination progresses. Additionally, since the electrons accelerate to relatively high energy rather quickly, the collisional cross section rapidly becomes very small indeed. The number density of electrons is low enough, especially as recombination proceeds, such that this is a reasonable first approximation. Therefore for now it is only the influence of the 'global' electric and magnetic fields that is considered.

The electromagnetic feedback on charges in the current-carrying region was neglected for now, because like the free charges, the influence of individual electrons is very small compared to the wider fields imposed. By Lenz's law one would expect the system to oppose the current density decay which should slow the decay, details such as this will be considered as future work.

The data was written to files and then plotted using MATLAB. The code usually evolved 10^5 timesteps in order to achieve the desired resolution, and the data sampled 10^3 of these steps for each electron. These data included full position and velocity data. Additionally, the *full* data for one randomly-chosen electron was recorded for detailed analysis. The value of the decay constant $kappa$ was chosen such that the final current density value was 10^{-5} of the initial current density value, in line with the assumption that the ionisation fraction of the plasma changed from 1 to 10^{-5} during the process of global recombination in the early Universe.

5.4.1 Mean Final Energy of 100 Electrons

The simulation was carried out for 100 electrons, evenly spaced throughout the domain from the centre of the solenoid to just short of the location of the current density. If an electron ever reached the location of the current density, it was treated as having escaped and played no further part in the simulation. Physically this is reasonable, since either the electron would be absorbed into the current density and make a negligible extra contribution, or it would escape through into a neighbouring magnetic domain which is not being considered at the moment. Only electrons that start very close ($< 5\%$ of the size of the computational domain) to the location of the current density move near enough to escape during the evolution time studied.

To turn the numbers given out by the code into physical units certain scale lengths must be set, that were earlier substituted out to make all quantities dimensionless. By setting the magnetic field scale the gyro-frequency equation can be used to set the time scale. Then setting either the velocity scale or the length scale will ensure that all scale lengths are defined.

For example, if the initial value of the background magnetic field, sustained by the current density of the circulating charges, is chosen to be $B_0 \sim 10^{-12}\,\mathrm{T}$ (Ichiki et al. 2006; Barrow et al. 1997; Jedamzik et al. 2000; Chen et al. 2004), then the timescale t_0 is set as follows:

$$t_0 = \frac{1}{\omega_c} \tag{5.57}$$

$$\omega_c = \frac{q_e B_0}{m_e} \tag{5.58}$$

$$= \frac{1.6 \times 10^{-19} \times 10^{-12}}{9.11 \times 10^{-31}} \tag{5.59}$$

$$\therefore t_0 = 5 \text{ seconds} \tag{5.60}$$

Figure 5.6 shows results for simulations using the parameters $P_1 = P_2 = P_3 = 1$. This can be interpreted as a system with a background magnetic field of 10^{-12} T, a characteristic speed of 10^8 ms^{-1}, and characteristic length scale of $5 \times 10^8\, m$. The speed scale is of an order of magnitude consistent with what is commonly assumed in the literature to be the sound speed at the onset of global recombination (usually $c/\sqrt{3}$ [4]). This is reasonable, since it can be expected that the sound speed could be very important for the progress of global recombination because temperature fluctuations would spread throughout the plasma at the sound speed. The length scale is simply the Larmor radius for an electron moving at speed 10^8 ms^{-1} in a background magnetic field of 10^{-12} T.

In the plot, the points show the mean final velocity (i.e. the gyro motion is averaged out over ten or so cycles leaving only the drift component of motion) while the error bars show the deviation from the mean. The usual standard deviation formula was used to calculate this. Large error bars indicate that the gyro motion is still significant, while small error bars show that the drift motion completely dominates. The final mean kinetic energy of electrons spaced throughout the domain ranges from ~ 0 keV for those far from the current density all the way up to ~ 9 keV for those nearest the domain edge. This is consistent with the calculations presented by Diver and Teodoro (2008) who suggested that a kinetic energy of around 7 keV could be achievable for a free electron accelerated by the electromagnetic response to recombination. In the context that the "thermal" energy is around 0.3 eV, a possible increase in kinetic energy

[4] For a cosmological model consistent with current observations.

of four orders of magnitude above the background means that even a tiny proportion of these energetic electrons could have an effect in the post-decoupling Universe.

5.5 Discussion

The aim of this chapter was to derive a self-consistent model of magnetic collapse during large-scale neutralisation of an inhomogeneously-magnetised plasma. The plasma was considered to be split into large magnetic domains, each with its own local, roughly uniform background magnetic field sustained by conduction current i.e. charges circulating around the edge of the domain. This initial study considered only a single magnetic domain, but it is straightforward to build more complex examples within the framework presented here.

In deriving the electromagnetic equations, it was assumed that the plasma density could essentially be imposed. This allows the consideration of different models for the plasma behaviour during neutralisation - linking the current density to the plasma (i.e. ion) density means that it is the plasma density evolution which is imposed, with the conduction current density and hence the magnetic field sustained by it affected accordingly. In the case presented here an exponential fall-off in ion density was assumed, as the transition from fully-ionised to almost-neutral progressed globally. There is scope to try out alternative models for the progress of global neutralisation, for example a propagating neutralisation front travelling at the sound speed, or a spotty domain with localised hot-spots of neutralisation that spread outwards until the domain is fully neutral.

The single infinite solenoid magnetic domain is the simplest possible example, but it is effective in making the point that regardless of how the magnetic fields were first induced, *if* one assumes that the Universe was magnetized pre-Decoupling, there are electromagnetic consequences to consider *during* the epoch of Decoupling. Any more complex examples can be described by a superposition of many solenoids. One such example would be to consider two adjacent magnetic domains with anti-aligned

uniform magnetic fields inside them. Picture two solenoids next to each other, at their plane of intersection there would be a "hot spot" of current density that experienced contributions from both solenoids. This hot spot would result in slightly different field solutions in the two domains due to differences in the function describing the current density. This also allows the tantalising possibility of remote effects between magnetic domains, if one could construct a model where only one of the two magnetic domains is experiencing significant recombination. Such a model may be pathological, but in this case the current density hot spot in the non-recombining domain would, over time, relax to the same magnitude as the conduction current density for the rest of that domain. The electromagnetic response for that localised collapse would be limited, but could still affect charges in the domain without the domain itself being affected by neutralisation. This is an example of the sort of study that is entirely within the abilities of the model.

For physical scale lengths consistent with much of the literature, the order of magnitude (10keV, compared with a thermal energy of $0.3\mathbf{eV}$) of kinetic energy gained by the electrons in these simulations are consistent with those predicted by the simple calculation in Diver and Teodoro (2008). The agreement of the results from this simple computational model with the earlier prediction motivates the development of a more detailed model, for example one that includes electromagnetic feedback from the accelerated charges and models the current-carrying region to higher resolution.

Once the electrons are accelerated to such energies, around four orders of magnitude greater than the thermal energy, their collisional cross section is tiny and so generally the accelerated electrons would carry on uninterrupted into the otherwise cool, dark Universe. Further work that this study leads into includes finding out how an energetic population of electrons could affect the post-recombination Universe on large scales, such as contributing a Coulomb interaction to gravitational collapse models. Even a very small charge density could contribute to biasing large scale structure formation. Consider for example the forces exerted by a population of 10^3 hydrogen

atoms on a passing free electron: the gravitational force F_G is

$$F_G = \frac{GMm}{r^2} \tag{5.61}$$

where G is the gravitational constant, $M = 10^3 \times (m_e + m_p)$ is the total mass of the ensemble[5], m is the mass of the single electron and r is the distance between the electron and the ensemble of atoms. Meanwhile the electrostatic force F_E is given by:

$$F_E = \frac{Ee}{4\pi\epsilon_0 r^2} \tag{5.62}$$

where E is any unbalanced charge in the ensemble, e is the charge of the free electron, r is the separation distance, and ϵ_0 is the permittivity of free space. Then if there is even a single unbalanced charge in the ensemble of atoms, the ratio of F_E to F_G is

$$\begin{aligned} \frac{F_E}{F_G} &= \frac{e^2}{4\pi\epsilon_0 GMm} \\ &= \frac{(1.6 \times 10^{-19})^2}{4\pi \times 8.854 \times 10^{-12} \times 6.673 \times 10^{-11} \times 1.673 \times 10^{-24} \times 9.11 \times 10^{-31}} \\ &= 2.3 \times 10^{36} \end{aligned} \tag{5.63}$$

i.e. it would require an ensemble of 2.3×10^{39} atoms to gravitationally overcome the electrostatic force between a single free electron and an single unbalanced unit of electric charge within the ensemble. The converse of this is that a charge imbalance of just three parts in 10^{39} is enough for the electrostatic force to dominate over the gravitational attraction between groups of neutral atoms. Over long distances this will not happen due to charge shielding as discussed in section 1.5.1, but small perturbations could bias the initial gravitational collapse of gas and dust during the earliest structure or star formation.

5.6 Summary

This chapter used the solver developed in chapter 4 to study the motion of free charged particles responding to the magnetic collapse of a solenoidal magnetic field. The mean

[5] where m_e and m_p are the mass of the electron and proton respectively

final energy of electrons evenly spaced throughout the solenoidal magnetic domain was found to reach a maximum of around 9 keV in figure 5.6. Parameter choices were consistent with those used in the literature. A simple example was shown to elucidate how these energetic electrons could play a potential, and neglected, role in the early post-decoupling Universe by biasing the earliest gravitational collapses for first stars and large scale structure formation.

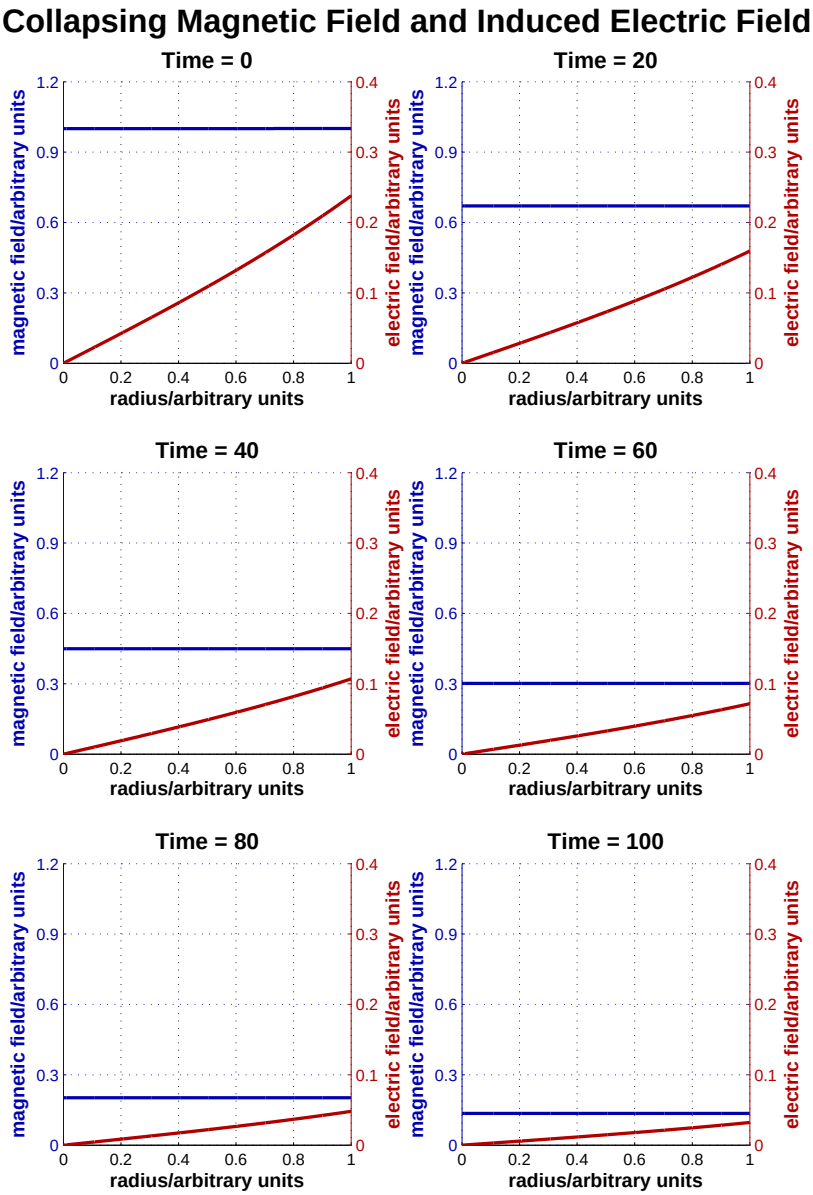

Figure 5.5: Snapshots of the magnitude of magnetic field (blue lines and axes) and electric field (red lines and axes) as a function of radius inside an infinite solenoid (see figure 5.1). Radius = 1 corresponds to the conduction current-carrying part of the solenoid. The conduction current density in the solenoid is decreasing exponentially, with the decrease beginning at the instant $Time = 0$ as shown in the top-left plot. Subsequent plots show snapshots as time advances. The magnetic field remains approximately uniform as it decays along with the current that sustained it. A small perturbation related to the collapse is dominated by the background field. The electric field induced has the form of the modified Bessel function I_1 and has higher magnitude closer to the current-carrying region. It too decays as the rate of current decay decreases with time.

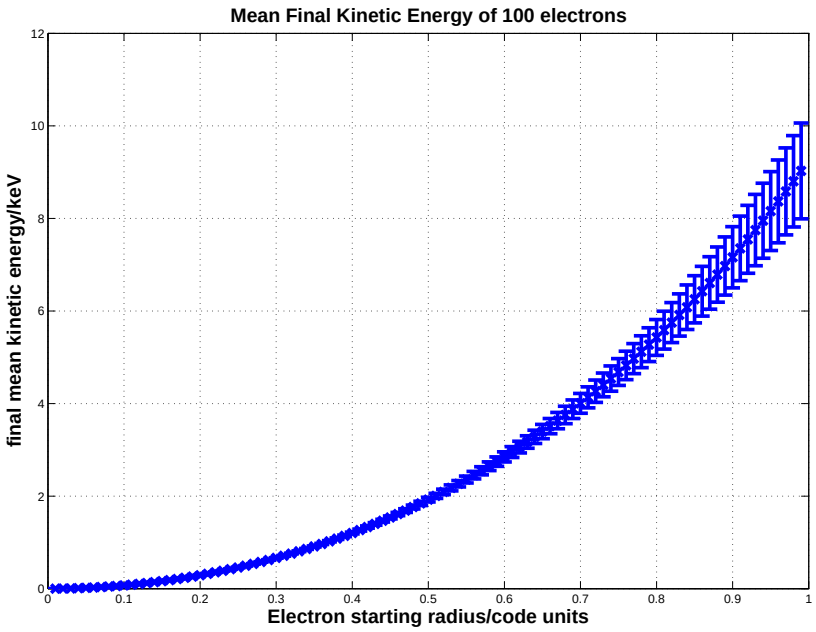

Figure 5.6: Each point denotes the final mean kinetic energy of a single electron, in keV. The error bars essentially show the gyro motion, calculated by standard deviation from the mean kinetic energy. The electrons were initially stationary, and evenly spaced along the radius of the domain. Therefore the x-axis can be considered to show the electron starting positions, with $x = 0$ being the centre of the solenoid and $x = 100$ as the location of the current density. The simulations are fully two-dimensional, but due to the cylindrical symmetry of this example the results can be presented in this one-dimensional fashion.

6

Conclusions and Future Work

"There is, though I do not know how there is or why there is, a sense of infinite peace and protection in the glittering hosts of heaven. There it must be, I think, in the vast and eternal laws of matter, and not in the daily cares and sins and troubles of men, that whatever is more than animal within us must find its solace and its hope."

H. G. Wells, 'The Island of Dr Moreau'

6.1 The Past

In the Beginning...

Like any research project, the primary objective of this thesis changed considerably over its course as it progressed, though the final result is pleasingly relevant to both the original vision and to a range of alternative applications. At the outset in Oc-

tober 2008, the plan was to bring some understanding of plasma physics to cosmology, a field where there is the requirement for but not an abundance of plasma- and electromagnetism-related theoretical work. There were three strands to the initial project plan: of these the first one, developing the theoretical and computational model for electron acceleration during the cosmological epoch of recombination, survives here intact. However, it turns out that the model may have important relevance closer to home in pulsed plasma devices. Another interesting area to explore would be to investigate the possibility of using modulated magnetic fields as an acceleration technique.

The second strand of the project originally began as an investigation into the viability of observing the polarisation signatures of Alfvén waves embedded in the microwave background. When it became clear that an Alfvén wave propagating during the global recombination of the Universe would in fact be engaged in a race to see which instability destroyed it first, and that furthermore the precision of polarisation observations required will not be available in the near future, the focus shifted somewhat. As a result, the investigation of the observational method first proposed by Chandrasekhar and Fermi (1953) has shown some very interesting conclusions. The initial narrowly targeted study has turned out to be much more widely relevant than expected, a great positive of this project.

The third and final topic that was initially expected to form a part of this thesis was unfortunately eclipsed by the the other two developments, and for this reason it is considered to be a priority for future work. This strand essentially studied the thermodynamics of the epoch of recombination, prompted by questioning whether or not the microwave background could possibly be a physically perfect black body. The black body assumption depends on the electrons (dominant in terms of affecting the measurable black body temperature): specifically, on the electron energy distribution being a Maxwellian. The process of recombination, taking $100,000$ years, would preferentially remove electrons within a narrow energy range from the population, thus altering the velocity distribution. The distribution would rapidly re-equilibrate

to a thermal signature, but it would be unlikely to return to the initial temperature. This is a runaway effect which early calculations show could lead to something similar to a noise "floor" in microwave background observations of around 1 part in 10^6 - coincidentally the expected precision of PLANCK satellite observations.

6.2 The Present

The thesis itself can be split into two parts - the part investigating wave modes in partially-ionised plasmas in the fluid limit, explored in chapters 2 and 3; and the part consisting of chapters 4 and 5, which specifically studied recombining plasmas.

Wave Modes in Partially-Ionised Plasmas

In chapter 2, the theoretical model of a partially-ionised plasma as a momentum-coupled mixture of a neutral fluid and an MHD plasma was further developed from that first described by Diver et al. (2006). The motivation was for a model from first principles, that made no assumption about the nature of the interaction between the plasma and neutral gas other than that the collisional momentum exchange took the Boltzmann form. A computational model of wave modes induced in such a mixture was written, and examples of the complex, hybrid response were shown. The inevitable superposition of different wave modes resulting from excitation to either the plasma or the neutral gas was demonstrated. In particular, it was clear that the neutral gas could be perturbed indirectly even by purely magnetic wave modes (i.e. transverse Alfvén waves), while conversely it was seen that sonic waves in the neutral gas could indirectly induce coherent magnetic perturbations via the plasma. This is despite the neutral fluid neither exerting nor experiencing any magnetic influence.

Chapter 3 put the computational model to use, in order to test it with the predictions made by the widely-used Chandrasekhar-Fermi observational method (Chandrasekhar and Fermi (1953), abbreviated to CF53). The method combines observations of velocity and polarisation dispersion to estimate the magnetic flux density in astrophysical

objects such as molecular clouds or nebulae. The CF53 method was tested on three key assumptions, and for all of them it was found that some refinement might be necessary to avoid systematic errors when interpreting the new generation of high-precision polarisation data.

Electron Acceleration by Magnetic Collapse

Chapter 5 developed a theoretical and computational method for modelling the motion of charged particles in a generalised configuration of electric and magnetic fields. The method was tested with some very simple examples and was found to work correctly, with the test electrons behaving as predicted by theory. The computational model was then used in chapter 6 to study a much more complex field configuration, derived from first principles. The specific study was of a single magnetic domain in the early Universe undergoing recombination. Assuming that, as observations suggest, there were magnetic fields coherent over long scale-lengths at this epoch, then the sustaining conduction current in the plasma would be reduced as recombination progressed. The unavoidable electromagnetic consequences of such a current collapse were derived, with induced electric field affecting remaining charges in the domain. The computational model found that electrons affected by the induced fields were found to be accelerated to energies of around 9 keV, consistent with the theoretical prediction made by Diver and Teodoro (2008). This would mean the Universe would have been seeded with a very sparse population of relatively high-energy electrons just as the evolution became truly dominated by gravitational forces. These charged particles could have an influence on localised gravitational collapse, providing a bias for early structure formation. It was shown that a charge imbalance of around one part in 10^{39} could make the electrostatic force dominant over gravitational attraction.

6.3 The Future

As it should, this thesis leaves some very interesting avenues to be explored further in future work. The various aspects are applicable to a range of fields, from cosmology and astrophysics to lab plasma experiments and fusion.

Refining the Chandrasekhar-Fermi Method

It is all very well providing theoretical results showing that the CF53 method needs to be refined, but actually improving the interpretation of observations should be the next step. Currently the CF53 method is checked by comparing observations to predicted polarisation spectrums taken from simulations of MHD turbulence (Zweibel 1990; Heitsch et al. 2001; Ostriker et al. 2001). However, these methods make the same assumptions as CF53 itself, and those same assumptions are challenged by the results presented in chapter 3. For this reason a priority for future work should be to develop the computational model to the point where it can make predictions that can be compared to observations in the same way as the MHD turbulence simulations. This would give an indication of how to proceed in improving the interpretation of the CF53 method.

Computational Models for Inhomogeneous and Recombining Plasmas

An interesting alternative method that was explored for this work was the possibility of finding analytic solutions to the rate equations of reaction and carrying this over into the other equations. Essentially this would allow full study of the microphysics of the system rather than imposing quantity changes on it, and lead to a more natural physical model overall. In this case, unlike the other models described, it is the temperature of the plasma that is the crucial quantity for starting the overall reaction. It is possible to make reasonable assumptions about the temperature evolution up until the onset of global recombination. A plasma undergoing the process of global neutralisation is by definition *not* in equilibrium. However, it is also possible to consider the plasma as

evolving through a series of quasi-equilibria throughout the reaction. The total energy in the system must always be conserved, therefore an energy equation can be used to close the system.

Rate equations are a useful technique that cleverly take account of physics acting on fast timescales while working in a slower-timescale fluid model overall. It can be thought of as applying an average of the faster effects over a slower timescale. The use of rate equations is well-understood, especially when it comes to studying e.g. temperature-dependent atomic processes in a fluid context.

The step that will be employed here is to recognise that there is an energy transfer along with the transfer of density between two populations. In the recombining plasma case the direction of density transfer is from the ionised population to the neutral one. Since electrons formally do not exist in MHD one cannot think about them specifically. However, one can consider the *indirect* impact that the electron population has. Electrons are more maneuverable than ions, therefore they are far more responsive to temperature changes. Conversely, if the electron population changes, this has a more rapid effect on the temperature than would simply changing the ion population. It will be possible to develop a model taking account of the impact of the electron population, but without explicitly modelling electrons because that would be invalid in MHD.

Consider the atomic reactions governing the ionisation and neutralisation of plasma, the simplest of which is shown as a two-way chemical reaction in equation 6.1:

$$H + \gamma \rightleftharpoons e^- + p^+ \tag{6.1}$$

where H represents a neutral Hydrogen atom, γ an energetic photon, e^- an electron and p^+ a proton. The forwards reaction of ionisation depletes the neutral population and increases the ion population, and vice versa for the reverse reaction (neutralisation). For this system, equilibrium is defined as the condition where the forward and reverse reactions are balanced, resulting in zero net change in the number density of any single species. Obviously mass conservation dictates that there can be no net change in the total number density (neutrals plus ions). Global recombination will be-

gin when the temperature falls low enough such that the neutralisation reaction dominates the ionisation, in other words when the forwards reaction happens much more frequently than the reverse reaction, unbalancing the system.

The basic algorithm to be used in developing simulations is as follows, e.g. for the case of a recombining plasma:

1. Initial Conditions: The temperature is such that the system is just out of equilibrium in favour of recombination. The driving wall produces consistent perturbations of choice that propagate into the computational domain, just as in the static case.

2. Fluid Equations: These are evolved forward one timestep as for the Lax-Wendroff solver used in the static model. A different solver method may need to be used for this stage since Lax-Wendroff is diffusive and may not conserve energy with 100% accuracy.

3. Rate Coefficients: The thermal perturbation associated with density perturbations at each point in the computational domain can be calculated using the equations of state: a new temperature can be found that reasonably assumes thermal equilibrium is reached more quickly than the fluid timescale. Hence the new rate coefficients, in Arrhenius form, can be calculated.

4. Rate Equations: With the new coefficients calculated, the equilibrium rate equations for the next timestep can be computed using the rate equations.

5. Energy Balance: Finally, energy conservation can be used to find the energy balance at the beginning of the next timestep. 'Ionisation' (an increase in plasma density with a corresponding decrease in neutral gas density) and 'recombination' (vice versa) transfers energy between kinetic energy and latent neutral gas energy.

6. Repeat from step 2.

A major advantage is that in this method, the large-scale changes of e.g. global recombination do not have to be externally imposed, and the reactions progress naturally. Given the generality of the derivation, there would be scope to use this method to investigate a wide range of physical phenomena, including wave modes in inhomogeneous plasmas, the overall reaction progress for recombination or ionisation, and the temperature evolution of a recombining plasma. The latter study in particular holds great relevance to cosmic microwave background observations. It would also be possible to use the model to study the cooler edge regions of tokamaks.

Temperature Drift of Recombining Plasmas

The brief work that was carried out on this topic suggested that a detailed theoretical model is not too far away.

Energetic Electrons in the Early Neutral Universe

Possibly the most cosmological in context of all potential future work, it would be very interesting to study the effects a sparse population of 10 keV electrons would have on gravitational collapse and early structure formation. There may also be an aspect involving magnetic fields and the first stars. Furthermore, since a charge imbalance of just 1 part in 10^{39} would be enough for electrostatic forces to be comparable to gravity, there is scope to investigate the contribution of this population to large-scale dynamics possibly including the expansion of the Universe. Electromagnetism has been neglected up until now in most, if not all, aspects of cosmology, and there is certainly a niche to be explored for a wide-ranging investigation of the impact it could have.

References

M. Abramowitz and I. A. Stegun. *Handbook of mathematical functions with formulas, graphs, and mathematical tables*. 1965.

R. A. Alpher, R. Herman, and G. A. Gamow. Thermonuclear reactions in the expanding universe. *Phys. Rev.*, 74:1198–1199, Nov 1948. doi: 10.1103/PhysRev.74.1198.2. URL `http://link.aps.org/doi/10.1103/PhysRev.74.1198.2`.

B.-G. Andersson and S. B. Potter. A high sampling-density polarization study of the Southern Coalsack. *MNRAS*, 356:1088–1098, January 2005. doi: 10.1111/j.1365-2966.2004.08538.x.

M. J. Aschwanden. *Physics of the Solar Corona. An Introduction with Problems and Solutions (2nd edition)*. December 2005.

J. Aumont and J. F. Macías-Pérez. Primordial Magnetic Fields with the WMAP and Planck Satellite Experiments. In *Revista Mexicana de Astronomia y Astrofisica Conference Series*, volume 36 of *Revista Mexicana de Astronomia y Astrofisica Conference Series*, pages 236–242, August 2009.

C. Baccigalupi. Planck mission: challenges and expectations for cosmology and particle physics . *Memorie della Societa Astronomica Italiana Supplementi*, 14:20, 2010.

J. D. Barrow, P. G. Ferreira, and J. Silk. Constraints on a Primordial Magnetic Field. *Physical Review Letters*, 78:3610–3613, May 1997. doi: 10.1103/PhysRevLett.78.3610.

E. Battaner and E. Florido. Magnetic fields in the early Universe. In *IAU Symposium*, volume 259 of *IAU Symposium*, pages 529–538, April 2009. doi: 10.1017/S1743921309031214.

C. L. Bennett, M. Bay, M. Halpern, G. Hinshaw, C. Jackson, N. Jarosik, A. Kogut, M. Limon, S. S. Meyer, L. Page, D. N. Spergel, G. S. Tucker, D. T. Wilkinson,

E. Wollack, and E. L. Wright. The Microwave Anisotropy Probe Mission. *ApJ*, 583: 1–23, January 2003. doi: 10.1086/345346.

Andrew J. Benson. Galaxy formation theory. *Physics Reports*, 495(23):33 – 86, 2010. ISSN 0370-1573. doi: 10.1016/j.physrep.2010.06.001. URL http://www.sciencedirect.com/science/article/pii/S037015731000150X.

N. D. R. Bhat and B.-G. Andersson. On the Magnetic Field Through the Upper Centaurus-Lupus Super Bubble in the Vicinity of the Southern Coalsack. *ApJ*, 729: 38, March 2011. doi: 10.1088/0004-637X/729/1/38.

C. Caprini and R. Durrer. Gravitational wave production: A strong constraint on primordial magnetic fields. *Phys. Rev. D*, 65(2):023517, January 2002. doi: 10.1103/PhysRevD.65.023517.

C. Caprini and R. Durrer. Limits on stochastic magnetic fields: A defense of our paper. *Phys. Rev. D*, 72(8):088301, October 2005. doi: 10.1103/PhysRevD.72.088301.

B. W. Carroll and D. A. Ostlie. *An introduction to modern astrophysics and cosmology*. July 2006.

S. Chandrasekhar and E. Fermi. Magnetic Fields in Spiral Arms. *ApJ*, 118:113–115, July 1953. doi: 10.1086/145731.

N. L. Chapman, P. F. Goldsmith, J. L. Pineda, D. P. Clemens, D. Li, and M. Krčo. The Magnetic Field in Taurus Probed by Infrared Polarization. *ApJ*, 741:21, November 2011. doi: 10.1088/0004-637X/741/1/21.

G. Chen, P. Mukherjee, T. Kahniashvili, B. Ratra, and Y. Wang. Looking for Cosmological Alfvén Waves in Wilkinson Microwave Anisotropy Probe Data. *ApJ*, 611: 655–659, August 2004. doi: 10.1086/422213.

J. Cho, E. T. Vishniac, A. Beresnyak, A. Lazarian, and D. Ryu. Growth of Magnetic Fields Induced by Turbulent Motions. *ApJ*, 693:1449–1461, March 2009. doi: 10.1088/0004-637X/693/2/1449.

A. A. da Costa, D. A. Diver, E. W. Laing, C. R. Stark, and L. F. A. Teodoro. Pulsar electrodynamics: Relativistic kinetic theory of radiative plasmas, collective phenomena and their radiation. *Phys. Rev. D*, 83(2):023013, January 2011. doi: 10.1103/PhysRevD.83.023013.

L. Davis, Jr. and J. L. Greenstein. The Polarization of Starlight by Aligned Dust Grains. *ApJ*, 114:206, September 1951. doi: 10.1086/145464.

M. A. de Avillez and D. Breitschwerdt. Does the Interstellar Magnetic Field follow

the Chandrasekhar-Fermi Law? *Baltic Astronomy*, 13:386–391, 2004.

R. O. Dendy. *Plasma Dynamics*. 1990.

R. H. Dicke, P. J. E. Peebles, P. G. Roll, and D. T. Wilkinson. Cosmic Black-Body Radiation. *ApJ*, 142:414–419, July 1965. doi: 10.1086/148306.

D. A. Diver and L. F. A. Teodoro. Unplugging the Universe: the neglected electromagnetic consequence of decoupling. *MNRAS*, 385:L73–L77, March 2008. doi: 10.1111/j.1745-3933.2008.00436.x.

D. A. Diver, H. E. Potts, and L. F. A. Teodoro. Gas-plasma compressional wave coupling by momentum transfer. *New Journal of Physics*, 8:265, November 2006. doi: 10.1088/1367-2630/8/11/265.

D. A. Diver, A. A. da Costa, E. W. Laing, C. R. Stark, and L. F. A. Teodoro. On the surface extraction of electrons in a pulsar. *MNRAS*, 401:613–620, January 2010. doi: 10.1111/j.1365-2966.2009.15684.x.

R. Durrer. Cosmic magnetic fields and the CMB. *New Astronomy Reviews*, 51:275–280, March 2007. doi: 10.1016/j.newar.2006.11.057.

R. Durrer, T. Kahniashvili, and A. Yates. Microwave background anisotropies from Alfvén waves. *Phys. Rev. D*, 58(12):123004, December 1998. doi: 10.1103/PhysRevD.58.123004.

T. A. Enßlin, A. Waelkens, C. Vogt, and A. A. Schekochihin. Future magnetic field studies using the Planck surveyor experiment. *Astronomische Nachrichten*, 327: 626–631, June 2006. doi: 10.1002/asna.200610607.

D. Falceta-Gonçalves, A. Lazarian, and G. Kowal. Studies of Regular and Random Magnetic Fields in the ISM: Statistics of Polarization Vectors and the Chandrasekhar-Fermi Technique. *ApJ*, 679:537–551, May 2008. doi: 10.1086/587479.

E. Fermi. On the Origin of the Cosmic Radiation. *Physical Review*, 75:1169–1174, April 1949. doi: 10.1103/PhysRev.75.1169.

J. P. Freidberg. *Plasma Physics and Fusion Energy*. 2007.

R. D. Gehrz, E. E. Becklin, J. de Buizer, T. Herter, L. D. Keller, A. Krabbe, P. M. Marcum, T. L. Roellig, G. H. L. Sandell, P. Temi, W. D. Vacca, E. T. Young, and H. Zinnecker. Status of the Stratospheric Observatory for Infrared Astronomy (SOFIA). *ArXiv e-prints*, February 2011.

M. Giovannini. The Magnetized Universe. *International Journal of Modern Physics*

D, 13:391–502, 2004. doi: 10.1142/S0218271804004530.

M. Giovannini. Topical Review: Magnetized CMB anisotropies. *Classical and Quantum Gravity*, 23:R1–R44, January 2006. doi: 10.1088/0264-9381/23/2/R01.

M. Giovannini. Electric-magnetic duality and the conditions of inflationary magnetogenesis. *Journal of Cosmology and Astroparticle Physics*, 4:3, April 2010. doi: 10.1088/1475-7516/2010/04/003.

P. Goldreich and W. H. Julian. Pulsar Electrodynamics. *ApJ*, 157:869, August 1969. doi: 10.1086/150119.

D. Grasso and H. R. Rubinstein. Magnetic fields in the early Universe. *Phys. Rep.*, 348:163–266, July 2001. doi: 10.1016/S0370-1573(00)00110-1.

J. S. Hall. Observations of the Polarized Light from Stars. *Science*, 109:166–167, February 1949. doi: 10.1126/science.109.2825.166.

F. Heitsch, E. G. Zweibel, M.-M. Mac Low, P. Li, and M. L. Norman. Magnetic Field Diagnostics Based on Far-Infrared Polarimetry: Tests Using Numerical Simulations. *ApJ*, 561:800–814, November 2001. doi: 10.1086/323489.

R. H. Hildebrand, L. Kirby, J. L. Dotson, M. Houde, and J. E. Vaillancourt. Dispersion of Magnetic Fields in Molecular Clouds. I. *ApJ*, 696:567–573, May 2009. doi: 10.1088/0004-637X/696/1/567.

W. A. Hiltner. Polarization of Light from Distant Stars by Interstellar Medium. *Science*, 109:165, February 1949. doi: 10.1126/science.109.2825.165.

M. Houde, J. E. Vaillancourt, R. H. Hildebrand, S. Chitsazzadeh, and L. Kirby. Dispersion of Magnetic Fields in Molecular Clouds. II. *ApJ*, 706:1504–1516, December 2009. doi: 10.1088/0004-637X/706/2/1504.

K. Ichiki, K. Takahashi, H. Ohno, H. Hanayama, and N. Sugiyama. Cosmological Magnetic Field: A Fossil of Density Perturbations in the Early Universe. *Science*, 311:827–829, February 2006. doi: 10.1126/science.1120690.

K. Ichiki, K. Takahashi, N. Sugiyama, H. Hanayama, and H. Ohno. Generation of Large-Scale Magnetic Fields from Primordial Density Fluctuations. *Modern Physics Letters A*, 22:2091–2098, 2007. doi: 10.1142/S0217732307025339.

R. Jancel and T. Kahan. *Electrodynamics of Plasmas*. 1966.

K. Jedamzik, V. Katalinić, and A. V. Olinto. Limit on Primordial Small-Scale Magnetic Fields from Cosmic Microwave Background Distortions. *Physical Review Letters*, 85:700–703, July 2000. doi: 10.1103/PhysRevLett.85.700.

T. Kahniashvili, A. Kosowsky, A. Mack, and R. Durrer. CMB signatures of a primordial magnetic field. In R. Durrer, J. Garcia-Bellido, and M. Shaposhnikov, editors, *Cosmology and Particle Physics*, volume 555 of *American Institute of Physics Conference Series*, pages 451–456, February 2001. doi: 10.1063/1.1363561.

E. Komatsu, K. M. Smith, J. Dunkley, C. L. Bennett, B. Gold, G. Hinshaw, N. Jarosik, D. Larson, M. R. Nolta, L. Page, D. N. Spergel, M. Halpern, R. S. Hill, A. Kogut, M. Limon, S. S. Meyer, N. Odegard, G. S. Tucker, J. L. Weiland, E. Wollack, and E. L. Wright. Seven-year Wilkinson Microwave Anisotropy Probe (WMAP) Observations: Cosmological Interpretation. *ApJS*, 192:18, February 2011. doi: 10.1088/0067-0049/192/2/18.

A. Kosowsky, T. Kahniashvili, G. Lavrelashvili, and B. Ratra. Faraday rotation of the cosmic microwave background polarization by a stochastic magnetic field. *Phys. Rev. D*, 71(4):043006, February 2005. doi: 10.1103/PhysRevD.71.043006.

R. Kulsrud and W. P. Pearce. The Effect of Wave-Particle Interactions on the Propagation of Cosmic Rays. *ApJ*, 156:445, May 1969. doi: 10.1086/149981.

I. Langmuir. Oscillations in Ionized Gases. *Proceedings of the National Academy of Science*, 14:627–637, August 1928. doi: 10.1073/pnas.14.8.627.

D. Larson, J. Dunkley, G. Hinshaw, E. Komatsu, M. R. Nolta, C. L. Bennett, B. Gold, M. Halpern, R. S. Hill, N. Jarosik, A. Kogut, M. Limon, S. S. Meyer, N. Odegard, L. Page, K. M. Smith, D. N. Spergel, G. S. Tucker, J. L. Weiland, E. Wollack, and E. L. Wright. Seven-year Wilkinson Microwave Anisotropy Probe (WMAP) Observations: Power Spectra and WMAP-derived Parameters. *ApJS*, 192:16, February 2011. doi: 10.1088/0067-0049/192/2/16.

M. Lyutikov. On generation of Crab giant pulses. *MNRAS*, 381:1190–1196, November 2007. doi: 10.1111/j.1365-2966.2007.12318.x.

R. Maartens, C. G. Tsagas, and C. Ungarelli. Magnetized gravitational waves. *Phys. Rev. D*, 63(12):123507, June 2001. doi: 10.1103/PhysRevD.63.123507.

A. Mack, T. Kahniashvili, and A. Kosowsky. Microwave background signatures of a primordial stochastic magnetic field. *Phys. Rev. D*, 65(12):123004, June 2002. doi: 10.1103/PhysRevD.65.123004.

S. A. Mao, B. M. Gaensler, M. Haverkorn, E. G. Zweibel, G. J. Madsen, N. M. McClure-Griffiths, A. Shukurov, and P. P. Kronberg. A Survey of Extragalactic Faraday Rotation at High Galactic Latitude: The Vertical Magnetic Field of the

Milky Way Toward the Galactic Poles. *ApJ*, 714:1170–1186, May 2010. doi: 10.1088/0004-637X/714/2/1170.

J. C. Mather, E. S. Cheng, R. E. Eplee, Jr., R. B. Isaacman, S. S. Meyer, R. A. Shafer, R. Weiss, E. L. Wright, C. L. Bennett, N. W. Boggess, E. Dwek, S. Gulkis, M. G. Hauser, M. Janssen, T. Kelsall, P. M. Lubin, S. H. Moseley, Jr., T. L. Murdock, R. F. Silverberg, G. F. Smoot, and D. T. Wilkinson. A preliminary measurement of the cosmic microwave background spectrum by the Cosmic Background Explorer (COBE) satellite. *ApJL*, 354:L37–L40, May 1990. doi: 10.1086/185717.

A. R. Mitchell and D. F. Griffiths. *The finite difference method in partial differential equations*. 1980.

H. K. Moffatt. *Magnetic field generation in electrically conducting fluids*. 1978.

G. Novak, J. L. Dotson, and H. Li. Dispersion of Observed Position Angles of Submillimeter Polarization in Molecular Clouds. *ApJ*, 695:1362–1369, April 2009. doi: 10.1088/0004-637X/695/2/1362.

E. C. Ostriker, J. M. Stone, and C. F. Gammie. Density, Velocity, and Magnetic Field Structure in Turbulent Molecular Cloud Models. *ApJ*, 546:980–1005, January 2001. doi: 10.1086/318290.

T. Padmanabhan. *Structure Formation in the Universe*. June 1993.

P. J. E. Peebles. The Black-Body Radiation Content of the Universe and the Formation of Galaxies. *ApJ*, 142:1317, November 1965. doi: 10.1086/148417.

P. J. E. Peebles. Recombination of the Primeval Plasma. *ApJ*, 153:1, July 1968. doi: 10.1086/149628.

A. A. Penzias and R. W. Wilson. A Measurement of Excess Antenna Temperature at 4080 Mc/s. *ApJ*, 142:419–421, July 1965. doi: 10.1086/148307.

Planck Collaboration, P. A. R. Ade, N. Aghanim, M. Arnaud, M. Ashdown, J. Aumont, C. Baccigalupi, M. Baker, A. Balbi, A. J. Banday, and et al. Planck early results. I. The Planck mission. *A&A*, 536:A1, December 2011a. doi: 10.1051/0004-6361/201116464.

Planck Collaboration, P. A. R. Ade, N. Aghanim, M. Arnaud, M. Ashdown, J. Aumont, C. Baccigalupi, M. Baker, A. Balbi, A. J. Banday, and et al. Planck Early Results: The Planck mission. *ArXiv e-prints*, January 2011b.

Planck Collaboration, P. A. R. Ade, N. Aghanim, M. Arnaud, M. Ashdown, J. Aumont, C. Baccigalupi, M. Baker, A. Balbi, A. J. Banday, and et al. Planck Early Results:

The thermal performance of Planck. *ArXiv e-prints*, January 2011c.

PLANCK Science Team. *PLANCK - The Scientific Programme*. ESA, 2005.

W. H. Press, S. A. Teukolsky, W. T. Vetterling, and B. P. Flannery. *Numerical recipes in FORTRAN. The art of scientific computing*. 1992.

M. G. Rusbridge. The relationship between the 'tangled discharge' and 'dynamo' models of the magnetic relaxation process. *Plasma Physics and Controlled Fusion*, 33:1381–1389, October 1991. doi: 10.1088/0741-3335/33/12/004.

L. Spitzer and J. W. Tukey. Interstellar Polarization, Galactic Magnetic Fields, and Ferromagnetism. *Science*, 109:461–462, May 1949. doi: 10.1126/science.109.2836.461.

K. Subramanian and J. D. Barrow. Magnetohydrodynamics in the early universe and the damping of nonlinear Alfvén waves. *Phys. Rev. D*, 58(8):083502, October 1998a. doi: 10.1103/PhysRevD.58.083502.

K. Subramanian and J. D. Barrow. Microwave Background Signals from Tangled Magnetic Fields. *Physical Review Letters*, 81:3575–3578, October 1998b. doi: 10.1103/PhysRevLett.81.3575.

K. Takahashi, K. Ichiki, and N. Sugiyama. Electromagnetic properties of the early universe. *Phys. Rev. D*, 77(12):124028, June 2008. doi: 10.1103/PhysRevD.77.124028.

L. F. A. Teodoro, D. A. Diver, and M. A. Hendry. A cautionary note on cosmological magnetic fields. *MNRAS*, 383:L35–L39, January 2008. doi: 10.1111/j.1745-3933.2007.00406.x.

V. N. Tsytovich, G. E. Morfill, S. V. Vladimirov, and H. M. Thomas. *Elementary Physics of Complex Plasmas*. 2008.

J. P. Vallee. Observations of the Magnetic Fields Inside and Outside the Milky Way, Starting with Globules (˜ 1 parsec), Filaments, Clouds, Superbubbles, Spiral Arms, Galaxies, Superclusters, and Ending with the Cosmological Universe's Background Surface (at ˜ 8 Teraparsecs). *Fund. Cosmic Phys.*, 19:1–89, 1997.

L. M. Widrow. Origin of galactic and extragalactic magnetic fields. *Reviews of Modern Physics*, 74:775–823, 2002. doi: 10.1103/RevModPhys.74.775.

E. G. Zweibel. Magnetic field-line tangling and polarization measurements in clumpy molecular gas. *ApJ*, 362:545–550, October 1990. doi: 10.1086/169291.